Intense Terahertz Sources for 2D Spectroscopy.

Pedersen, Pernille Klarskov

Publication date:
2015

Document Version
Publisher's PDF, also known as Version of record

Intense Terahertz Sources for 2D Spectroscopy

by

Pernille Klarskov Pedersen

A thesis submitted in partial fulfilment of the requirements for the degree of Doctor of Philosophy

Technical University of Denmark

April 2015

Supervisor: Prof. Peter Uhd Jepsen

DTU Fotonik
Department of Photonics Engineering

Abstract

This Ph.D. thesis covers the development of terahertz (THz) spectroscopy systems for investigating nonlinear vibrational responses in organic biomolecules such as sucrose.

First, an add-on module for the DFT-based *ab initio* software CASTEP is developed to include a THz pulse as an external field in a molecular dynamics (MD) simulation. With this THz induced nonlinear responses and mode couplings in CsI and sucrose are investigated for increasing field strengths, and it is found that these occur for sucrose when the field strength is in the MV/cm range.

THz sources based on $LiNbO_3$, DAST, DSTMS and 2-color air plasmas are investigated, capable of generating high pulse energies i.e. up to several μJ when pumped by fs pulses with energies on the order of ~mJ. Beam profiles are measured with a commercial THz camera, and it is found that the crystal-based sources have Gaussian beams, while the THz radiation emitted from a 2-color air plasma has a conical beam profile. With the beam profiles measured through a focal plane, this has been reconstructed in 3D showing that the beam collapses to a single spot in focus. Besides the off-axis THz radiation, a weak on-axis forward propagating mode has been observed having a Gaussian beam profile.

In addition to the intense THz pulses focused in free-space in order to achieve the highest possible field strength, it is shown that resonant micro-slit arrays can be used to enhance the THz field, and with the possibility of mounting crystalline samples inside the metallic slits, this is proposed as a combined spectroscopy system for investigating high-field phenomena. With a carefully optimized design, the slit resonance can be coupled to the lattice modes of the array structure to achieve a field enhancement of more than 35 times, which is approximately 60 % more than what is observed for a similar decoupled slit.

Nonlinear spectroscopy experiments are performed on sucrose using a DSTMS THz source since this covers to the lowest lattice vibrations of sucrose from approximately 1 to 5 THz, and at the same time provided the highest field strength of almost 5 MV/cm. In agreement with the MD

simulations, a bleaching of the 1.4 THz is observed for the highest field strengths in a 1D spectroscopy configuration. Phonon coupling in sucrose is investigated with a 2D spectroscopy experiment based on a DSTMS and a DAST source, for which a new chopper scheme is presented for a direct measurement of nonlinear signals. With this, nonlinear pump-probe signals are measured with the highest response when the sucrose crystal is cryogenically cooled down 10 K. These signals reveal details about long-lived coherence and nonlinear phonon beating in sucrose induced by the intense THz pulses.

Resumé

Denne Ph.D. afhandling omhandler udviklingen af terahertz (THz) spektroskopi-systemer til undersøgelse af ikke-lineære vibrationer i organiske biomolekyler såsom sukrose.

Et nyt modul til den DFT-baserede software CASTEP er udviklet til at inkludere en THz puls, der er tilføjet som et eksternt felt i en molekylær-dynamik (MD) simulering. Med dette kan THz inducerede ikke-lineære responser og vibrations-koblinger i Csl og sukrose undersøges som funktion af feltstyrke. For sukrose er det blevet observeret at de ikke-lineære effekter indtræder når feltstyrken er i en størrelsesorden af et par MV/cm.

I denne afhandling undersøges THz kilder baseret på $LiNbO_3$, DAST, DSTMS og 2-farvet luft plasmaer, som alle har det til fælles at de kan generere høje puls-energier, dvs. op til flere μJ når de pumpes med femtosekund-pulser med energier i størrelsesordenen af et par mJ. Stråleprofiler måles med et kommercielt THz kamera, og det konstateres, at de krystal-baserede kilder har en Gaussisk stråle, mens THz-stråling, der udsendes fra et 2-farve luft plasma har en konisk stråle profil. Ved hjælp af THz kameraet er denne ståleprofil målt gennem et brændplan blevet rekonstrueret, og rekonstruktionen viste at den koniske profil kollapser til en plet i fokus. Udover den koniske THz-stråling der udsendes i en vinkel fra plasmaet, er der også en svag Gaussisk stråle der udsendes lige frem for plasmaet.

Ud over de intense THz pulser der fokuseres alene for at opnå den højest mulige feltstyrke, er det her vist at resonante mikro-spalter i en metallisk film kan anvendes til at forstærke feltstyrken af en THz puls. Ved at montere krystallinske prøver inde i de metalliske spalter, kan der udføres spektroskopi med forstærkede feltstyrker til at undersøge ikke-lineære fænomener. Hvis placeringen af de metalliske spalter designes omhyggeligt, kan spaltens resonans kobles til gitter-resonancen af slit-strukturen, og derved kan der opnås en feltforstærkning på mere end 35 gange, hvilket er ca. 60 % mere end hvad der opnås for en lignende isoleret spalte.

Ikke-lineære spektroskopi eksperimenter er udført på sukrose ved at anvende en DSTMS THz kilde, da denne dækker det mest interessante

frekvensområde fra ca. 1 til 5 THz, og på samme tid giver er den højeste feltstyrke á ca. 5 MV/cm. På samme måde som i MD simuleringsresultaterne, observeres der en blegning af 1,4 THz fononen for de højeste feltstyrker i 1D spektroskopi konfigurationen. Kobling mellem THz fononerne i sukrose undersøges med et 2D spektroskopi eksperiment baseret på en DSTMS og en DAST kilde, hvor et nyt chopper-skema er præsenteret således at ikke-lineære signaler kan detekteres direkte. Med dette, er ikke-lineære pumpe-probe signaler blevet målt med den højeste respons når sukrose krystallen er afkølet til 10 K. Disse signaler afslører vigtige detaljer om vedvarende koherens og ikke-lineær fonon-vekselvirkning i sukrose induceret af de intense THz pulser.

Preface

This thesis is a result of my time as a Ph.D. student working on the project "HI-TERA: High-intensity terahertz source for nonlinear spectroscopy at long wavelengths" from April 2012 to March 2015 at the Technical University of Denmark. The HI-TERA project was funded by the The Danish Council for Independent Research | Technology and Production Sciences (FTP) and was supervised by Professor Peter Uhd Jepsen, head of the Terahertz Science & Technology Group at DTU Fotonik – Department of Photonics Engineering. Additionally to the project funds from FTP, equipment expenses for a Helium cryostat and THz emitters of DSTMS and DAST crystals have been covered from Toubro Fonden and Brdn. Hartmanns Fond.

All experiments presented in this thesis have performed in the Terahertz Laboratories at DTU Fotonik. The amplified laser system together with the light conversion OPA system required some maintenance and alignment, which has been carried out and taught by Binbin Zhou.

During the project it has been possible to initiate a number of international collaborations with funding from the Eliteforsk travel grant. I had the chance to stay for four months at the Institute of Optics, University of Rochester in Professor Xi-Cheng Zhang's group, which led to the results of tailored field enhancements in slit arrays presented in Chapter 5. The samples were fabricated in the DTU Danchip cleanroom by Abebe Tarekegne, Maksim Zalkovskij and Krzysztof Iwaszczuk.

For the development of the CASTEP module presented in Chapter 2, I visited Professor Stewart J. Clark at Durham University, who kindly provided his expertise in DFT calculations and programmed the software. For the simulations presented in Chapter 2, phonon calculations (static DFT calculation) were done by Peter Uhd Jepsen and MD simulations were performed by me. Bernd Fischer (Marburg University) and Peter Uhd Jepsen have performed the permittivity measurement on CsI at Freiburg University.

In Chapter 4 where beam profiling of a THz beam generated from a two-color air plasma is presented, Andrew C. Strikwerda performed calculations

on Bessel-Gauss beams and Krzysztof Iwaszczuk performed the Gouy phase experiments.

Kgs. Lyngby, April 10th 2015

Acknowledgements

For the past three years I have had the chance to experience a number of amazing things – both inside and out the lab, and for this there are many people I would like to thank!

First of all I would like to thank my supervisor Peter Uhd Jepsen for being an awesome advisor in every way. It has been a pleasure to learn from someone who shares his passion for science and always motivated me to discover new research areas in a friendly and humoristic way. Also, I am grateful for Peter's way of supporting me as a person and scientist towards my future carrier and believing in me when I did not do it myself.

I am thankful to Toubro Fonden and Brdn. Hartmanns Fond, who listened to my ideas and supported them. Without their financial support I would not have been able to perform the 2D spectroscopy experiments, which I am very proud of. I am as well grateful to have received the Eliteforsk Travel grant, which gave me some priceless opportunities to establish international collaborations. I would like to thank Lars-Ulrik Aaen Andersen for nominating me, and in general for creating a nice informal and friendly research environment at Fotonik.

I would like to thank the (former) members of the THz group at DTU: Krzysztof Iwaszczuk, Corinna Koch, Tianwu Wang, Abebe Tarekegne, Jonas Buron, Andrew Strikwerda, Hualong Bao, Kimberly Reichel and Maksim Zalkovskij for all the fruitful discussions as well as scientific conversations. It has been a pleasure both to work and travel with you, and I appreciate your patience for bulky experiments. A special thanks to Kim and Abebe for the proof readings. Additionally, I would like to thank Binbin Zhou, who is the grand master of amplified laser systems, and always helped me to prepare for my experiments and understand how such complicated "machineries" work. Without Binbin I would still not have had any signal out of the Topas.

I would also like to than Xi-Cheng Zhang and his group at the University of Rochester for letting me join you for four months. It has been a pleasure to learn from you, and I will never forget the view over Lake Ontario.

Finally, I would like to thank my friends and family for distracting me when needed, and understanding that my job is more than just a job to me. I am lucky to have you in my life, and I hope you will all visit me in Providence.

Table of Contents

Chapter 1

Introduction

Terahertz (THz) is, as the name implies, frequencies in the order of 10^{12} Hz. As most other PhD theses about THz technology and science, the story begins with the electromagnetic spectrum. Although, the general public may be more familiar with the visible part, the electromagnetic spectrum spans much wider than that, and many different physical mechanisms can be studied within each frequency range. As shown in Fig. 1.1 the THz frequencies are located in the center of the electromagnetic spectrum surrounded by the microwaves on the low-frequency side and infrared light on the high-frequency side. The span of the THz range is nowhere strictly defined, but is commonly considered to be from 0.1 to 10 THz, or in the

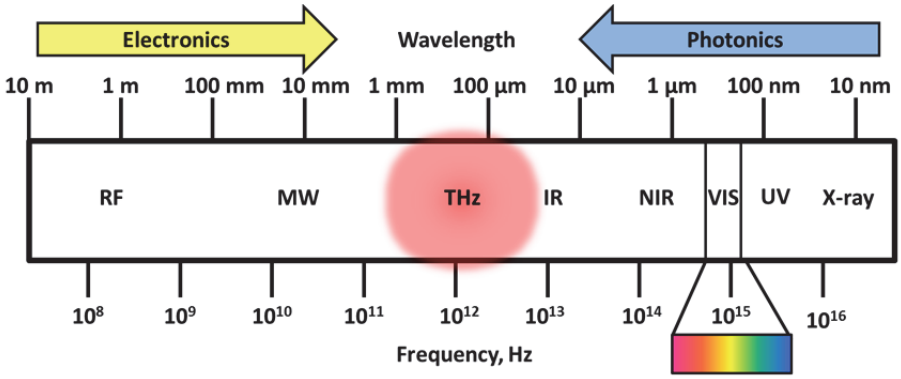

Fig. 1.1: The electromagnetic spectrum. The red dot indicates "You Are Here".

ultra-broadband case up to 30 THz. The THz regime may be approached from the electronics side, for example for wireless communication with a desire of a large bandwidth for fast data transfer rates, which is facilitated with an increased carrier frequency making THz naturally preferred over microwaves [5]. Approaching the THz from the "photonics side" implies that THz radiation is generated by an optical technique. THz generation and detection can be both complex and inefficient, and for this reason the THz range has in popular terms been known as the "THz gap". Today, several commercial THz systems for both industrial and scientific usage are available on the marked. Even though its scientific history do not go much further back than to the 80s, THz technology is today a well-established research field, and the word "Terahertz" even has its own inofficial Google Scholar page, which today has a total H-index of 142. With this, the term "THz gap" is among connoisseurs considered as outdated.

THz radiation has a number of unique properties. With the long wavelengths of hundreds of μm, THz waves are less affected by Mie scattering and can thereby propagate through many non-metallic materials such as clothes, paper, cardboard, wood, ceramics and plastic. For this reason THz radiation can be used to image objects behind such substances, which obviously has potential applications in a number of security related scenarios. A harmless illustration of this is shown in Fig. 1.2. Here a travel ID ("Rejsekort") has been scanned with the commercial THz system Picometrix T-Ray 4000. The left Panel shows the resulting THz image from where the chip containing information about the user and the ongoing journey appears in the lower left corner, and the embedded near-field antenna is seen at the circumference of the card. The photo shown in the right panel does not does not have any visible indications of the chip and antenna.

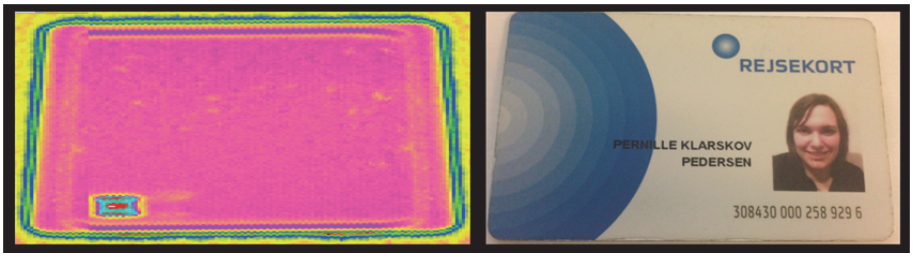

Fig. 1.2: THz imaging of a "Rejsekort"/Danish travel ID (left) together with a photo taken with an iPhone 5c (right).

As most other light sources, a THz source can be both continuous wave (CW) and pulsed. Today, compact commercial CW systems based on photomixing are available on the marked, which can rapidly be scanned between 0.1 and 2 THz to achieve spectral resolution down to 100 MHz. THz pulses have a duration of a few hundred femtoseconds (fs) and are therefore capable of pumping and probing dynamics on a fs scale. THz pulses have the outstanding property of being close to single-cycle, and for this reason among others, both the phase and amplitude can be experimentally extracted. In contrast to most other optical techniques where only the intensity is measured, the phase information recorded in addition to the amplitude with THz spectroscopy, can be directly converted in to information about material properties such as the refractive index, absorption or conductivity. At the same time a pulsed light source at any frequency, including THz, gives the possibility of achieving high peak field intensities, which is often much higher than what can be achieved of average power with CW.

In most semiconductors carriers typically have a scattering time between 50-200 fs, meaning that the conductivity spectrum falls in the THz region. For this reason THz radiation has been widely used to study carrier dynamics in traditional semiconductors, but also in new materials such as graphene [6] and carbon nanotubes [7]. Conductivity imaging of individual nanostructures with THz radiation is extremely challenging since even a tightly focused, diffraction-limited beam will have a spot size of hundreds of microns for the lowest THz frequencies. Several approaches have been implemented to improve the resolution in THz images. For example Laser Terahertz Emission Microscopy (LTEM) where instead of illumination a sample with THz radiation, an optical beam with photon energy high enough to lift carriers to the conduction band, is focused onto the sample, which will then emit THz radiation in dependence of any built-in electric fields that can accelerate the photogenerated carriers [8]. The resolution of such a system is better because light with the shorter wavelengths i.e. NIR or visible light can be focused to a much smaller spot. Another successful approach has been to add THz technology to a scanning tunneling microscope (STM) and the two technologies together offer a carrier imaging system with both nanometer spatial resolution and sub-picosecond time resolution [9, 10].

IR light is widely used for studies of intramolecular vibrational modes. Detecting such IR vibrations (at frequencies around 100 THz) that typically

involve movements of a few atoms in a molecule, for example a CH group, can provide a "fingerprint" of molecules in a sample. For a classical harmonic oscillator the frequency is given as $\omega = \sqrt{k/m}$, and by transferring this picture to the dynamics of a molecule, it is seen that molecular vibrations falling in the THz range involve larger masses and weaker forces. As a consequence, such vibrations are most often a mixture between inter- and intramolecular vibrations and hence THz modes are much more delocalized than IR modes. The fact that THz light can probe intermolecular modes instead of just the intramolecular vibrations detected with IR spectroscopy means that spectroscopic results can reveal information not only about a specific molecule, but also about its chemical environment. Because of the low photon energy of THz radiation (1 THz corresponds to 4.14 meV) it is in general considered to be harmless to biological tissue [11]. However, THz exposure has shown to induce lesions to DNA and, interestingly, also to activate DNA repair mechanisms in the cells [12]. Similarly, it has previously been the general perception that THz radiation would only probe material properties of samples, but not induce any nonlinearities or damage in a sample. Nevertheless, today's improvement in intense table-top THz sources have resulted in extreme THz phenomena such as field emission from metallic nano-tips [13], electro-migration of gold [14] and formation of nitrogen plasma from electron field emission [15]. Also, a THz induced nonlinear response of vibrational modes in amino acids have been observed with intense THz pulses [16] although not a lot of nonlinear studies considering vibrational modes have been performed compared to electron dynamics. In a broader perspective, the study of phonons in the nonlinear regime is highly relevant since non-equilibrium vibrational modes are known to be partially responsible for energy transfers in processes such as photosynthetic light harvesting [17].

2D spectroscopy is a well-established method for IR spectroscopy where time-resolved nonlinear coupling between vibrational modes is retrieved. A limited number of papers have been published on 2D THz spectroscopy [18], and despite the great potential of using this technique for investigating the lowest vibrational modes with THz spectroscopy, the complicated setup geometries and low nonlinear response most likely explains why no experimental 2D nonlinear studies of THz modes in organic materials have been published yet. In this thesis the goal is to perform 2D spectroscopy in the THz regime in order to study nonlinear vibrational dynamics in a

crystalline organic molecule such as sucrose. In order to do so, simulation studies of molecular dynamics induced by strong THz fields together with development of the strongest THz sources possible with table-top fs lasers have been united in a 2D THz spectroscopy platform.

1.1. Thesis outline

Additionally to this short introduction chapter, this thesis consists of five chapters, each representing a milestone towards the final goal of performing 2D THz spectroscopy on sucrose. The thesis is organized as follows:

Chapter 2 begins with the background for performing nonlinear spectroscopy on crystalline materials. Here, molecular dynamics (MD) simulations have been performed with the *ab-inito* DFT software CASTEP, with a specially developed add-on module capable of including a THz pulse as an external field affecting the crystal during the simulation. Simulation results for varying THz field strengths applied on CsI and sucrose crystals are presented, and the THz induced vibrational modes and mode-couplings extracted from the simulations are investigated. Having a simple crystal structure the CsI results are first compared to experimental results for verification of the developed CASTEP module. The nonlinear effects observed in simulations on sucrose when increasing the THz field strength up to the level of several MV/cm are considered as a possible input to the following nonlinear THz spectroscopy experiments presented in Chapter 6.

Chapter 3 gives a brief overview of the THz sources and detectors developed up to today's most commonly used table-top THz spectroscopy setups. The most intense THz pulses used here are generated from amplified fs laser systems, of which the main concepts are explained. A number of different methods for THz generation and detection are used through out this thesis based on photoconductive antennas (PCAs), $LiNbO_3$, organic crystals (DAST and DSTMS), 2-color air plasmas, electro-optic (EO) sampling and air-biased coherent detection (ABCD). The choice of a particular emitter and detector combination depends on the needs of the experiment, and for this reason each technique together with its pros and cons are explained, which leads to a back-to-back comparison for all the mentioned THz sources.

Chapter 4 covers a study of the beam profiles of the intense THz sources mentioned above in order to achieve the ideal beam shape for nonlinear spectroscopy experiments. This is done by scanning a commercial THz

microbolometer camera through the focal plane of the THz beam and recording intensity images of the beam at each camera position. For the THz beams generated from EO crystals the beams have a Gaussian beam profile, and for this reason they are characterized by the beam quality factor, M^2. For the THz beams generated from 2-color air plasmas a more complicated conical intensity profile is emitted from the plasma. The propagation of this through a focal plane is characterized and reconstructed in 3D from the camera measurements. With the measurements of the conical emission collapsed to a single spot in focus, a theoretical model of a Bessel-Gauss beam is proposed. The exact frequency response of the THz camera is not known, and for this reason a frequency resolved measurement of the beam size in focus is performed with a Gouy-phase experiment. The unfocused beam is resolved into frequency bands using THz bandpass filters in front of the camera. The final characterization experiment presented in Chapter 4 eliminates the conical THz emission from the beam path and leaves a weak on-axis forward propagating mode to be measured with the THz camera.

Chapter 5 considers how the field strength of a THz pulse can be enhanced in an array of resonant metallic micro-slits. Park *et al*. [19] have recently showed how a single nanoslit can be used for spectroscopy of crystalline material with a great sensitivity since the field as well as the absorption cross-section of the molecules is enhanced inside the slit. For an array structure the lattice modes of the structure on a silicon substrate interface will couple with the slit resonance itself if they are similar in frequency. This coupling is investigated by measuring the field enhancement in three series of samples where the slit resonance is varied in a fixed array, and where the lattice resonances in both directions of the surface are swept across the slit resonance. From this it is found that the field enhancement is optimum when the slit resonance is matched with the lattice mode resonances both from the direction parallel and perpendicular to the THz pulse polarization. The experiments are supported with full-wave electromagnetic simulations using CST Microwave Studio from where the field pattern of the surface plasmon polariton (SPP) waves between the resonant slits that lead to the coupling is mapped.

Chapter 6 implements the intense THz sources discussed in chapter 3 in experiments for nonlinear spectroscopy. The first part concerns 1D spectroscopy where nonlinear effects induced by single, intense THz pulses are targeted. In practice, the measured absorption spectra are investigated

when the incident THz field strength is varied. The $LiNbO_3$ source is used for the experiments on the 0.53 THz phonon in lactose, while the DSTMS source is used for measurements on sucrose, ZnTe and silicon to get a comparison to semiconductor systems when these high fields are applied. The second part describes the experimental work of this thesis with 2D THz spectroscopy based on the collinear geometry as proposed in [4] with DAST and DSTMS emitters as THz sources. A new chopper scheme for simultaneous detection of all necessary signals for extracting nonlinear signals based on boxcar detection is first presented, after which the 2D experiments are performed on sucrose at temperatures down to 10 K. The nonlinear pump-probe signals reveal details about long-lived coherence and phonon beating of the nonlinear response in sucrose induced by the intense THz pulses.

Chapter 7 concludes the work of this thesis, and gives perspectives and an outlook for future studies.

Appendices describing misaligned beam profiles, tukey windows, CASTEP scripts and experimental photos are included in the back. Video material supporting vizualized figures in this thesis can be found at http://terahertz.dk/?page_id=611.

Chapter 2

Modeling of Terahertz Interactions in Molecular Crystals

With the aim of developing a THz platform for nonlinear spectroscopy, this chapter is concerned with the development of a simulation tool for nonlinear effects when intense THz pulses interact with molecular crystals. For simulations of vibrational resonances of molecules in the THz range, various software packages based on Density Functional Theory (DFT) calculations have been used by others for this purpose. For example the CHARMM code [20] has been used to reproduce THz spectra of the amino acids L-serine and L-cysteine [21] and hydrated chicken egg white lysozyme crystals [22], and programs as DMol^3[23, 24] and LAMMPS [25] have been used for simulations of various crystalline materials such as the explosives PETN [26-28] and HMX [29]. Common to all of the above mentioned software solutions is that they are based on predefined potentials to perform classical molecular dynamics (MD) simulations [30]. These classical simulations have proven to be a powerful tool to investigate larger molecules such as proteins [22, 31], however, the usage of predefined potentials is problematic in systems where the pattern of the chemical bonding or electron density distribution is expected to shift significantly due to atomic motions [32].

An alternative to the classical MD simulations are the *ab initio* MD simulations where the forces acting on the nuclei from the electronic structure are calculated "on-the-fly" at each timestep in the simulation [30]. For this reason the *ab initio* MD simulations have a great potential of

investigating crystalline materials in the nonlinear regime where the intermolecular potential energy is expected to be anharmonic. These potential-free simulations rely on the ability to select approximate solutions to the Schrödinger equation. In this quantum mechanical regime the correlation lengths are, however, much smaller than in the classical regime, resulting in much longer simulation times.

CASTEP (Cambridge Serial Total Energy Package) is an example of a commercially available DFT-based code capable of performing *ab initio* simulations [33]. Briefly explained, one-electron Schrödinger equations are solved using the the plane-wave pseudopotential approach, where the strong

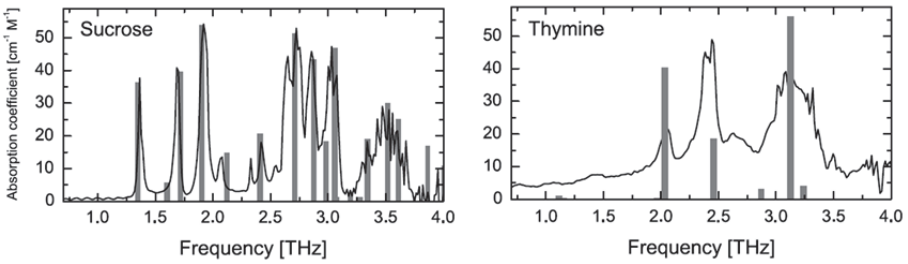

Fig. 2.1: Measured absorption spectra and calculated vibrational modes of sucrose and thymine [2].

ion electronic potentials are replaced with much weaker potentials describing only the valence electrons to simplify the calculations [34]. Using periodic boundary conditions and Bloch's Theorem, the wavefunctions are expanded into plane waves, after which the electronic wavefunctions and corresponding charge densities are found with a self-consistent energy minimization scheme. CASTEP can been used for a wide range of applications for investigation of material properties including EELS, Raman and NMR spectroscopy [35], and in 2007 it was demonstrated that CASTEP can accurately predict vibrational modes of crystalline materials in the THz range [2]. Using CASTEP for simulations of THz modes is computationally demanding for several reasons. Firstly, compared to intramolecular IR modes that are usually much more localized and originates from motions between a few atoms (for example C=O stretch, CH_2 rocking etc.), vibrational modes in the THz range are intermolecular. This means that it is necessary to include the full periodic structure of a molecule to calculate the phonon modes in the THz range with a DFT software. Secondly, CASTEP simulations of THz frequencies require tight convergence tolerances on

energies and atomic positions in order to avoid numerical errors. For simulations of high-frequency modes an error of a few wavenumbers is normal whereas this is unacceptable in the THz range. In [2] Jepsen and Clark compared the calculated phonon modes of sucrose, benzoic acid and thymine with absorption spectra measured with a THz-TDS system based on photoconductive antennas. Their results obtained from sucrose and thymine are shown in Fig. 2.1, where the solid black curves are the experimentally obtained absorption spectra and the grey bars are the calculated modes. The overall agreement between the measured and calculated modes is very good, proving that CASTEP is indeed capable of calculating vibrational modes in the THz range.

In this thesis, the aim is to investigate nonlinear effects in crystalline materials using intense THz sources such as $LiNbO_3$, two-color air plasmas and organic crystals (DAST and DSTMS), which produce pulse energies that are hundreds of thousands times larger than what is typically obtained with photoconductive antenna sources (see Fig. 3.1 in chapter 3). The expected nonlinear effects in crystalline materials when exposing them to such intense THz field could be bleaching [16] or frequency shifts [16, 36] of the phonon resonances. The phonon calculations presented in [2] represents a "static" case where influence of the THz field on the ions in the crystal is not taken into account. To be able to predict nonlinear phonon responses induced by intense THz pulses, it is demonstrated in this chapter how a THz pulse can be added to a MD simulation in the CASTEP code. The programming of this CASTEP module has been done in collaboration with Prof. Stewart Clark at Durham University. In the following, the implementation of the THz pulse is explained, and simulations of the molecular dynamics in cesium iodide (CsI) and sucrose when being exposed to THz fields of increasing field strengths are presented. It is shown how the intense fields can affect the phonon resonances.

2.1. Implementation of a THz Pulse in CASTEP

In order to simulate the interaction between a THz pulse and molecular crystals, an external force on the polarizable ions is added in the CASTEP code,

$$F_{THz} = q_{eff} E_{THz} = (q_{Mulliken} + \alpha_{THz} E_{THz}) E_{THz} , \qquad (2.1)$$

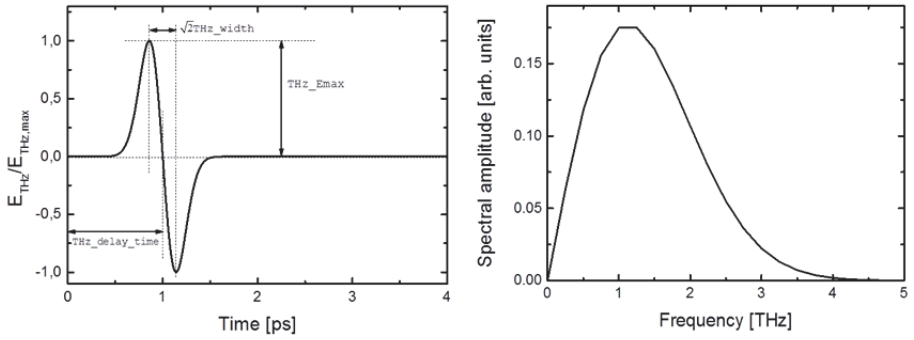

Fig. 2.2: Electric field implemented in CASTEP using Eq. (2.2) with a=1, b=1 ps and c=0.2 ps (left) and the corresponding spectral distribution obtained by a Fourier transform (right).

where $q_{Mulliken}$ are the Mulliken charges [37] on each ion at each time step in the simulation, and α_{THz} is the THz polarizability. The THz field is defined as a differentiated Gaussian function i.e.

$$E_{THz}(t) = \frac{a(b-t)}{c^2} e^{\frac{-(t-b)^2}{2c^2}} \tag{2.2}$$

where *a, b* and *c* are constants determining the amplitude, delay time and width of the THz pulse, respectively. These parameters can be set freely in each simulation, but for the results considered in this chapter, the parameters are set so that the THz pulse represents what can be generated with a $LiNbO_3$ source, as shown in Fig. 2.2. An electric field following the expression in (2.2) is shown in the left panel, where *b* is set to 1 ps and *c* is 0.2 ps. Figure 2.2 (right) shows the corresponding spectral distribution obtained by a Fourier transform. Having a spectral bandwidth of 3 THz is comparable with what can be generated with $LiNbO_3$ (see Fig. 6.2 in Chapter 6 for an experimentally obtained spectrum from $LiNbO_3$).

2.1.1. Statistical Ensembles

When running an MD simulation in CASTEP it is important to choose the correct statistical ensemble and to determine which conditions are fixed during the simulation and which are sampled. Per default, CASTEP uses the NVE ensemble (constant number of ions, cell volume, and energy). The additional energy added from the THz pulse is not included in this conservation of energy. However, the externally added energy is not

dissipated here, which is not consistent with the experimental situation, where excitation of lower-energy vibrational modes (acoustic phonons) will dissipate the vibrational energy of the optical phonons excited by the THz pulse.

A useful alternative is the NVT ensemble, which conserves temperature, and may therefore be a better choice for the MD simulations with external excitation by a THz pulse. An important part of the NVT ensemble is a thermostat with a certain time constant that adjusts the dissipation rate of energy to the external heat bath. This time constant should possibly be set to a value similar to the experimentally observed decay time of the phonon vibrations, but the effect of this has not been explored to any significant extent yet. For the simulations presented in this chapter, an NVT ensemble with a Nosé-Hoover thermostat [38] is used, which gives a fixed average temperature but still allows for temperature fluctuations. This is crucial since some temperature fluctuations are expected when the THz field is applied, but the temperature should eventually converge back to its initial set value.

Other statistical ensembles offered in CASTEP are NPH (constant ion number, pressure and enthalpy) and NPT (constant ion number, pressure and temperature). Both ensembles allows the size of the simulated crystal structure to vary, and for investigations lattice motions i.e. phonons while applying strong THz field this can be advantageous. Preliminary simulations using NPT ensembles where the pressure was set to 1 bar achieved promising results, however, these simulations were significantly more time consuming than when using the NVT ensemble, and for this reason NVT was preferred.

2.1.2. Exchange-correlation Functionals

In DFT theory it is important to use appropriate approximations for describing the form of the exchange-correlation energy functional [39]. The most widely used approximation is the local-density approximation (LDA) that assumes that for an infinitesimal modification of the density the exchange-correlation energy can be described as a uniform electron gas [33]. Per default, CASTEP uses the LDA exchange-correlation functional. This is a good choice for strongly bound ionic systems such as ionic salts, and for this reason this has been used for the simulations of CsI in section 2.2. However, the Perdew-Burke-Ernzerhof (PBE) functional is an approximation based on fundamental constants giving a functional that is

more appropriate for inhomogeneous densities [40, 41], which has been reported to work better for hydrogen-bonded molecular crystals [42]. This functional was used by Clark and Jepsen in [2] for the calculation of precise phonon frequencies in molecular crystals, and is also used in for the MD simulations of sucrose presented in section 2.3.

2.1.3. Running a Molecular Dynamics Simulation

CASTEP requires two files to run a simulation, namely a "<jobname>.cell" file and a "<jobname>.param". The .cell file stores the geometric arrangement of the ions and the dimensions of the unit cell, which typically is created using the Accelrys Materials Studio software. The .param file stores the run parameters i.e. the chosen type of calculation, values of certain parameters such as the applied THz field pulse, the choice of statistical ensemble and exchange-correlation functional and other parameters that control the calculation. In addition to these two CASTEP required files, a script is used to execute CASTEP on a specified number of nodes on the cluster. The simulations presented in this chapter are calculated on the FOTONANO computer cluster at DTU using Intel® Xeon® E5-2665 processors. For a simple unit cell of CsI a simulation of 20 ps with a resolution of 1 fs can be achieved using 28 processors in 24 hours, while the simulations for sucrose presented in section 2.3 have taken approximately 8 months to obtain using either 64 or 96 processors including "cluster queue time", which is probably more than 50% of the total time.

For efficient parallel computing it is important that the number of *k*-points in the geometric structure is a divisor of the selected number of processors. The required computational time scales with the number of k-points, so the used number of *k*-points represent a reasonable compromise between precision and available computational resources. For a CsI unit cell the number of *k*-points was set to 14 and the CsI 2x2x2 supercell calculations used 4 *k*-points, hence the choice of 28 processors. The sucrose simulations were also performed with 4 *k*-points leaving both 64 and 96 processors as appropriate choices.

Examples of .cell and .param files can be found in Appendix A.

2.2. Molecular dynamics in cesium iodide

The first molecule considered for MD simulations with an implemented THz pulse using the developed add-on module to CASTEP, is CsI. As discussed

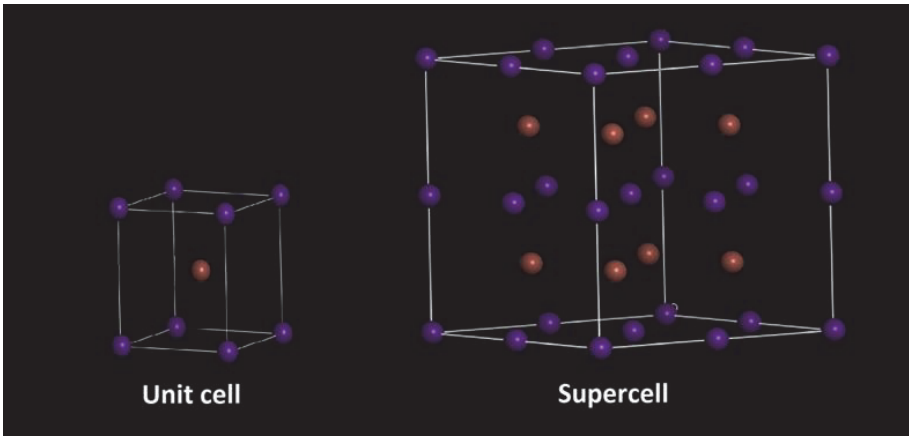

Fig. 2.3: The CsI unit cell and the 2x2x2 supercell. Purple spheres represent Cs+ ions and red spheres indicate I- ions.

above, its simple crystal structure means that the MD simulations are relatively fast, and at the same time it has a strong optical phonon in the THz range to be studied. CsI forms a body-centered cubic (bcc) crystal lattice, with lattice constant 4.57 Å. In this section both the CsI unit cell as well as a 2x2x2 supercell is studied in order to see effects of the optical as well as acoustic modes. The unit cell and the 2x2x2 supercell structures created with Accelrys Materials Studio are shown in Fig. 2.3, where the purple and the red balls represent the Cs^+ and the I^- ions, respectively.

2.2.1. The measured dielectric function of cesium iodide

To achieve some background knowledge of the optical properties of CsI the experimentally obtained permittivity is considered. Figure 2.4 shows the spectrum of the real (left) and imaginary (right) part of the permittivity in the range from 0.5-3.0 THz, measured by THz time-domain spectroscopy. The measurements were carried out in reflection geometry, using a plane, metallic mirror as the reference reflector [43]. The permittivity is extracted from the measured amplitude and phase of the reflected signal from the sample, measured relative to the metallic reflector. Assuming unity reflection coefficient from the metal, the ratio is determined by the complex index of refraction $\tilde{n}$ of the sample,

$$\frac{\tilde{r}_{sam}}{\tilde{r}_{ref}} = \frac{\tilde{n}-1}{\tilde{n}+1} \tag{2.3}$$

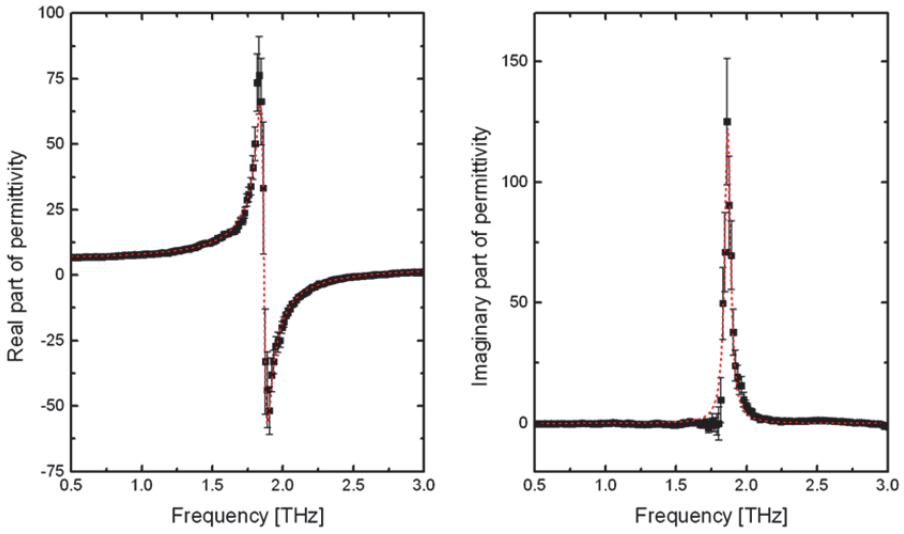

Fig. 2.4: The solid squares are the measured real (left) and imaginary (right) parts of the permittivity of CsI. Dashed, red curves represent a global fit of the Lorentz oscillator model to the experimental data.

The permittivity is then calculated as $\tilde{\varepsilon}(\nu) = \varepsilon'(\nu) + i\varepsilon''(\nu) = \tilde{n}(\nu)^2$. The experimental data are shown as solid squares, and a global fit based on the Lorentz oscillator model,

$$\varepsilon(\omega) = \varepsilon_\infty + \frac{\omega_p^2}{\omega_0^2 - \omega^2 - i\omega\gamma}, \tag{2.4}$$

is shown together with the experimental data as the red dashed line. The fitted parameters of the Lorentz model are estimated as follows. The plasma frequency $\omega_p = (21.17 \pm 0.12)$ THz, the resonance frequency $\omega_0 = (11.722 \pm 0.002)$ THz, the damping rate $\gamma = (0.312 \pm 0.05)$ THz, and the optical permittivity $\varepsilon_\infty = 3.55 \pm 0.15$. This gives the strong resonance seen at $\nu = 1.87$ THz.

2.2.2. Terahertz induced effects in cesium iodide

Using the crystal structures shown in Fig. 2.3, MD simulations are performed with different THz peak field strengths from 0 to 50 MV/cm interacting with the CsI unit cell and supercell, respectively. The direct

outputs from CASTEP are the position of the ions and their velocity at each time step. In order to compare the simulation results with experimentally accessible quantities, the velocities of the ions at each time step in the simulation are used to calculate the velocity autocorrelation function (VAF). The VAF at the *i'th* time step is defined as

$$C_v(t_i) = \sum_{j=0}^{M-1} \sum_{k=1}^{K} \mathbf{v}_k(t_i) \cdot \mathbf{v}_k(t_i + j\Delta t) \tag{2.5}$$

where M is the number of time steps, K is the number of ions and Δt is the time step size. The spectral density (square of the Fourier transform) of the VAF corresponds to the vibrational density of states (VDOS) of the system, which for the optical phonons can be compared to the experimentally obtained imaginary part of permittivity.

Fig. 2.5 shows the VAF for zero and 20 MV/cm field strength applied to the CsI unit cell (top traces) and supercell (lower traces), respectively, for the unit cell (left) and supercell (right) simulations.

When no external field is applied during the simulation, all motion is due to thermal energy at the finite simulation temperature (here 10 K). The VAF for the unit cell is a very clean oscillation due to the presence of a single optically active mode, the TO phonon. In contrast, the corresponding VAF for the supercell simulation shows a more complicated beating pattern of several modes, resulting in a much faster decay of the VAF, due to dephasing of the different modes.

For the VAF in the upper part of the right panel representing the simulation with 20 MV/cm peak field strength applied to the unit cell at t = 1 ps, it is seen how the VAF amplitude increases when the THz pulse reaches the CsI. The transient increase of the VAF decays after approximately 7 ps. The slight modulation of the envelope of the VAF after 7 ps is predominantly a numerical artifact due to the Nosé-Hoover thermostat.

Similar to the situation at zero field, comparing the unit cell VAF at 20 MV/cm with that of the supercell simulation (lower trace, right panel) reveals that the unit cell VAF oscillates in a periodic manner, whereas the trace of the VAF for the supercell appears to be more complicated, with a much faster dephasing time. These oscillations are caused by beating of several modes, and are expected to be of acoustic modes, which are present

in the supercell simulations with a wavelength of twice the lattice constant, but are not present in the simulations of the unit cell.

The VDOS for the simulations of the unit cell for different THz field strengths from 0 to 50 MV/cm are shown in Fig. 2.6. At approximately 1.95 THz a resonance is seen, which is identified to be the TO phonon mode seen in the experimental data shown in Fig. 2.4. In the field-strength dependent simulations it is seen that the phonon sharpens when the field increases up to 5 MV/cm. At the higher field strengths the phonon starts reds-shifting until the field strength reaches 50 MV/cm, where no clear resonance is seen anymore. This is understood as an indication that the field strength is approaching a value where the field is strong enough to melt the crystal, and thus the crystalline structure of CsI breaks down.

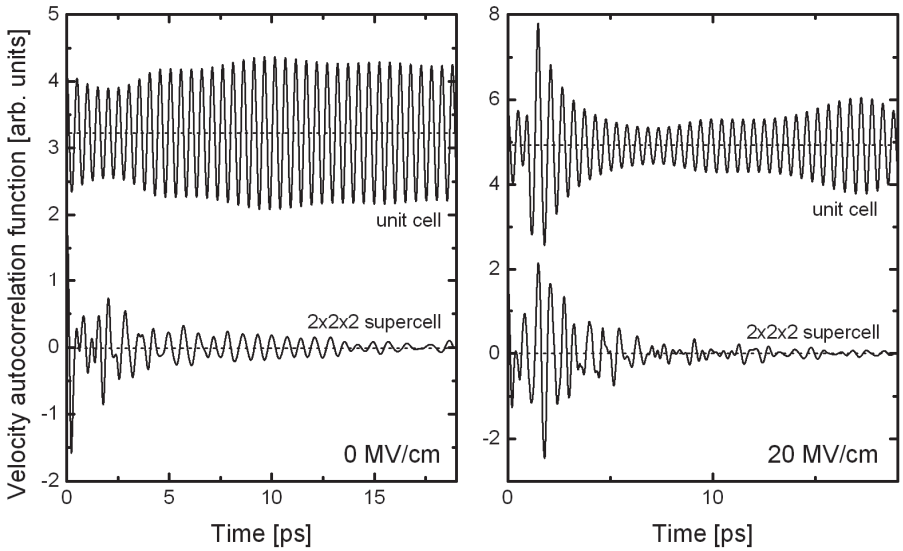

Fig. 2.5: Example of VAFs calculated from the supercell simulations. The left panel shows the VAF for zero field applied, and the right panel shows the VAF for an incoming THz field of 20 MV/cm.

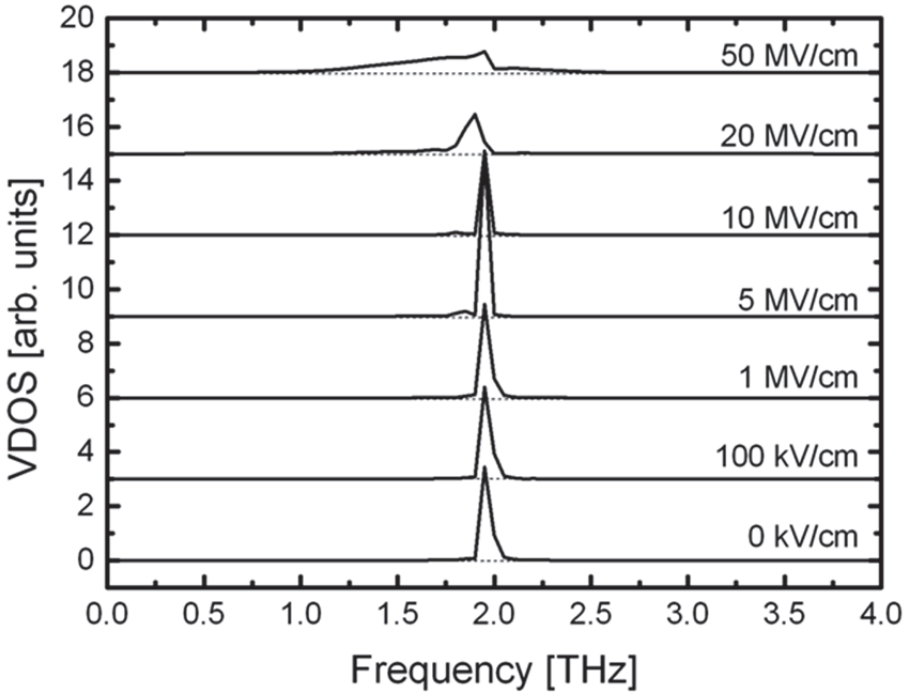

Fig. 2.6: Vibrational density of states (VDOS) for the unit cell at different field strengths from 0 to 50 MV/cm. Each trace has been vertically offset for clarity

The VDOS for the simulations of a THz field with varying field strength interacting with the supercell are shown in Fig. 2.7. In contrast to the VDOS for the unit cell, the VDOS for the supercell shows a collection of several resonances in a much more complicated pattern. This is in agreement with the beating in the VAFs, which to a higher degree is observed for the supercell than the unit cell. The TO-phonon seen in the unit cell VDOS at 1.95 THz, does only weakly appear for 0 MV/cm, while the signal of this is increasing up to 1 MV/cm, and decreasing again at higher field strengths. The sharp modes around 1 THz and 1.4 THz are expected to be acoustic modes, and the broad mode at approximately 2.5 THz is expected to be the LO phonon [44-46]. None of these additional modes are infrared active, but are still visible in the VDOS, which does not take selection rules into account. Again, for the highest field strength of 20 MV/cm, the distinct features merge to a very broad peak at 1.5 THz indicating the first steps of melting of the crystal as discussed for high field strength interacting with the unit cell crystal.

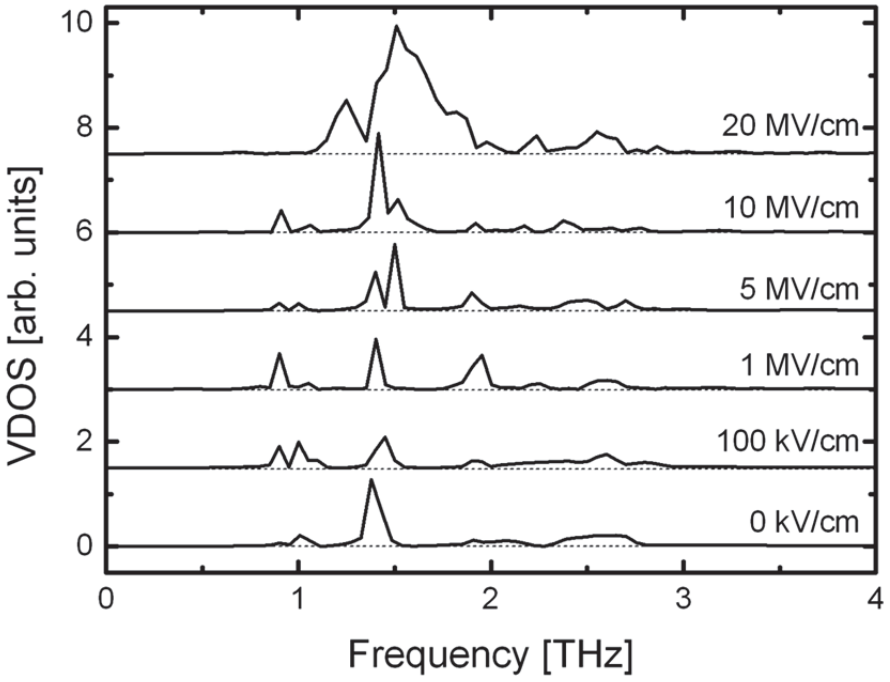

Fig. 2.7: Vibrational density of states (VDOS) for the 2x2x2 supercell at different field strengths from 0 to 20 MV/cm. Each trace has been vertically offset for clarity.

The vibrations of the CsI crystals during the simulations have been visualized by monitoring the ion positions at all time steps using the VMD software [7] and can be seen at http://terahertz.dk/?page_id=611 (first two links under "Klarskov Thesis results"). The videos show the movements of the ions at a THz field strength of 20 MV/cm interacting with the unit cell and the supercell, respectively. Also here it is seen how the unit cell only exhibits a single vibrational mode corresponding to the TO phonon vibration, whereas the supercell vibrates in several modes. Both videos are composed of several of the simulated cells periodically arranged together.

The time-dependent evolution of the VDOS can be investigated using a short-time Fourier transform (STFT) to create a spectrogram. This means that the VAF is broken into segments by a window function which is translated across the full simulation time span in a time sequence, τ. The Fourier transform is calculated at each time step the local window is applied, and the STFT is the resulting map obtained from all the Fourier transforms

as a function of time. A spectrogram is the magnitude squared of the STFT i.e.

$$S(\tau,\nu) = |STFT(\tau,\nu)|^2 = |\int_{-\infty}^{\infty} C_v(t) W(t-\tau) e^{-2\pi i \nu} dt|^2 \quad (2.6)$$

where $C_v(t)$ is the VAF calculated in (2.5) and W is the window function. In this case a Hanning window is used

$$W(t-\tau) = \frac{1}{2}(1+\cos(\frac{\pi(t-\tau)}{L-1})) \quad (2.7)$$

where L is the size of the window. For the spectrograms calculated in Fig. 2.8 the L value was set to 4.096 ps and the window was moved 96 fs per iteration $(\Delta\tau)$. The left panel is the spectrogram calculated for the simulation of the unit cell when a field of 50 MV/cm is applied. It is seen that the nonlinear spectral broadening observed for the corresponding trace in Fig. 2.6 occurs during the first 1-2 picoseconds when the system interacts with the THz transient, but after this the TO phonon at 1.95 THz sharpens again. After 3-6 ps the intensity of the phonon is reduced, and gains again after 6 ps. As discussed above this rapid broadening when the intense THz field is applied is considered as a pre-state to the melting of the crystal, however, the spectrogram shows that this is only temporary, and the crystal structure recovers on a time scale of a few picoseconds. For the spectogram calculated for the 2x2x2 supercell when 1 MV/cm is applied is shown in the right panel of Fig. 2.8. The main broadening is again occuring within the

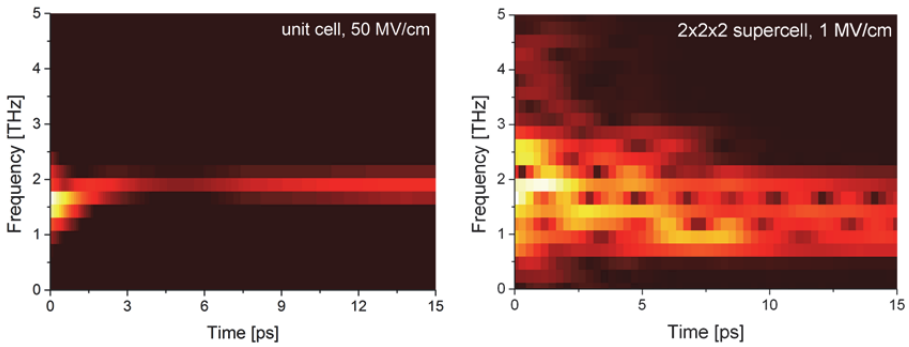

Fig. 2.8: Short-time Fourier transform (spectrogram) of theVAF calculated for the unit cell simulation when a field of 50 MV/cm is applied (left) and for the 2x2x2 supercell when 1 MV/cm is applied.

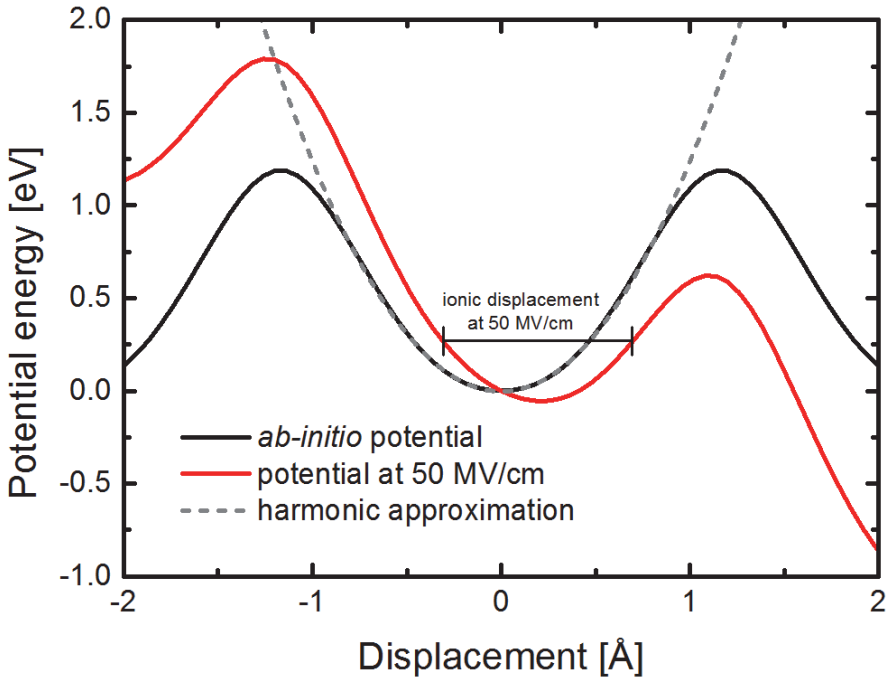

Fig. 2.9: Vibrational potential of the TO phonon from ab-initio calculations (black curve), its harmonic approximation (grey, dashed curve) and the potential curve at 50 MV/cm field strength (red curve). The horizontal bar shows an example of the simulated oscillation amplitude of the Cs ion at 50 MV/cm THz peak field strength.

first 2 picoseconds when the THz field is present. What is particularly interesting for this spectrogram is that the spectral distribution is not stationary at any time, instead the modes are beating over the entire time axis. This is for example seen as the reappearing dark spots at app. 1.8 THz. The TO phonon at 1.95 THz seems to dominate the spectrum while the THz field is on, but after the 2 ps the accoustic mode at 1.4 THz is more intense, and from 6 to 9 ps the accoustic mode at 1 THz is most present. This is interpreted as that the TO phonon couples its energy to the acoustic modes and thereby the resulting VDOS shown in Fig. 2.7 are dominated by the acoustic modes.

The nonlinear response of the system in this case is due to the slight anharmonicity of the very tight (approximately 2 eV deep) vibrational potential energy of the TO phonon eigenmode. To investigate this further the vibrational potential energy is calculated by an ordinary DFT single point

energy calculation in CASTEP when displacing the ions along the normal mode coordinates of the TO phonon motion. From the visualizations of the unit cell vibration it is seen that this mode corresponds to displacement of the Cs ions with respect to the I ions along the z-direction. Fig. 2.9 shows the calculated vibrational potential of the TO phonon when displacing the ions in the z-direction from their geometrically optimized positions (black curve). The dashed, grey curve shows the harmonic approximation to the potential energy at small displacements. The vibrational potential is symmetric and follows closely the harmonic approximation up to energies of more than 1000 meV. The potential energy curve is modified instantaneously by the external electric field ($V(x,t) = -E(t)\cdot x$) as shown for a peak field strength of 50 MV/cm (red curve). The horizontal bar indicates the magnitude of the Cs ion motion at 50 MV/cm applied field strength. From these considerations it can be seen that the ultrafast dynamics of the system brings it close to damage threshold (melting), seen in Fig. 2.9 as the local potential energy maximum at 1 Å displacement (red curve). In more complex systems with softer vibrational potentials, it can be expected to observe potentials with lower binding energies and larger nonlinearities. In such situations, nonlinear responses should be observed at lower field strengths, and for this reason, sucrose is studied in the following section.

2.3. Molecular dynamics in Sucrose

As shown in Fig. 2.1, sucrose has a large number of optical phonons in the THz range, and is therefore an obvious candidate for the study of nonlinear coupling between the optical phonons. Sucrose is a carbohydrate with the chemical formula $C_{12}H_{22}O_{11}$, and the unit cell of a sucrose single crystal contains two sucrose molecules sitting in the configuration as shown in Fig. 2.10. The transmission of sucrose in the infrared part of the electromagnetic spectrum can be measured with Fourier transform infrared spectroscopy (FTIR) giving the absorption of the IR modes and the high frequency THz modes. An example of an FTIR spectrum of sucrose [21] is shown as the blue curve in Fig. 2.11. The highest frequency modes from 97 to 107 THz have been identified to be mainly OH stretch modes while the slightly weaker bands from 86 to 91 THz are CH and CH_2 stretching modes [47]. Sucrose is found to be almost completely transparent between 45 and 86 THz where no vibrational modes are found, and the modes from 34 to 45 THz are recognized as CH_2 scissoring, wagging and rocking modes together with the CH rocking mode. At lower frequencies, more complex and

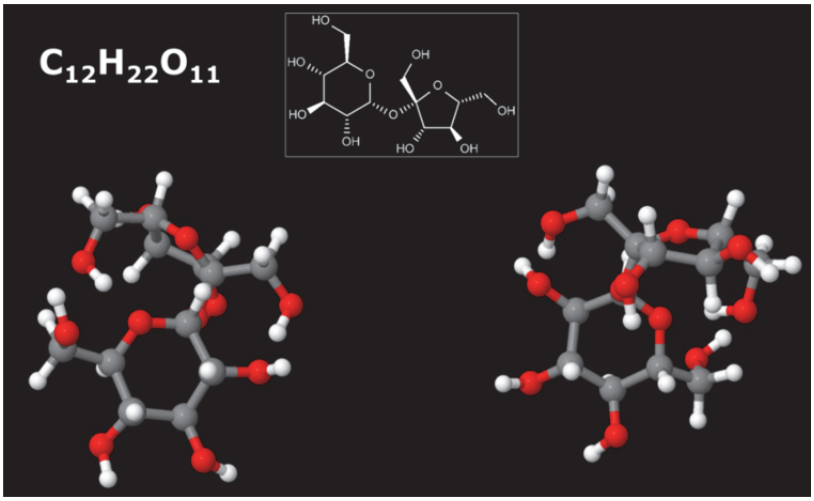

Fig. 2.10: The sucrose unit cell. Red, grey and white spheres are oxygen, carbon and hydrogen, respectively. The inset shows the structural formula of a single molecule.

delocalized modes involving combinations of several of the above mentioned modes. The most delocalized modes below 10 THz are primarily of interest in this thesis. However, to investigate the reliability of the CASTEP code when implementing a larger, hydrogen bonded crystal structure, the vibrational modes of sucrose from 0 to 110 THz are calculated in two different ways: 1) the possible eigenmodes of sucrose structure is calculated in the same way as in [2] shown as the black bars in Fig. 2.11 and 2) by performing an MD simulation without any THz field applied (red curve in Fig. 2.11). It is seen that both the eigenmode calculation and the MD simulation agree well with vibrational features obtained with the FTIR measurement. In all cases a low-frequency and high-frequency band of modes are obtained from 0 to 50 THz and 80 to 107 THz, respectively, while in between no vibrational modes are observed. The high-frequency bands of the MD simulations are slightly redshifted from the CH and OH stretch modes obtained in the FTIR measurements, but some deviation at higher frequencies is somewhat expected since the MD simulations shown here are optimized for the low-frequency THz modes. At the same time, the temperature conditions are different for the three curves. The DFT calculations resulting in the phonon eigenmodes are assuming a temperature of 0 K, while the MD simulations are performed at 10 K and the FTIR spectrum is measured at room temperature. For the MD simulations it was possible to set the temperature at any finite value larger than 0 K, and the

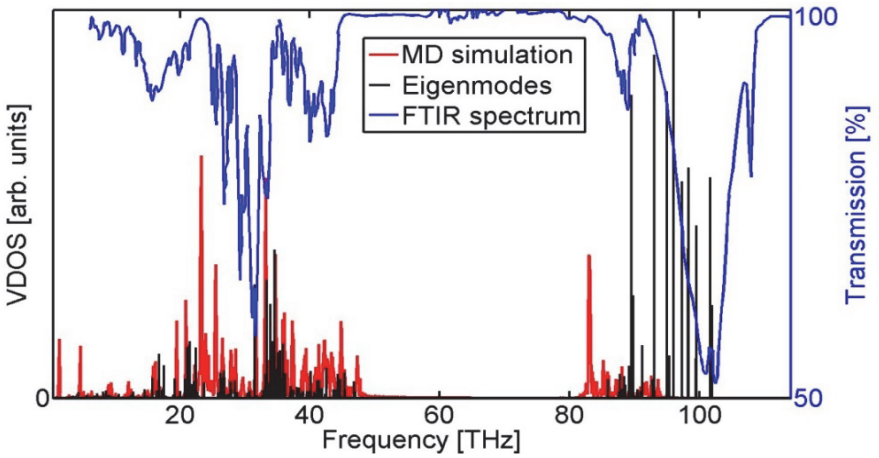

Fig. 2.11: FTIR transmission spectrum of sucrose (blue curve) together with the VDOS calculated from a MD simulation without any THz field applied (red curve) and a DFT simulations of the eigenmodes (black bars).

choice of 10 K is advocated by the significant sharpening of the absorption peaks at low temperatures compared to at room temperature [36]. For the same reason the 2D THz spectroscopy measurements on sucrose presented in Chapter 6 are also performed at 10 K.

As mentioned in section 2.1.2 the most important setting to be changed in CASTEP when performing an MD simulation on hydrogen bonded materials compared to an ionic lattice is the usage of the PBE exchange-correlation functional instead of the LDA functional. Except from this, the MD simulations for sucrose were performed in the same way as for CsI. However, when calculating the VAF from the CASTEP output, the more complicated crystal structure and large number of atoms lead a significantly more noisy time trace. For this reason an averaged VAFs was calculated for the sucrose MD simulations i.e.

$$< C_v(t_i) >= \frac{1}{N}\sum_{n=1}^{N} C_v(t_i + n\Delta t) \tag{2.8}$$

where $C_v(t_i)$ is calculated as in (2.5) and N is the number of averages in where each of the single VAFs are calculated in a window that is slided in steps of Δt. Fig. 2.12 shows the difference between a single VAF calculated for a sucrose MD simulation (left) and VAF calculated over 100 averages. Both traces appear significantly more noisy than for the CsI simulations,

however, the averaged trace fluctuates less and the effect of the reduced is even clearer in the corresponding VDOS shown in the insets. Using 100 averages gives a total window shift of 100 fs meaning that features faster than 100 fs i.e. frequencies higher than 10 THz cannot be well resolved from the averaged VAF if it has not reached a steady state. To conserve mostly the molecular vibrations induced by the applied THz field, the averaged VAF is calculated from the time position of the positive peak of the THz field i.e. t_i = 839 fs. The VDOS corresponding to the single VAF and 100 times averaged VAF is shown as the insets in Fig. 2.12. The spectral features in each case appear quite unlike, but the averaged spectrum is expected to be most representative for the THz induced vibrations. Especially, the more clear appearance of the phonon at 1.4 THz is ideal since this will also be considered in the experimental part of this thesis discussed in Chapter 6. In the follow is presented the results of MD simulations with different field strengths of the applied field strengths. From the CASTEP output the VAFs are all calculated using 100 averages in the same way as described above.

The VDOS spectra calculated from the averaged VAFs for the applied THz field strengths of 10 MV/cm, 30 MV/cm, 50 MV/cm and without any applied any THz field applied are shown in Fig. 2.13. Considering the VDOS without any field applied the two peaks at 1.38 THz and 4.59 THz are most significant. For the reference these positions are indicated with vertical dotted lines. For both peaks it is observed that the maximum position redshifts when the THz field is applied and increased. The height of both peaks decrease when the field strength is increased to 30 MV/cm which is interpreted as a bleaching. The value of the peak at 1.38 THz increases again when the highest field of 50 MV/cm is applied while the peak at 4.59 THz is

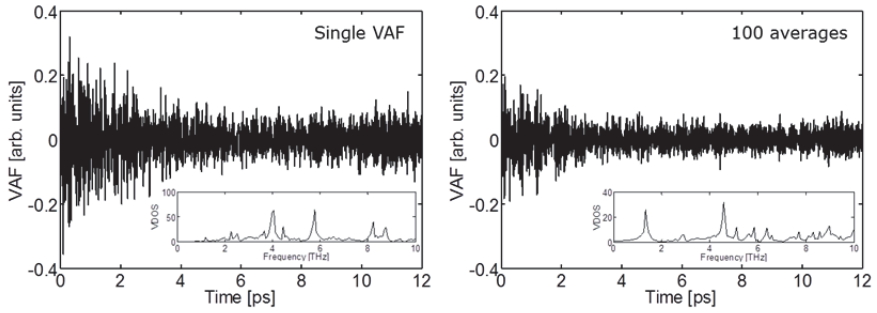

Fig. 2.12: Velocity autocorrelation function (VAF) calculated directly from the CASTEP output (left) and using 100 averages (right).

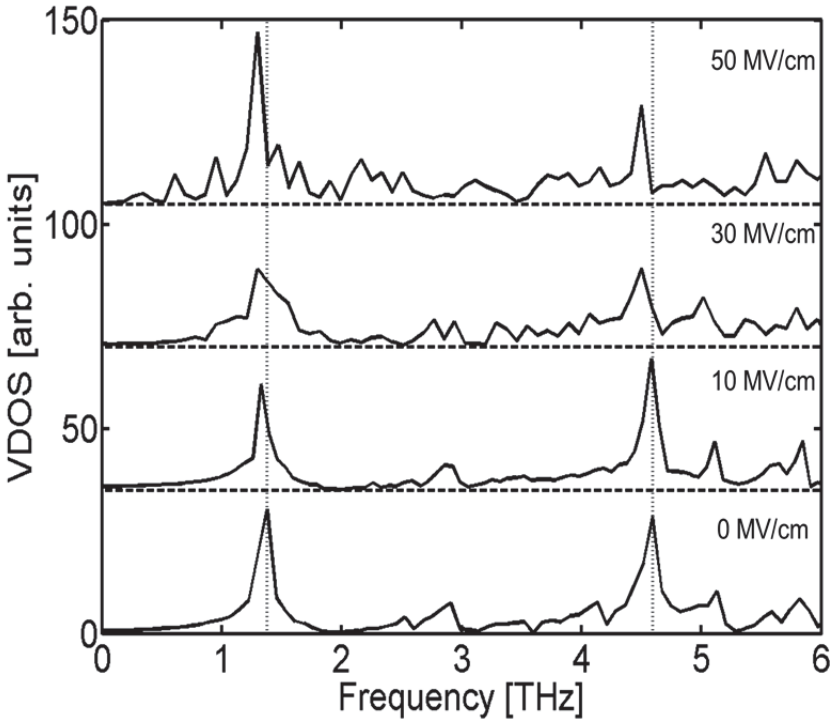

Fig. 2.13 :VDOS for the sucrose unit cell at different field strengths from 0 to 50 MV/cm. Each trace has been vertically offset for clarity.

still bleached.

In a similar way as for CsI in section 2.2.2 the vibrational potential energy for the phonon at 1.38 THz is estimated by calculating the single point energies when displacing the ions in the crystals along the normal mode coordinates with a standard DFT simulation in CASTEP, which is shown as the circles in Fig. 2.14. As mentioned previously the sucrose THz modes are very delocalized and involve movements of several ions, and the estimation of the mode displacement is much more complicated than for TO phonon of CsI. For simplicity, the displacement of the 1.38 THz in sucrose is here estimated displacement of the most displaced ion along the eigenvector of the mode shown in Fig. 2.14 as the circles. The blue curve is the harmonic approximation to the smallest displacements within ± 0.1 Å in which the energy response is assumed to be linear. At larger displacements it is observed that the ion gains a larger potential energy than the energy predicted for the harmonic approximation. For a Morse potential having a softer shape than a harmonic potential and thereby more closely spaced

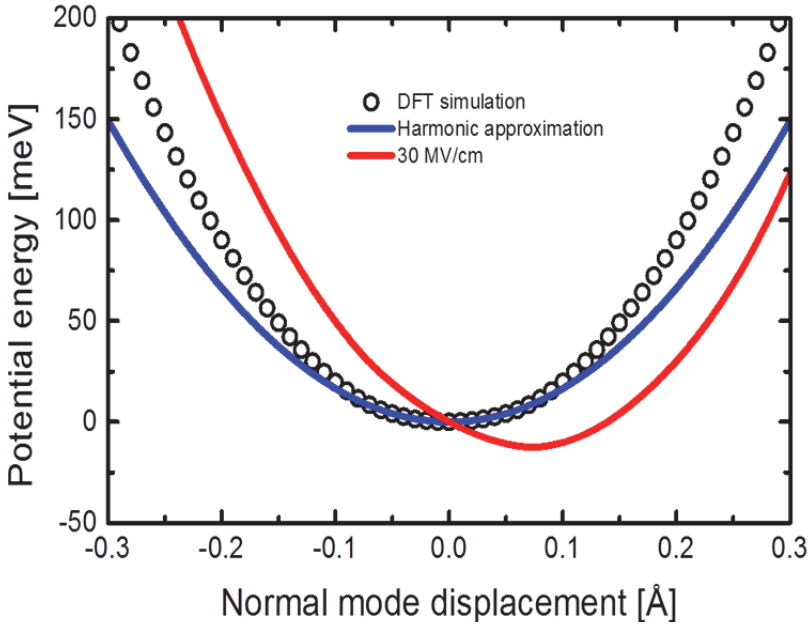

Fig. 2.14: Vibrational potential for the 1.38 THz mode in sucrose calculated from DFT calculations (empty dots), its harmonic approximation (blue curve) and the potential curve at 30 MV/cm field strength (red curve).

energy levels leading to a redshift for a specific resonance frequency, the inverse situation where the potential energy is steeper than the harmonic approximation as seen for the 1.38 THz mode is expected to lead to a blueshift. This is, however, in contradiction to what is observed for the VDOS in Fig. 2.13. The red curve shows the potential energy modified by the THz field of 30 MV/cm calculated in the same way as for the CsI displacement potential explained in section 2.2.2. Comparing the original potential of the mode displacement (circles) with the potential modified potential (red curve), the modified potential appears steeper than the original potential confirming the expectation of a blueshift when a strong THz field is applied.

To investigate the time-resolved effect of the strong THz field interacting with the sucrose crystal, spectrograms are calculated for the MD simulations with different field strengths applied. The spectrograms without THz field and with a field of 50 MV/cm giving the clearest demonstration of the vibrational dynamics induced by the THz field are shown in Fig. 2.15. The averaged VAFs are used for the calculation of the spectrogram meaning that

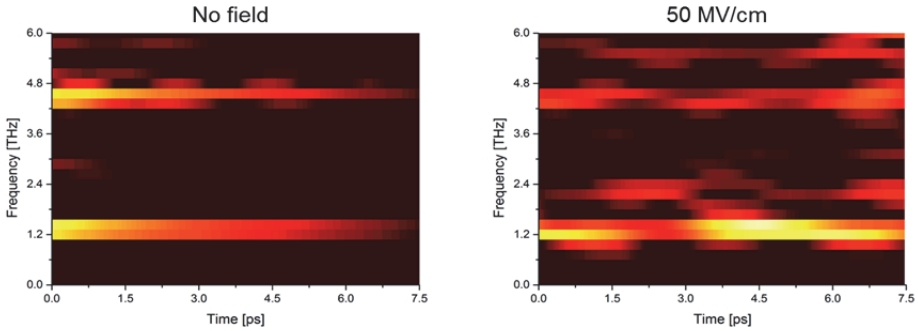

Fig. 2.15: Short-time Fourier transform (spectrogram) of the VAF calculated for the sucrose simulation without an applied field (left) and when 50 MV/cm is applied (left).

t=0 is at the positive peak of the THz field for 50 MV/cm simulation. For the spectrogram without any field applied the spectral distribution is easily identified to be similar to the VDOS for 0 MV/cm in Fig. 2.13 where the peaks at 1.38 and 4.59 THz are most significant while a few other peaks at 2.88, 5.04 and 5.77 THz are seen. When the field of 50 MV/cm is applied the spectrogram is more complicated to understand, but by comparison with the spectrogram without any field applied, the spectral features induced by a strong THz field can be explained. Looking at t=0 the peak of the 1.35 THz has shifted to 1.2 THz similar to what was also observed in Fig. 2.13. However, looking carefully, a blueshifted shoulder up to approximately 2.3 THz is observed as well, which might correspond to the expected blueshift from the steep field-modified potential as seen in Fig. 2.14 (red curve). The blueshifted mode at 2.2 THz seems to build up in intensity over the following 2-3 ps. After this the blueshifted mode shifts back into the original mode at 1.38 THz which maximizes its intensity after 4.5 ps followed by a reappearance of the blueshifted mode at 2.2 THz. Overall, this is understood as a beating between the 1.38 THz phonon and its blueshifted mode induced by the THz field. At the low-frequency side of the 1.38 THz phonon a shift appears until approximately 2 ps after the THz peak, after which a similar beating is observed. A redshift of the 1.38 THz phonon was observed as well by Walther *et al.* in [36] for high temperatures, and in vibrational spectroscopy redshifts can in general be understood as a heating effect due to the lattice expansion and population of higher levels in Morse-like vibrational potentials. The redshift observed here when the high field is applied might then be a counter effect to the blueshift, meaning that the intense THz field heats the sucrose crystal and thereby expands it

temporarily. Walther *et al.* also observed a blueshift of the same phonon when increasing the temperature from 10 to 200 K, which is here explained to be an effect of the steep steady-state potential in Fig. 2.14 (blue curve). For the peak at 4.59 THz as similar blueshift is seen, so it can be expected that the analysis for the 1.38 THz is expected to be valid for this as well. It is, however, important to note that the peak at 4.59 THz is not within the spectral bandwidth of the applied THz field (see Fig. 2.2) meaning that the THz field can non-resonantly drive the beating between frequencies by modifying the vibrational potential of the modes. Comparing the peaks appearing in the MD simulations from 0 to 4 THz (Fig. 2.13 and Fig. 2.15) directly with the THz TDS measured peaks and the DFT calculated vibrational modes in Fig. 2.1, the number of peaks in MD simulations is surprisingly small. The explanation for this is at this moment not entirely well-understood, but, besides the different temperature conditions in the THz TDS experiment, eigenmode calculation and the MD simulations, it should be noted that the MD simulations performed in this thesis do not take any selection rules into account, meaning that the simulations do not predict whether certain modes are IR or Raman active. Certainly relevant for the comparison with THz spectroscopy is the selection of IR active modes, however, the simulation times when including this increase dramatically. Nevertheless, inclusion of selection rules should result in even fewer modes, but would also give a more representative peak values. A possible explanation is that as an artifact of missing IR activity information the two peaks at 1.38 and 4.59 THz are dominating the VDOS from 0 to 6 THz and the remaining expected peaks are much weaker and thereby inseparable from the spectral noise. Fortunately, the phonon at 1.38 THz is for the following experimental study in this thesis of particular interest. While the peak values of the different peaks in each MD simulation is not exact, the relative peak values of the specific peaks from simulation to simulation is trustworthy, which is fundamental for the analysis above.

2.4. Conclusion

In this chapter it has been shown how a THz pulse can be implemented as an external field to perform field dependent MD simulations with the quantum mechanical *ab initio* software CASTEP. MD simulations with THz field strengths up to 50 MV/cm and 20 MV/cm have been performed for a unit cell and a 2x2x2 supercell of CsI, respectively, and with 50 MV/cm for a unit cell of sucrose. For the CsI unit cell, the TO phonon is identified at

1.95 THz, and when the field is increased to more than 20 MV/cm a nonlinear response of the crystal in the form of redshift and spectral broadening is observed. For the CsI supercell the VDOS spectra show more peaks due to the presence of acoustic modes and the LO phonon at 2.5 THz. When high field strengths are applied to the supercell a spectral broadening is again observed, and by studying the spectrograms calculated from the MD simulations it is seen that the spectral broadening happen within the first 2 ps of the simulation, which is while the THz field interacts with the crystal. Afterwards, the modes are beating with each other. For the more complex unit cell of sucrose mainly two peaks at 1.38 and 4.59 THz appear in the VDOS calculated from the MD simulations. For both modes the VDOS show an immediate redshift of the modes when the field strength is increased, which is contradictory with the steep vibrational potential calculated for the 1.38 THz mode, both in the steady state and with an external field of 30 MV/cm applied. However, looking at the spectrograms calculated for MD simulations with and without a field of 50 MV/cm, a blueshift induced by the strong THz field is also observed. The redshift is suspected to be a thermal effect.

With this it has been shown how this THz CASTEP module can be used for a detailed analysis and deeper understanding of nonlinear coupling between vibrational modes at THz frequencies. As an outcome from the field dependent MD simulations of sucrose presented here, a few points are made for the following experiments. Regarding the THz field strength, peak values in the order of MV/cm should be achieved in order to achieve and observe nonlinear effects. Concerning the spectral features, bleaching of the phonons is often one of the first effects seen, and might be an effect of a spectral shift. In an ordinarily recorded THz spectrum it is expected that such a spectral shift can be difficult to reveal. 2D THz spectroscopy may increase the possibility of observing nonlinear effects in terms of spectral shifts, since having two THz pulses offers the possibility of studying the beating of the modes in a time-resolved manner.

Chapter 3

Generation and detection of terahertz pulses

FTIR spectrometers are considered as the first optical systems approaching the THz regime. These were originally described in the 1960s [48] based on an incoherent, broadband light source combined with a Michelson interferometer, and covers mainly the infrared electromagnetic spectrum from hundreds of THz and down to below 10 THz. The development of coherent sources covering the lowest THz frequencies was initiated by the development of the first titanium:sapphire femtosecond laser in 1982 [49]. Already in 1975 David H. Auston published his results on gating and switching in silicon using ps pulses [50], and the technique of generating and detecting fast pulses when charge carriers are excited in semiconductor materials using an optical pulse, and subsequently accelerated by either an internal bias field for generation or an externally applied field for detection, is today also known as an "Auston Switch" [51]. With the fs pulses available from the Ti:sapphire laser for generation and detection of THz pulses with photoconductive antennas (PCA), Grischkowsky and coworkers demonstrated the first THz time-domain spectroscopy (THz-TDS) results in the late 80s [52, 53]. Today PCAs are probably the most popular solution for THz generation and detection, especially in commercial spectroscopy and imaging systems. During the early 90s the so-called optical rectification [54] of fs pulses in nonlinear crystals such as ZnTe and $LiNbO_3$ was utilized for THz generation [55, 56]. Despite the widely used term of "optical rectification" the underlying physical mechanism is considered to be difference-frequency generation (DFG) from second-order nonlinear mixing processes between the individual laser modes within the bandwidth of the pump pulse [57], as noted already in the first experimental demonstration of generation of far-infrared radiation by a picosecond laser pulse in $LiNbO_3$

[58]. Compared to THz generation with PCAs relying on carrier dynamics in semiconductors, the DFG of fs pulses in EO crystals is an almost instantaneous process giving the possibility of capturing more of the enormous bandwidth provided by optical fs pulses. In addition to the generation technique based on EO crystals, several groups published in 1996 how EO crystals also can be exploited for detection of THz pulses [59-61].

For generation of intense THz pulses the PCAs were the first sources to generate pulse energies on the order of a μJ using a table-top fs laser [62]. However, several disadvantages are associated with the PCA generation method when upscaling intensity level: the THz amplitude tends to saturate at relatively low fluences or, for large-aperture PCAs, very high bias voltages should be applied. Budiarto *et al.* reported saturation at laser fluences of 40 $\mu J/cm^2$ with large-aperture GaAs antennas using a bias of a few kV. However the saturation was avoided by increasing the bias voltage to 45 kV resulting in a THz pulse energy of 0.4 μJ [63]. At the same time Jepsen *et al.* reported damage of standard GaAs photoconductive antenna chips when using more than 60 mW from a 86 MHz repetition rate laser focused onto the chip [64]. EO crystals, on the other hand, do not require any applied bias voltage and are in most cases fairly simple to implement in a setup from an optical point of view. In 2007 ZnTe was used to generate THz pulses with energies 1.5 μJ [65] and 10 μJ was generated using a $LiNbO_3$ [66]. With $LiNbO_3$, the currently highest achieved THz pulse energy of 0.4 mJ was reported by Fülöp *et al.* where a conversion efficiency of 0.77 % was achieved [67].

Even with the near-instantaneous DFG processes in EO crystals, the bandwidth of the generated THz pulses will still be limited due to phonon resonances and phase matching conditions in the crystal. One of the newest techniques for THz generation addresses this problem simply by using air as the generation medium. The first demonstration of THz generation from a two-color air plasma was done in 2000 by Cook and Hochstrasser [68]. An Air Biased Coherent Detection (ABCD) technique using air as the detection medium was pioneered by the group of X.-C. Zhang [69]. The combination of the air-based generation and detection techniques offers spectrometers covering bandwidths of more than 100 THz [70].

In this Ph.D. project a number of different THz sources and techniques have been used. At the beginning of the project systems based on a $LiNbO_3$ source

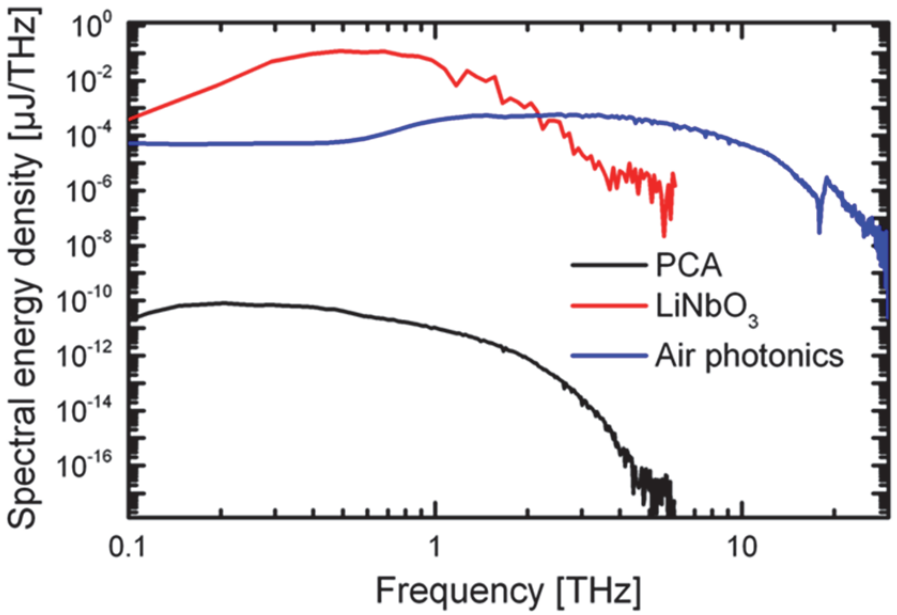

Fig. 3.1: Spectral energy density of three typical THz sources: PCA (black), 2-color air plasma (blue) and $LiNbO_3$ (red).

combined with EO detection, 2-color air plasma with ABCD detection, and a commercial system with both the generation and detection based on PCAs were available in the THz labs at DTU Fotonik. The spectral energy distributions of these three sources are shown in Fig. 3.1, where it is seen that the highest peak field energy is achieved with the $LiNbO_3$, but a broader bandwidth is achieved with the air photonics setup. The commercial PCA based setup generates pulse energies that are orders of magnitudes lower than the two other techniques, but with a very high signal-to-noise ratio (SNR), making such a system useful for linear spectroscopy in the relevant 0.05-2 THz range.

During this project two other systems based on THz generation from organic crystals (DAST, DSTMS) and 2-color air plasma with 1300 nm as the fundamental beam were built. All techniques have been demonstrated first by other groups, but the physical mechanism behind the techniques will be discussed briefly in the following. This will lead to back-to-back comparison of the different techniques where the advantages and disadvantages of each method will determine the methods used in the experiments in the following chapters of this thesis.

3.1. Photoconductive Antennas

As mentioned above the PCAs for THz generation were developed during the 80s and were used both as the source and detector in the first THz spectroscopy systems [52, 71]. One of the most common types of PCAs is the Hertzian dipole antenna where two metallic electrodes with a bias voltage applied forms a dipole with a gap separated by 5-10 µm [72] as illustrated in Fig. 3.2. The electrodes are placed on a semiconductor substrate having a bandgap matching the wavelength of the incident fs pulses, and at the same time offering a high carrier mobility and a short free carrier lifetime. In the semiconductor, light with a photon energy above the electronic energy band gap can excite electrons from the valence band to the conduction band, where the electrons are free and available to conduct current. When these electrons are created in the presence of the local DC electric field created by the applied bias voltage, they will be accelerated, and hence they emit electromagnetic radiation. If the mobile carriers are generated by a femtosecond laser pulses this radiation falls in the THz range of the electromagnetic spectrum due to the time scales of the involved dynamics. At the same time the metallic electrodes are connected by the free carriers excited in the semiconductor by the fs pulse, and with the photocurrent transients bridging the gap between the electrodes the dipole antenna efficiently radiates the generated THz-frequency electromagnetic

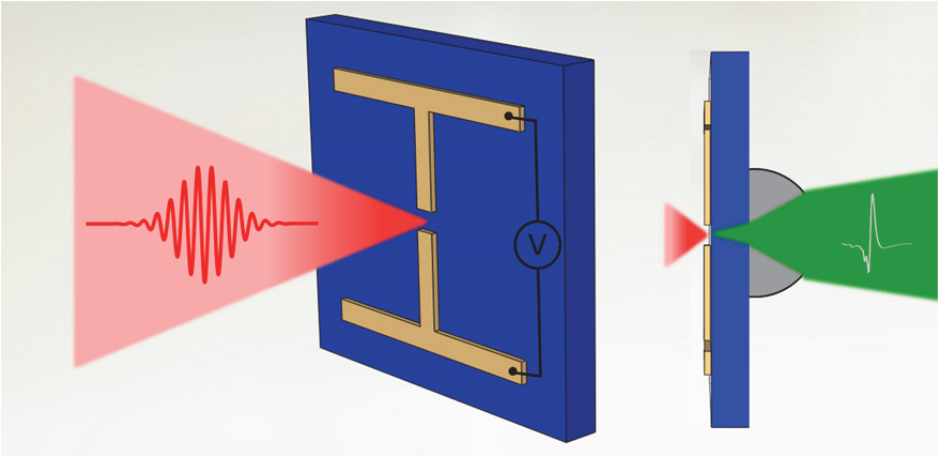

Fig. 3.2: Illustration of a biased Hertzian dipole antenna on a semiconductor (blue material) pumped by a NIR fs pulse. On the backside a silicon lens (grey) is mounted to collimate the emitted THz light.

field. The emitted THz radiation is collected and collimated by a silicon lens attached to the backside of the semiconductor. For incident fs pulses of 800 nm wavelength, low-temperature grown GaAs (LT-GaAs) is one of the most commonly used semiconductors for THz generation, while low temperature grown InGaAs (LT-InGaAs) can be used for fs laser pulses at longer wavelengths such as 1064 μm and 1550 μm. Both LT-GaAs and LT-InGaAs offer sub-picosecond carrier lifetimes [72, 73].

As mentioned in the beginning of the chapter, generation of intense THz pulses using PCAs is rather problematic. For the Hertzian dipoles antennas the achieved pulse energy is typically in the order of nJs due to clamping of the amplitude of the THz field when the fluence of the fs pulses is increased. An alternative antenna structure for overcoming this issue is using the so-called large-aperture PCA, where the electrodes are separated by a greater distance allowing for the semiconductor to be excited over a larger area. The cost of this is, however, that much higher bias voltages should be applied, and applying an electric field more than 100 kV/cm is not uncommon [74].

The main difference between the PCAs used for generation and detection is that the PCA used for detection is not biased. Femtosecond laser pulses still gate the antenna, while the simultaneously arriving THz field drives the photocurrent in the antenna. If the photoconductivity response of the detector is much faster than the duration of the THz pulse the measured current is directly proportional to electric field of the THz pulse [57]. For THz pulses generated with a dipole antenna on LT-GaAs the FWHM pulse with is typically 0.4 ps [72], and the carrier lifetime in LT-GaAs can be as low as a few hundreds fs [73] meaning that for detection a LT-GaAs PCA can directly resolve the generated THz field.

3.1.1. The Picometrix system

Even though fs pulses with the wavelength of 800 nm is suitable when using the PCAs based on LT-GaAs, having a longer wavelengths such as 1.0 or 1.5 μm opens the possibility for fiber-coupled PCAs [75] with an alternative III-V semiconductor material. The Picometrix T-Ray 4000 system is a commercial fiber-coupled THz-TDS system based on InGaAs PCAs. In a closed box an ytterbium laser is coupled to two fibers with the length of 5 m guiding the fs pulses to the THz emitter and detector PCA, respectively. Prior to the fiber coupling, the fs pulses go through free-space group-

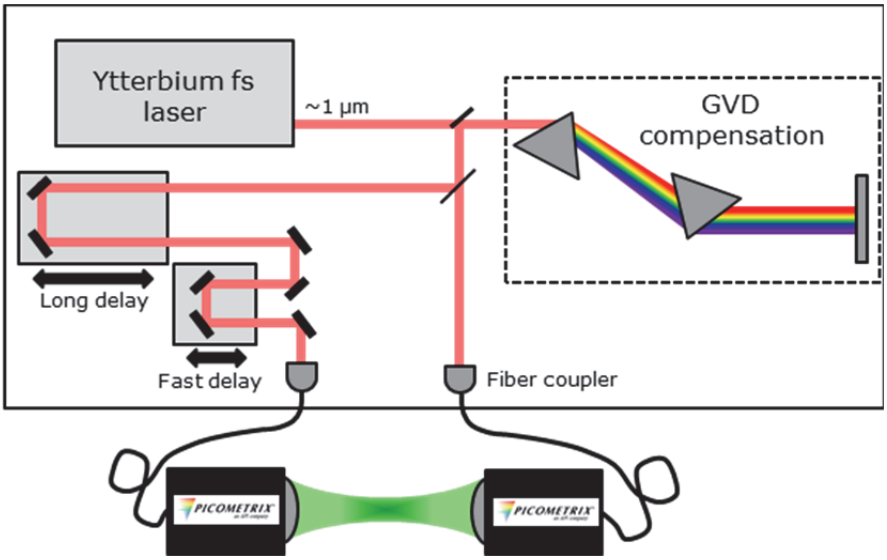

Fig. 3.3: Schematic of the Picometrix T-Ray 4000 system. Inside the box is the fs laser, group velocity dispersion compensation control and delay stages. The free-space fs pulses are coupled to the PCA modules outside the box through a 5 m long fiber.

velocity dispersion compensation and the time delay modules inside the box. A sketch of the T-Ray 4000 system is shown in Fig. 3.3.

The T-Ray 4000 is capable of recording 100 waveforms per second in a time window of 320 ps with a resolution of 78 fs. It can be used with three types of focusing polyethylene lenses having a focal length of 1", 3" and 6", respectively. The shorter the focal length, the tighter the THz beam can be focused, but at the same time, the more material is introduced in the THz beam by the thicker lenses, leading to somewhat lower performance at the highest frequencies. A typical waveform recorded with the 3" lenses averaged over 10,000 waveforms is shown in Fig. 3.4, where the spectral coverage is up to approximately 2 THz, and the peak dynamic range is approximately 60 dB (1000:1 in signal amplitude).

As a spectroscopy setup the main advantage of most commercial PCA systems is the fast recording of waveforms giving the possibility of acquiring thousands of waveforms in a few minutes. This is particularly useful in cases where the transmission through a sample is low. At the same time a portable fiber-coupled emitter and detector are not critically sensitive to alignment performed by the user, and they simplify a spectroscopy setup significantly

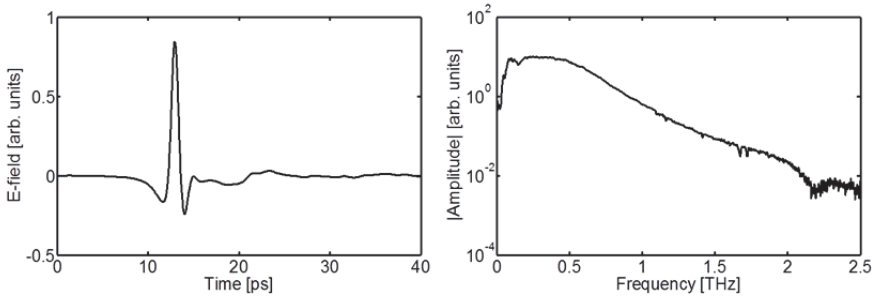

Fig. 3.4: Average over 10,000 waveforms recorded with Picometrix T-Ray 4000 (left) and corresponding spectrum (right).

compared to similar free-space setups. By using a pellicle beam splitter the system can also be used in a reflection geometry. The combination of the portability of the system together with the flexibility to easily change between transmission and reflection detection means that it, besides spectroscopy, has also been used to investigate hidden layers in artwork outside of the lab [76, 77].

3.2. High-power THz generation

While the Picometrix T-Ray system is based on a standard fs oscillator, the methods described in the following subsections for generation of intense THz pulses critically relies on amplified fs laser pulses. Therefore this subsection will first describe the performance of an amplified fs laser system before exploring the techniques used for intense THz pulse generation and detection.

3.2.1. Amplified laser systems

The experiments performed in the high-power lab at DTU Fotonik have been done using two amplified fs laser systems, both from Spectra-Physics: the Spitfire Ace and Spitfire Pro XP which were installed in 2013 and 2009, respectively. Both systems are Ti:sapphire regenerative amplifiers working with a repetition rate of 1 kHz but have the possibility of working at lower repetition rates, which is crucial for the organic crystals as explained in section 3.2.2.2. The Spitfire Ace delivers 6 mJ pulses with a pulse duration of approximately 120 fs while the Spitfire Pro XP gives 3.5 mJ pulses with a pulse duration of 35 fs. It is possible to change the pulse duration of both amplifiers between 35 and 120 fs by changing the gratings for appropriate pulse stretching and compression. The short pulse duration is ideal for two-

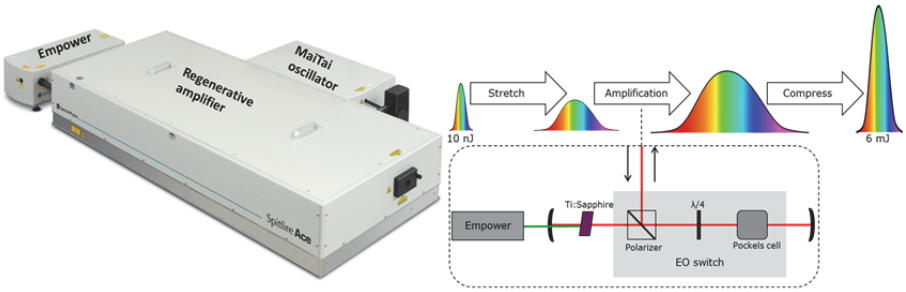

Fig. 3.5: The Spectra-Physics Spitfire Ace fs amplified laser system (left, source: www.newport.com) together with an illustration of the CPA technique (right). The inset illustrates the regenerative amplification process, where the pulses are amplified by the Ti:sapphire gain crystal pumped by the Empower. After sufficient amplification the pulses are let out by the EO switch consisting of a Pockels cell, quarter wave plate (λ/4) and a polarizing beam splitter [3].

color air plasma generation and for this reason the Spitfire Pro XP is commonly used for the THz generation using a 2-color air plasma with 800 nm as the fundamental beam. THz generation in $LiNbO_3$ is more efficient with longer pulse durations so for this reason the Spitfire Ace is mainly used for pumping the $LiNbO_3$ based setups. The Spitfire Ace can be coupled to a Light Conversion TOPAS-Prime optical parametric amplifier (OPA) system giving the possibility to convert the fundamental wavelength of 800 nm to any wavelength between 150 to 4000 nm. The TOPAS-prime is most efficient when converting the 800 nm pump wavelength to the signal wavelength at 1300 nm. When pumping the TOPAS-prime with pulses of 6 mJ at 800 nm, pulses of approximately 1 mJ can be achieved at 1300 nm. It should be noted that the pulse duration is decreased to 70 fs during the conversion process due to nonlinear effects.

A regenerative amplifier system consists of three parts: an oscillator, a pump and the amplifier itself. The main differences between the Spitfire Ace and the Spitfire Pro XP are the Ti:sapphire fs oscillator and the pump. Firstly, the Spitfire Ace has a MaiTai XF-I oscillator which is a hands-free laser, while the Tsunami oscillator in the Spitfire Pro XP system requires manual mode-locking by adjusting a slit-prism pair. The hands free feature of the MaiTai gives a surprisingly high stability of the amplified system. Secondly, and most importantly, the delivered average power of the Empower pump, which is a green pulsed diode laser, is higher in the Spitfire Ace system. The

Spitfire Pro XP pump laser has an average power of 30 W, while the Spitfire Ace pump delivers an average power of 45 W. In the following the Spitfire Ace system is described. Besides a few design improvements in the Spitfire Ace, the principle of the amplification process itself is similar for the two systems. As shown in Fig. 3.5 the Spitfire Ace has the MaiTai oscillator, the Empower pump and the amplifier itself in three separate boxes. The MaiTai produces pulses of 10 nJ in a repetition of 80 MHz. After leaving the MaiTai the pulse train passes through a 5/95 beamsplitter, where 95% of the beam goes to the amplifier while 5% can be used for EO sampling as explained in section 3.3.1. The amplification is done using the chirped pulse amplification (CPA) technique [78] as illustrated in the right part of Fig. 3.5. When the pulses enter the amplifier a grating pair stretches the pulses before the amplification, and is again compressed by another grating pair after the amplification. In this way damage of the Ti:sapphire crystal in the gain cavity due to high peak power can be avoided. A simplified illustration of the amplification is shown as the inset in Fig. 3.5. The stretched pulses are sent to the regenerative cavity where the Ti:sapphire gain crystal is pumped by the Empower, and the pulse energy will increase according to the number of roundtrips in the cavity. When the pulse energy is sufficiently high, the pulses are coupled out of the cavity again due to the electro-optic effect in a Pockels cell, which, together with a quarter waveplate and a polarizer, works as an optical switch [3]. With the amplification and recompression, the pulses have increased their pulse energy from 10 nJ to 6 mJ, and with the pulse duration of 120 fs this corresponds to a peak power of 50 GW.

3.2.2. Optical rectification

THz generation in a nonlinear crystal is often referred to as optical rectification. In the case of monochromatic light this is a DC response rectified by the incoming field, while for fs pulses the optical rectification performs a DFG mixing of combinations of frequencies within the bandwidth of the pulse [79]. The nonlinear behavior originates from the material failing to respond in a linear way when a sufficiently strong optical field is applied. Second order nonlinear effects are only present in non-centrosymmetric since the second order nonlinear susceptibility $\chi^{(2)}$ vanishes for centrosymmetric materials. Silica, which is the most common material for fabrication of optical fibers, is an example of a centrosymmetric material [80], so the second order effects are rarely discussed in nonlinear fiber optics. Non-centrosymmetry typically means that the charge density

distribution of a material on the molecular level is asymmetric. In EO crystals this is often caused by the difference in electronegativity between the atoms in the molecular structure. For example, for ZnTe the electronegativity is higher for Te than for Zn meaning that the charge distribution inclines towards Te hence the potential energy surface becomes asymmetric [72].

The second order nonlinear polarization in a non-centrosymmetric material is written as

$$\tilde{P}^{(2)}(t) = \epsilon_0 \chi^{(2)} \tilde{E}(t)^2 . \tag{3.1}$$

In a simplified case an optical pulse can be described as a single oscillating frequency with a time dependent amplitude i.e.

$$E(t) = E_0(t) e^{-i\omega t} . \tag{3.2}$$

If the pulse duration is much longer than the optical period, the polarization induced by the optical rectification process reproduces the envelope of the pulse. Now, the electric field induced by optical rectification of optical field in a non-centrosymmetric material can be found by solving the wave equation. If the amplitude i.e. the envelope of the optical pulse in the medium is Gaussian it can be written as [72]

$$E_0(z,t) = E_0 \exp\left(-a\left(t - \frac{z}{v_0} \right)^2 \right) \tag{3.3}$$

where a determines the width of the pulse, z is the length of the nonlinear medium and v_0 is the velocity of the optical pulse in the medium i.e. $v_0 = c/n.$ With this, the solution of the wave equation gives that the optically rectified electric field proportial to the second-order time derivative of the Gaussian waveform specifically written as

$$E_{OR}(z,t) = Al\left[1 - 4a\left(t - \frac{z}{v_O} \right)^2 \right] \exp\left[-2a\left(t - \frac{z}{v_O} \right)^2 \right] \tag{3.4}$$

where A is a constant defining the amplitude and l is the propagation length. When considering Gaussian optical pulse with a FWHM of 100 fs, the

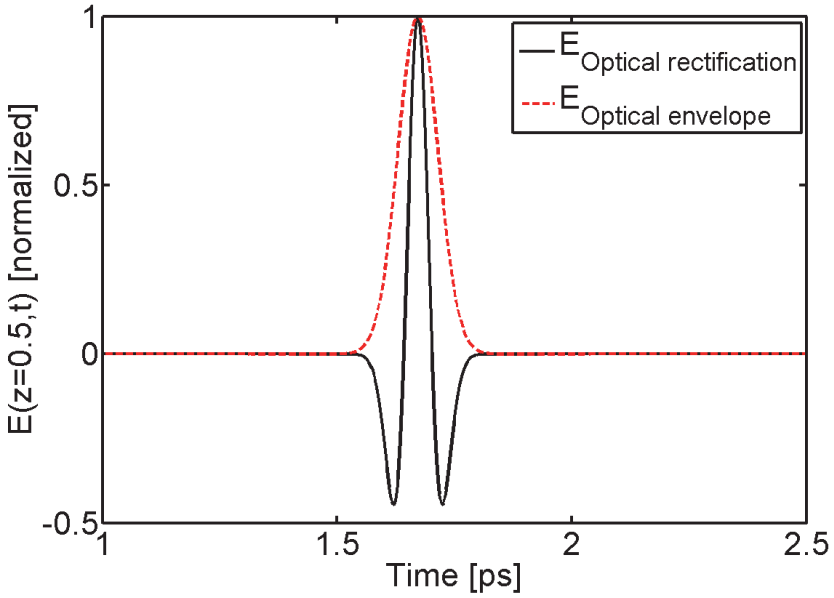

Fig. 3.6: Electric field induced by optical rectification (black line) of a Gaussian fs pulse (red dashed line) in the center of a 1 mm thick ZnTe crystal.

electric field generated by optical rectification in a 1 mm thick ZnTe crystal (n=2.85 at 800 nm [81]) after the propagation of 0.5 mm is calculated as the black line in Fig. 3.6. For a qualitative comparison this calculation represents the time-dependent shape of a THz pulse well. The red, dashed line in Fig. 3.6 respresents the envelope of the Gaussian pulse from which the THz field is rectified through the second order nonlinear polarization, while the oscillating component insignificant for optical rectification has been left out (having a period of 2.67 fs at 800 nm).

The simplified example discussed above does not consider dispersion, and the possibility of DFG has been left out. In order to include this, the electric field of a fs laser pulse is written in frequency domain, and equation (3.2) is substituted with

$$E(t) = \int_0^\infty E(\omega) e^{-i\omega t} d\omega + c.c. \tag{3.5}$$

and inserted into equation (3.1) [82] so that

$$P_{NL}^{(2)} = 2\int_0^\infty \int_0^\infty \chi^{(2)} E(\omega_1) E^*(\omega_2) e^{-i(\omega_1-\omega_2)t} d\omega_1 d\omega_2 + c.c. \qquad (3.6)$$

Effects of sum-frequency generation and second-harmonic generation have been left out while DFG is now included. For this case the coupled nonlinear wave equations have been solved in [83, 84] resulting in the solution for the generated THz field in frequency domain

$$E_{THz}(\Omega, z) = \frac{\Omega^2 e^{ik(\Omega)z}}{k(\Omega)c^2} \int_\infty^\infty \chi^{(2)} E(\omega+\Omega) E^*(\omega) \frac{e^{i\Delta kz} - 1}{\Delta k} d\omega \qquad (3.7)$$

where z is the crystal length, Ω is the difference frequency between two optical frequency components and Δk is the phase mismatch between the three frequencies i.e. $\Delta k = k(\omega_2) - k(\omega_1) - k(\Omega)$.

Equation (3.7) can be understood as DFG mixing of frequencies in the entire bandwidth of the incoming laser pulse can happen in a nonlinear non-centrosymmetric medium as long as the phase matching condition is fulfilled i.e. $\Delta k \approx 0$. Nevertheless, the bandwidth can also be limited by absorption in the specific material. For example ZnTe has a strong absorption above 3 THz due to a TA phonon at 3.7 THz and a TO phonon at 5.3 THz [85] limiting the THz bandwidth possible to generate and detect with ZnTe. This absorption is possible to include by using a frequency dependent expression for $\chi^{(2)}$ and the complex-valued $k(\Omega)$ [84].

For the reference, the DFG process resulting in a frequency component of 3 THz can for example be achieved when mixing the center the fs laser pulse at 800 nm with a second wavelength of 793.6 nm. A 100 fs transform-limited pulse from a Ti:sapphire laser has a bandwidth of 21 nm, so the second wavelength needed for DFG generation of light at 3 THz will be contained in such a fs pulse. As discussed in the section below about THz generation in $LiNbO_3$ it can be an advantage to limit the bandwidth of the fs laser pulse so that the possible DFG processes only result in THz frequencies in the bandwidth where the EO crystal has low absorption and good phase matching.

3.2.2.1. THz generation with $LiNbO_3$ crystals

Lithium niobate ($LiNbO_3$) is one of the most popular choices for generation of intense THz pulses with amplified laser systems. $LiNbO_3$ is a ferroelectric

material with a very high nonlinear coefficient, d_{eff}, of 168 pm/V at 800 nm, which is more than twice as much as for ZnTe [86, 87], and at the same time the damage threshold is high when the crystal is doped with a few percent of MgO [88]. The drawback of using $LiNbO_3$ for THz generation is that the refractive index for THz light is much larger than the group refractive index of the fs pulse at 800 nm (5.2 versus 2.2). This means that the phase matching in a collinear geometry will be extremely poor since the phase velocity of the THz pulse, υ_{THz}, will be much slower than the group velocity of the incoming fs laser pulse, υ_{NIR}^{gr}. To overcome this, the tilted-pulse-front technique was proposed, where a non-collinear geometry is used to improve the phase matching and thereby give a longer interaction length in the crystal [89]. When tilting the pulse front of the incident NIR light, the phase matching condition is modified so that the velocity of the THz light in the $LiNbO_3$ crystal is matched with the group velocity of the NIR beam projected onto the tilt direction written as

$$\upsilon_{NIR}^{gr} \cos\gamma = \upsilon_{THz}, \tag{3.8}$$

where γ is the angle of the tilt. In practice, it is possible to perform a tilt of the pulse front by using a grating [90] and subsequently image the pulse front onto the crystal with a telescope [66]. In [90] it was shown as well that the optimum value for γ should match the Cherenkov angle which is between 61^o and 63^o in order to achieve the most efficient THz generation in a bandwidth from 0.1-3.5 THz. These angles have been confirmed by imaging of the pulse front while propagating the crystal [91, 92]. In [91] it was shown that the THz amplitude decays rapidly for lower angles than 61^o and only gradually for larger angles.

Based on the work from Yeh *et al.* in [66] where 10 μJ of THz was generated with $LiNbO_3$, the tilted pulse front method has been implemented in the THz labs at DTU Fotonik. A sketch of this setup is shown in Fig. 3.7 where the inset is a zoom of the $LiNbO_3$ crystal showing the tilt of the pulse front. Using a grating with 2000 lines/mm and having an incident angle of the NIR beam into the grating of approximately 66.6 degrees, the pulse tilt is calculated to be 63^o. The tilted pulse fronts are imaged onto the $LiNbO_3$ crystal with a lens pair with focal lengths of 150 mm and 75 mm, giving a demagnification factor of 2. A λ/2 plate is used to rotate the polarization of

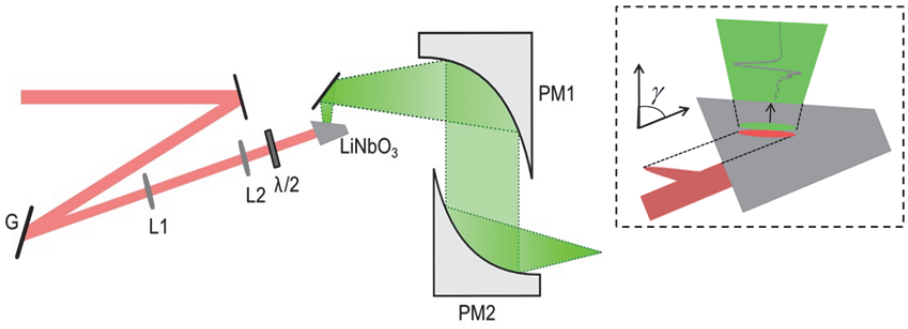

Fig. 3.7: Setup for THz generation in a $LiNbO_3$ crystal using the tilted-pulse-front method. 120 fs pulse fronts are tilted by a 2000 lines/mm grating and imaged onto the crystal where the THz radiation is generated. L1: 300 mm cylindrical lens, L2: 75 mm lens, PM1: 7" off- axis parabolic mirror, PM2: 4" off- axis parabolic mirror. The inset shows a zoom of the crystal illustrating the pulse tilt relative to the non-collinear propagation of the NIR and the THz beams.

NIR beam from horizontal to vertical so that it is parallel to the optical axis of the crystal.

In the configuration shown above, the generated THz light is collimated and focused to the sample spot with a pair of off-axis parabolic mirrors, PM1 and PM2, with focal lengths of 7" and 3", respectively. The choice of a focal length of 7" for PM1 was based on the assumption that the THz beam diverges slowly when being emitted from the $LiNbO_3$ crystal. In 2011 Hirori *et al.* [93] proposed an improved scheme for focusing of the THz light generated in a $LiNbO_3$ crystal, where three off-axis parabolic mirrors were used. Here, the THz beam was considered as a collimated beam when emitted from the crystal. The first off-axis parabolic mirrors had a focal length of only 10 mm, leading to rapid expansion of the THz beam after the intermediate focus. The second parabolic mirror with a focal length of 4" was re-collimating the expanding beam, and the third parabolic mirror with a focal length of 2" was then finally focusing the beam tightly. With this scheme, field strengths of more than 1 MV/cm were achieved.

Several improvements have been suggested for THz generation with $LiNbO_3$. The absorption of THz frequencies in the $LiNbO_3$ crystal is fairly high at room temperature, but can be reduced by cryogenic cooling. Calculations have predicted that the conversion efficiency could be raised

from a few percent up to more than 13% when cooling down to 10 K [94]. Experimentally, a conversion efficiency of 3.8% have been demonstrated when cooling down to 150 K, while the efficiency was saturated at lower temperatures [95]. At the same time this result was achieved with 1030 nm pulses since the three-photon absorption is reduced when the wavelength is increased [96]. As discussed previously, having a transform-limited pulse it is advantageously to increase the temporal duration and thereby reduce the bandwidth of incident pulses so that the duration should be even larger than the 120 fs pulse duration delivered from the Spitfire Ace. In [94] the optimum pulse duration was predicted to be around 500 ps, and in [97] the conversion efficiency increased when using up to 240 fs long pulses, however, the efficiency was saturated for longer pulses. Here, it was also measured that the THz generation causes a redshift of the incident 800 nm pulse after which Kerr-like effects prevents any further THz generation to occur.

3.2.2.2. THz generation with organic crystals

One of most nonlinear EO crystals is the organic salt DAST (dimethyl amino 4-N-methylstilbazolium) with a reported nonlinear coefficient of 615 pm/V [98]. At the same time DAST is, in contrast to $LiNbO_3$, ideally used in a collinear configuration, which significantly simplifies the geometry of the experimental setup. THz generation with DAST was first done by Xi-Cheng Zhang and coworkers in 1992 [99], where the crystal was pumped with 10 nJ pulses at 800 nm. Already at that time it was observed that the THz signal generated with DAST was more than 40 times stronger than the best unbiased semiconductor samples. A problem with the THz spectrum generated from DAST was limited by a strong phonon resonance at 1 THz [100]. Later it was suggested to pump the DAST crystals with longer wavelengths than the 800 nm generated from the Ti:sapphire laser in order to achieve phase matching at frequencies higher than 1 THz [98, 101]. When pumping DAST with fs pulses having a center wavelength from 1300 to 1600 nm, the phase matching is ideal for THz generation between 2 to 7 THz.

An alternative to DAST is the DSTMS (4-N,N-dimethylamino-4′-N′-methyl-stilbazolium 2,4,6-trimethylbenzenesulfonate) crystal [102, 103] having a chemical composition similar to DAST, but the phonon absorption around 1 THz is less pronounced [104]. As it will be shown in Chapter 6 of this thesis

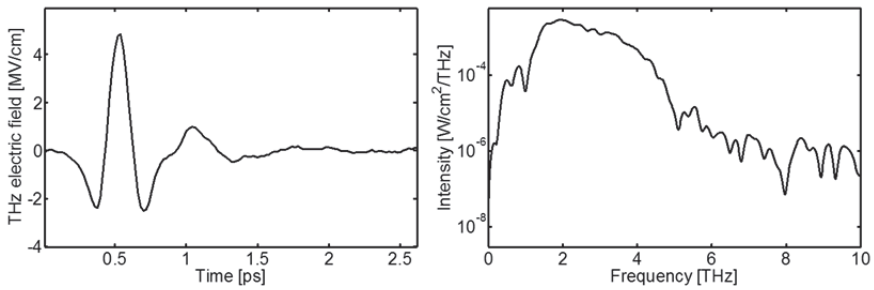

Fig. 3.8: Waveform and corresponding spectrum measured (with ABCD) form DSTMS when pumped with 1 mJ pulses at 1300 nm.

the THz spectrum generated from DSTMS is smoother than from DAST, and DSTMS gives a higher peak field intensity.

A disadvantage of the organic crystals is the low damage threshold, which is approximately 20 mJ/cm^2 [105]. To prevent thermal heating of the crystals they should be pumped with low repetition rates around 100 Hz when the pump pulse energies are approaching the mJ level. Recently organic crystals have been used for generation of intense THz pulses, where pulse energies of more than 100 µJ have been measured when pumping with 3.8 mJ pulses at 1500 nm [106].

As a new technique in the labs at DTU Fotonik, THz generation from DAST and DSTMS has been implemented with crystals purchased from Rainbow Photonics. DSTMS had an aperture of 3 mm and a thickness of 460 µm, and DAST had an aperture and thickness of 4 mm and 560 µm, respectively. Both crystals had a broadband AR coating centered at 1350 nm. Having the smoothest spectrum and highest peak field intensity, DSTMS was preferred for 1D THz spectroscopy. An example of a waveform and corresponding spectrum is shown in Fig. 3.8. Here, the THz pulse energy measured with a pyro-electric detector from QMC Instruments was approximately 10 µJ when the DSTMS crystal was pumped with 1 mJ pulses at 1300 nm. Both the DSTMS and DAST crystals are used for the 2D THz setup as explained in Chapter 6.

3.2.3. THz generation with two-color air plasma

THz generation from a two-color air plasma is the final as well as the historically youngest method to be discussed in this chapter. This method relies on the ability to ionize air with intense laser pulses, and for this reason

it was first demonstrated using an amplified Ti:sapphire laser system [68]. Today, most air plasma THz systems together with the setups discussed here are based on fs laser pulses with pulse energies in the order of mJs, nevertheless micro-plasmas emitting coherent THz radiation have been generated using 800 nm pulses with low pulse energies on the order of μJs by Buccheri and Zhang [107, 108]. A two-color air plasma is generated when a fs pulse is focused together with its second harmonic with pulse energies high enough to ionize the air (experimental details will be discussed in Chapter 3). The physical mechanisms behind the THz generation from such a two-color plasma have been widely discussed. The first interpretation explained the emission mechanism as a four-wave mixing process meaning that $E_{THz} \propto \chi^{(3)} \sqrt{E_{2\omega}} E_{\omega}$. Later, when experimental results revealed that the spatial profile of the THz radiation emitted from the air plasma was conical [109-112], You *et al.* explained this pattern with the so-called photocurrent model. This model was earlier used to explain the THz radiation from a tunnel ionization leading to an electron current in a symmetry-broken electric field [113]. In a two-color air plasma the symmetry of the electric field is broken in a similar manner by the coherent superposition of the second harmonic (2ω) and the fundamental beam (ω). Thus, acceleration of the electrons by the asymmetric optical field in the 2-color plasma is the source of the broadband THz radiation. With the fact that most plasmas used for efficient THz generation typically have a length of tens of mm, You *et al.* suggested an off-axis phase matching condition depending on the length of the plasma. The spatial properties of THz beams used for spectroscopy are of great importance to take into account, and for this reason the beam profiles from two-color air plasmas have been studied extensively in Chapter 4.

Due to the very good broadband phase matching between the involved optical fields in the ionized air (here 800 nm, 400 nm, and THz, where the refractive index is close to 1), the range of frequencies where the off-axis phase matching conditions mentioned above can be met is extremely wide, and for this reason air plasmas are the THz sources offering the widest bandwidths. Equally important is that, in contrast to EO crystals, the bandwidth in a plasma is not limited by phonon absorption and dispersion. The bandwidth of the generated THz pulse is essentially only limited by the bandwidth of the fs pulse creating the air plasma, and for this reason THz spectra with bandwidths of hundreds of THz have been achieved [70].

In general, 2-color air plasma where 800 nm is the fundamental wavelength is less efficient in terms of total generated THz energy, than using EO crystals. The conversion efficiencies of the above mentioned organic EO crystals were up to a few percent, where the highest conversion efficiency for a typical 2-color air plasma is on the order of 10^{-4} [114]. Experiments where plasmas have been generated by ionizing alkali vapors have successfully shown an improvement of the conversion efficiency since atoms of Rb and Cs have a lower ionization potential than air (N_2) [115]. However, the alkali atoms in the gas phase tend to cluster at higher pressures, so at this moment the experiment has only been performed for pressures less than 1 mbar.

3.2.3.1. Long wavelength two-color air plasma

Another method for increasing the conversion efficiency is to increase the wavelength of the fundamental beam generating the air plasma together with its second harmonic. The idea of increasing the generation wavelength for higher conversion efficiency has already been applied in the field of attosecond science for high harmonics generation using mid-IR pulses [116] since the laser induced ponderomotive energy scales as λ^2 [117]. For THz generation this was implemented by Clerici *et al.* where a model including this wavelengths scaling due to the ponderomotive force, but also due to a focusing effect was presented [118]. The focusing of a beam with a larger wavelength will fundamentally result in a larger focus volume having a positive effect on the THz generation efficiency. With this, Clerici and coworkers achieved a wavelength scaling factor of $\propto \lambda^{4.6}$ in good agreement with their experimental results from 2-color-plasmas generated with

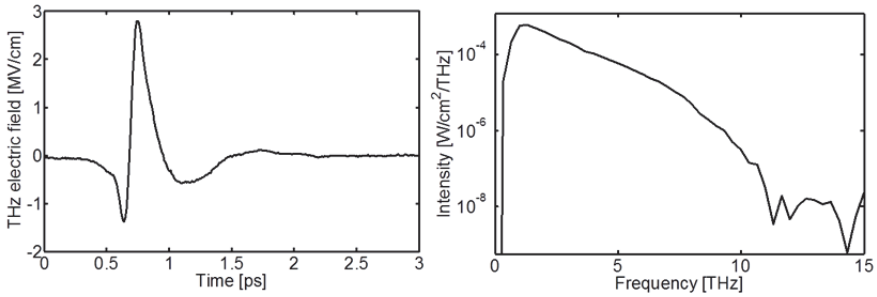

Fig. 3.9: Waveform and corresponding spectrum measured (with ABCD) from a 2-color air plasma using 1300 nm as the fundamental, with a pulse length of 70 fs.

wavelengths up to 1.8 μm for the fundamental beam.

During this project THz generation with a 2-color air plasma having 1300 nm as the fundamental wavelength was successfully achieved when pumping with 1 mJ, 70 fs pulses, where the resulting spectrum is seen in Fig. 3.9. Here a 100 μm thick BBO cut with $\theta=19.8^{o}$ giving relatively flat phase matching conditions around 1.5μm was used, and it should be noted that similar results cannot be achieved with a BBO phase matched at 800 nm. A field strength of 2.8 MV/cm is measured at the focus of a 2" off-axis parabolic mirror by measuring the power with pyro-electric detection (280 nW) and the beam spot size with the NEC THz camera found to be $(\sigma_x = 86.5\mu m, \sigma_y = 81.8\mu m)$ where σ is the Gaussian standard deviation. The time-domain trace is measured with ABCD detection.

3.3. High-power THz detection

For detection of intense THz pulses the EO sampling and ABCD detection techniques have been used in this work. As explained in section 3.1, photoconductive can be used for both generation and detection, and the same applies for the high-power techniques discussed above: both EO crystals and air can be used for detection as well. In the following the two detection techniques are explained.

3.3.1. Electro-optic sampling

EO sampling is probably the most commonly used technique for detection of intense THz pulses. This technique relies on the Pockels effect meaning that a THz pulse can induce a change in the birefringence in an EO crystal [55]. A sketch of a typical EO sampling configuration is shown in Fig. 3.10. The THz light is focused onto an EO crystal (EOC) where it is sampled by the 800 nm beam. If the THz beam is absent the quarter wave plate ($\lambda/4$) behind the EO crystal changes the polarization of the 800 nm light from linear to circular. Then the horizontal and vertical polarization components will be spatially separated by the Wollaston prism (WP). Each polarization component will be detected on two photodiodes, PD1 and PD2. The difference in the intensity of the two beams will be detected on a lock-in amplifier (or another electronic math module measuring the difference signal). The detection is "balanced" meaning that the quarter wave plate is

adjusted so that difference signal is zero when the THz signal is blocked. If the THz pulses arrive simultaneously on the EO crystal, a birefringence is induced by the THz beam resulting in a polarization change proportional to the strength of the THz field. After the quarter wave plate the polarization of the 800 nm beam is now elliptical causing an imbalance of the two polarization components, which is detected on the photodiodes. The full THz waveform can be sampled when this imbalance is measured as the 800 nm beam is scanned in time over the THz wave form. The THz induced phase retardation of the elliptically polarized 800 nm light is given by

$$\Gamma = \frac{\omega n_0^3 r_{41} L}{c} E_{THz}, \tag{3.9}$$

where n_0 is the linear refractive index, r_{41} is the electro-optic coefficient and L is the thickness of the crystal. Using that the difference signal (ΔI) over the total signal at each photodiode I_0 is equal to the sine of the phase retardation i.e. $\frac{\Delta I}{I_0} = \sin(\Gamma)$, the THz field is calculated as

$$E_{THz} = \arcsin\left(\frac{\Delta I}{I_0}\right)\frac{c}{\omega n_0^3 r_{41} L} \approx \frac{\Delta I}{I_0}\frac{c}{\omega n_0^3 r_{41} L} \tag{3.10}$$

where the last approximation is made for weak THz fields where $|\frac{\Delta I}{I_0}| < 0.5$ [119]. In practice, the signal on each of the photodiodes is limited by the laser induced damage threshold of the EO crystal and the photodiodes

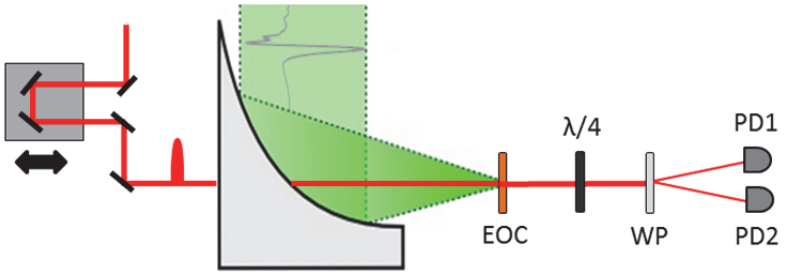

Fig. 3.10: Schematic of EO sampling setup. The NIR beam overlaps with the THz beam in the EO crystal (EOC), and the horizontal and vertical polarization states are separated by a quarter wave plate (λ/4) and a Wollaston prism (WP) and detected on the photodiodes PD1 and PD2.

themselves, so for intense THz pulses the field strength is attenuated so that approximation above is still valid.

Even without the approximation, the rotation of the polarization induced by the THz beam should be less than 90^o in order to observe an increase in the measured signal ΔI when the THz field is increased. The phenomena where the THz field strength is so strong that the polarization of the 800 nm beam is rotated more than 90^o is known as "over-rotation" and is, as mentioned above, avoided by attenuating the THz beam until a linear detection regime is reached. Most often this is done by inserting silicon wafers in the collimated beam path, since the wafers transmit only of 70% of the THz field per inserted wafer, due to Fresnel losses in the linear detection regime.

ZnTe is a popular choice for THz detection, but as mentioned previously, its bandwidth for generation as well as detection is limited due to absorption features. For this reason GaP has been used for EO detection offering a broader bandwidth than ZnTe [120]. Detection with a 300 μm GaP crystal covered the bandwidth generated with DSTMS i.e. at least beyond 5 THz.

3.3.2. Air-biased coherent detection

Air-biased coherent detection (ABCD) is the detection equivalent to the two-color air plasma generation method. Similarly, ABCD gives the best possible bandwidth due to the absence of phonon absorption and dispersion in air, but the understanding of the physical mechanism responsible for ABCD is significantly different from the photocurrent model discussed for THz generation from 2-color air plasmas. ABCD relies on the fact that a THz field can modulate the generation of the second harmonic of the fundamental beam in a four-wave mixing process i.e.

$$E_{2\omega} \propto \chi^{(3)} E_{\omega} E_{\omega} E_{THz} . \tag{3.11}$$

In the same way as a THz field, a strong DC field can also induce a second harmonic signal. If both a DC field and the THz field are applied, the total second harmonic field is

$$E_{2\omega} \propto \chi^{(3)} E_{\omega} E_{\omega} (E_{THz} + E_{DC}) . \tag{3.12}$$

The intensity of this second harmonic beam which is detected in an ABCD setup is then

$$I_{2\omega} \propto |E_{2\omega}|^2 \propto \left(\chi^{(3)} I_{\omega}\right)^2 \left(E_{THz}^2 + 2E_{THz}E_{DC} + E_{DC}^2\right). \quad (3.13)$$

If the DC field is applied so that it is constant over the entire laser pulse but changes its sign at every second pulse, the second crossterm in (3.13) can be isolated and detected with a lock-in amplifier i.e.

$$I_{2\omega} \propto |E_{2\omega}|^2 \propto \left(\chi^{(3)} I_{\omega}\right)^2 2E_{THz}E_{DC} \quad (3.14)$$

This means that the applied bias should be a square wave function with the frequency of the first sub-harmonic of the laser repetition rate i.e. 500 Hz for a 1 kHz amplified laser system. This is illustrated as in the inset below the biased electrodes in Fig. 3.11. The NIR and THz beams are focused between the electrodes where they are spatially overlapped. The amplitude the DC field is typically in the order of 1 to 8 kV generated by a function generator together with a high-voltage amplifier. The second harmonic beam can be detected with a photomultiplier or, alternatively, an APD used together with

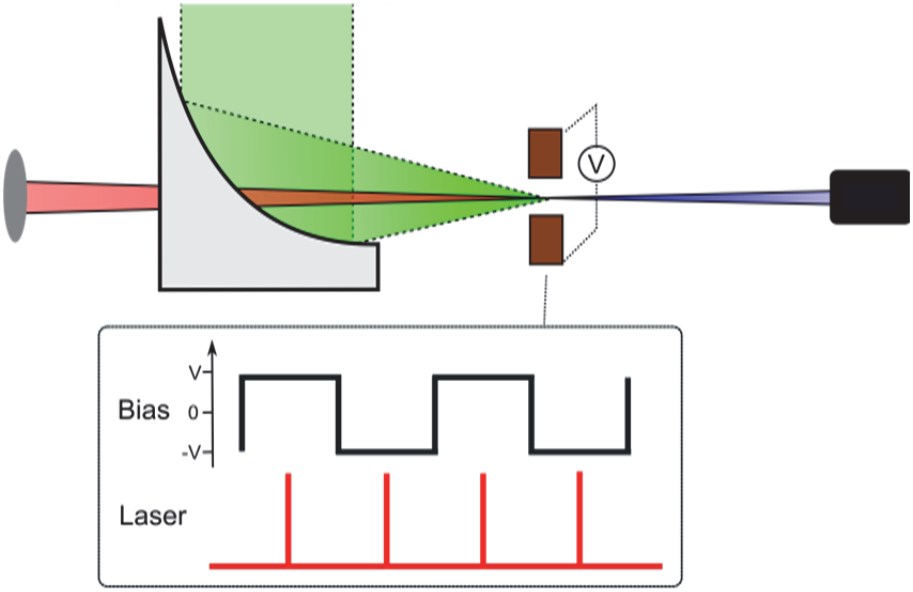

Fig. 3.11: Schematic of the ABCD setup. The NIR beam is focused by a lens and overlapped with the THz beam focused by an off-axis parabolic mirror. Two electrodes apply a bias voltage over the focus in the same plane as the polarization of the NIR beam. Blue light is detected with a PMT or an APD.

a boxcar integrator with a window width of a few nanoseconds, since the response of the APD alone is too fast for efficient lock-in detection at such low repetition rates. At the same time the boxcar can significantly improve the SNR (signal-to-noise ratio) since the noise from the laser in between the pulses is eliminated. The usage of boxcars for initial signal preparation will be discussed further in Chapter 6. The spectrum showed in Fig. 3.9 was recorded with ABCD using the Spitfire Ace system with 100 mW of the 800 nm amplified pulses focused by a 200 mm biconvex lens.

Since the first ABCD demonstration in 2008 [69], spectrometers based on this has been used for ultra-broadband THz spectroscopy on different samples of polymers [121], soft glasses [122], graphene [123] Si nanoparticles [124], solar cell materials [125] and water [126]. Together with the wide bandwidth where more than 30 THz have been transmitted through a thin water film [126], the absence of etalon effects from EO crystals is a big advantage for spectroscopy. However, the sensitivity of ABCD is significantly lower than for EO sampling meaning that the SNR of an ABCD recorded spectrum is typically no more than a few hundreds, while with EO sampling more than a thousand can be achieved.

3.4. Summary – Pros and cons of generation and detection methods

In this chapter a number of different methods for THz generation have been discussed, and all have been considered for the experiments performed in this thesis. For every experiment it is important to choose an appropriate source and detection method depending on the needs in the specific case. In the following the advantages and disadvantages for each source will be described, which is also given as an overview in Table 1.

The first THz system discussed in this chapter was the commercial PCA based system Picometrix T-Ray 4000. Here, the pulse energies are more than 10^6 times lower than what can be generated with the techniques based on the amplified laser systems presented in section 3.2, and in practice, the spectral coverage is only up to approximately 2 THz. Nevertheless, the fast waveform acquisition is advantageous for high-quality linear spectroscopy in this range, allowing for averaging over ten thousand of waveforms in less than 2 minutes, which is approximately the same time taken to record a single waveform over a much shorter time window with a 1 kHz system. In

Chapter 5 where field enhancement inside micro-slits is investigated, the Picometrix system is ideal for this experiment. For characterization of the field enhancement itself, the incident field strength is less important, and the resonances of the slits can easily be designed within the bandwidth of the system. In addition no damage due to the high field confined in the slits is risked with the Picometrix system, while damage to similar structures is often seen with the intense THz sources [127]. At the same time the transmission through the slit samples are down to a few percent, and for that reason the possibility of sampling many waveforms is crucial for a decent SNR in the recorded transmission spectra.

The first source considered for generation of THz pulses with energies in the μJ range was the $LiNbO_3$ crystal. At the beginning of this project a $LiNbO_3$ crystal was the source of the most intense pulses resulting in peak field strengths of ~ 400 kV/cm. With the aim of investigating nonlinear effects in crystalline materials such as coupling between phonons, it was found that only a few phonon resonances in various materials are within the limited bandwidth of the $LiNbO_3$. At the same time, considering the complicated geometry of the tilted pulse front method, a potential 2D THz spectroscopy experiment requiring two independent THz sources based on one or two $LiNbO_3$ crystals would be rather complex. The organic crystals of DAST and DSTMS offer THz spectra covering higher frequencies from 1-5 THz, and even with a significantly better conversion efficiency. Recalling the MD studies of sucrose from Chapter 2, this bandwidth is more ideal for covering several phonons. At the same time the collinear geometry significantly simplifies the experimental setup, which is much appreciated when assembling a 2D setup. While the high conversion efficiency of the organic crystals makes it up for energy loss when converting the 800 nm pulses to 1300 nm pulses with the OPA system, the biggest disadvantage is that the repetition rate should be on the order of 100 Hz to avoid heat buildup causing damage to the crystals. For this reason data acquisition time is increased as it is necessary to average over more scans or use longer time constants on the lock-in amplifiers in order to achieve the same SNR at 100 Hz than for a 1 kHz repetition rate system.

Even though the 2-color air plasma source with 1300 nm as the fundamental wavelength resulted in a high field strength when generating a single plasma, the 1 mJ output from the OPA system was not sufficient for generating two strong plasmas. At the same time the higher THz pulse energy in a more

limited bandwidth as generated from DAST and DSTMS was preferred for 2D spectroscopy.

Since the ABCD offers a lower sensitivity than EO sampling, and the nonlinear signal from organic materials such as sucrose are expected to be small, EO sampling was preferred since the generated frequency range could be covered with a GaP detector crystal. The spectra generated from DAST and DSTMS were recorded both with ABCD and EO sampling using GaP, and since no significant difference was observed in the spectral shape, the EO sampling was used for the 2D spectroscopy experiments where DAST and DSTMS were used as sources.

Table 1: Advantages and disadvantages of the THz sources discussed in this chapter.

THz source	Advantages	Disadvantages
Photoconductive antennas	• Fast waveform sampling • Can be portable	• Low pulse energies • Limited bandwidth
Lithium niobate	• High pulse energies • High damage threshold	• Complicated phase matching geometry • Transform-limited pulses of > 200 fs are optimum • Bandwidth is limited to 2-3 THz
2-color air plasma	• Relatively high pulse energies • Very high bandwidth • No phonons or crystal etalons • Tight focus	• Complicated, conical beam profile • Pulse energy is spread over the large bandwidth • Not very efficient at 800 nm
Long wavelength 2-color air plasma	• Efficiency increases with $\propto \lambda^{4.6}$	• OPA system is needed
DAST and DSTMS	• Very efficient, collinear phase-matching geometry • Bandwidth from 1-5 THz, high pulse energies confined here	• Low damage threshold • Should be pumped at ~1.3 μm (OPA system needed) • Low rep. rates i.e. ~100 Hz

Chapter 4

Beam profiling of THz beams

For spectroscopy systems it is important to characterize the spectral properties as well as the spatial properties of the beam. For beams with wavelengths in the visible and NIR part of the electromagnetic spectrum, the most common way to spatially characterize a beam is to scan a CCD or CMOS camera through the focal plane and measure the beam radius as function of distance to the focus. Spatial beam characterization of THz beams, however, is still not a standard procedure in most laboratories since no low-cost commercial camera is sensitive to THz light. Beam profiling of THz beams has instead been done by scanning single-pixel detectors in two or three dimensions [110, 112, 128-132], scanning a pinhole [109] or a disk [133], or using the knife-edge method [134], but these methods can be time consuming, difficult, or potentially inaccurate due to effects of diffraction at these wavelengths [133]. Recently, advances in detector arrays have led to the development of THz cameras [135], and today commercial THz cameras are available from several companies. These allow for fast and easy measurements of a THz beam, similar to conventional CCD based beam profile measurements at higher frequencies.

In this chapter beam profiling measurements are presented, where a commercial THz camera (NEC IRV-T0831) has been used to characterize beams from THz sources of DSTMS, $LiNbO_3$ and a two-color air plasma. The recorded images are 240x320 pixels with a pixel size of 23.5 μm, with 30 Hz frame rate, and the camera has a lock-in function chopping the incident laser beam at 15 Hz (half the frame rate) in order to reduce noise. The EO crystals DSTMS and $LiNbO_3$ generate Gaussian THz beams giving the possibility to characterize them according to well-known propagation formalisms and parameters such as *beam quality factor* M^2. This will be

discussed in section 4.1. THz radiation from two-color air plasmas is emitted in a conical pattern, and for this reason the beam profile characteristics are much more complicated than for the Gaussian beams. This is described thoroughly in section 4.2.

4.1. THz propagation from EO crystals

A way to characterize the quality of a Gaussian beam is to estimate the beam quality factor M^2. According to the ISO Standard 11146 the beam quality is calculated as

$$M^2 = \theta \frac{\pi w_0}{\lambda} \tag{4.1}$$

where λ is the wavelength, w_0 is the beam radius at the beam waist i.e. the beam diameter is the $1/e^2$ width (and not FWHM as usually preferred but $w \approx FWHM/1.18$ for a Gaussian beam) and θ is the half-angle beam divergence. The beam radius as a function of z is

$$w(z) = w_0 \sqrt{1 + \left(\frac{z}{z_R} \right)^2} \,. \tag{4.2}$$

Here z_R is the Rayleigh length. With this the beam divergence can be calculated as

$$\theta = \arctan\left(\frac{w(z)}{z} \right)\Bigg|_{z>>z_R} \,. \tag{4.3}$$

For Gaussian beams the M^2 factor is always equal to or greater than 1, and $M^2 = 1$ for a perfect, diffraction-limited beam. In the following, beam profiling measurements performed with the NEC THz camera will lead to an estimation of M^2 factors for the DSTMS and $LiNbO_3$ beams providing a measure of how close to diffraction-limited these beams are.

4.1.1. Beam profile from DSTMS

The experimental setup for THz generation with DSTMS is shown in Fig. 4.1 (a). As described in Chapter 3 the incoming beam consists of 70 fs pulses with energies of 1 mJ and a center wavelength of 1300 nm, which is generated by using the Spitfire Ace regenerative amplifier system together

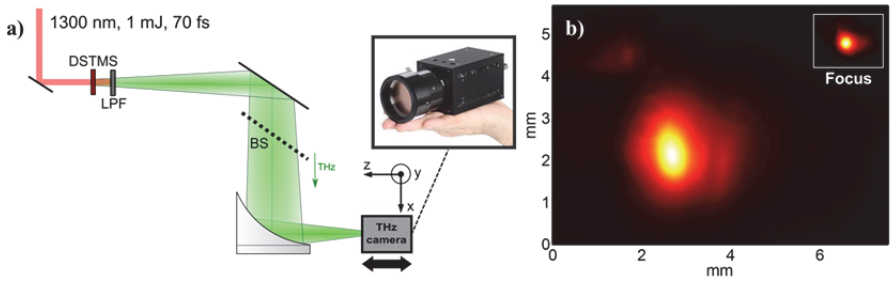

Fig. 4.1: a) Setup for THz generation with DSTMS. The 1300 nm is blocked by a low-pass filter (LPF) transmitting only frequencies < 20 THz. The THz beam is attenuated by a Si beam splitter (BS) and focused by a 2" off-axis parabolic mirror. b) Unfocused and focused intensity distributions measured with the THz camera.

with the TOPAS-prime OPA system. To prevent damage of the DTSMS crystal the repetition rate of the laser pulses is typically set to 100 Hz. The DSTMS crystal is aligned so that the *a*-axis is parallel to the polarization of the fs pulses (vertical). The optical light is blocked with a 20 THz low-pass filter from QMC instruments since 1300 nm is below the bandgap of Si, meaning that Si cannot be used to separate the THz beam from the laser beam. Prior to the implementation of the low-pass filter, sheets of Teflon and paper have also been used for the purpose of blocking the laser beam and transmitting the THz beam, but with a spectrally flat transmission of more than 90% the low-pass filter is preferred. Paper sheets are typically not transmitting frequencies higher than a few THz. The THz beam is slowly expanding after being generated in the DSTMS. The beam is focused by a single off-axis parabolic mirror with a focal length of 2", but since the beam is not completely collimated when it reaches the parabolic mirror the effective focal length was found to be approximately 2.5". To characterize the THz beam, the camera is scanned in the z-direction using a motorized stage. Both the parabolic mirror and the flat mirror directing the THz beam are mounted in kinematic mirror mounts in order to optimize the alignment of the THz beam. It has been found that even if the beam line is pre-aligned with a HeNe laser, the THz beam alignment might be significantly different. For alignment of the beam profile, the THz camera is used in video-rate i.e. 30 frames/s. Examples of THz beams where only alignment of the beam path with a HeNe laser has been performed are shown in Appendix B, where it is clearly seen that the alignment of the THz beam is not ideal. Well-aligned beam profiles of the DSTMS generated THz beam are shown in Fig. 4.1 (b)

where the inset is the focused beam, and the unfocused beam is measured approximately 16 mm from focus. Even though the repetition rate of the THz pulses was only 100 Hz, it was necessary to use two Si wafers for attenuation of the THz beam in order to avoid damaging the camera with the intense THz pulses. Due to Fresnel losses each Si wafer transmits approximately 50% of the incident THz power. One wafer was mounted on the front of the camera to protect the detection array from visible light, and the second wafer was positioned as indicated in Fig. 4.1(a) (BS) in the most expanded part of the THz beam. When using Si wafers for attenuation the round-trip reflection inside the Si wafer may appear in the recorded image as "ghosts". Two ghosts are seen in the Fig. 4.1 (b), one is from the Si beam splitter in the expanded beam path centered at approximately (x=1.8 mm,y=4.3 mm), and one from the Si wafer in front of the camera centered at (x=3.9mm,y=2.1mm).

Results from a beam scan of the DSTMS generated THz beam where camera has been scanned across the focal plane in steps of 1 mm are shown in Fig. 4.2. For each recorded image the projections of the intensity profiles in the vertical and horizontal directions are calculated, from which the FWHM is estimated. The FWHM at each stage position for both directions are shown in (a) as the red and blue dots, and the black curves are fits to the data according to the Gaussian beam propagation relation expressed in equation (4.2). With the Rayleigh lengths of (3.62 mm, 3.51 mm) and minimum FWHMs of (0.326 mm, 0.334 mm) for the (horizonzal, vertical) direction, it is seen that the fits agree well with the recorded data. The fact that the

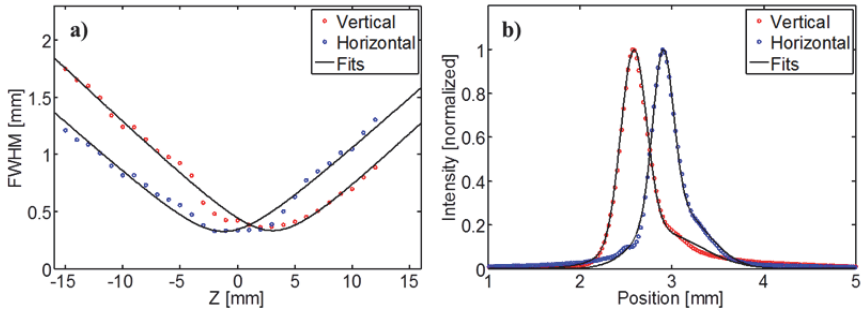

Fig. 4.2: a) FWHM measured for the DSTMS in horizontal and vertical direction. The solid black lines are fits of the FWHM of a Gaussian beam. b) Vertical and horizontal projection of the focused beam together with fits of two-peak Gaussian functions.

horizontal axis focuses a few mm before vertical axis is attributed to astigmatism. The horizontal and vertical projections of the intensity profile recorded at z = 1 mm are shown in Fig. 4.2(b). Here, each black curve is a superposition of two Gaussian functions in order to take both the beam itself and a ghost into account. The ghost next to the beam spot influences the horizontal projection in focus, while the ghost above the beam spot appears in the vertical projection.

The NEC THz camera is specified to be sensitive from 1-7 THz. However, the exact frequency response of the camera is not known. Nevertheless, this camera has been used for imaging of mid-IR fiber modes with frequencies higher than 25 THz [136], and stray light at 1300 nm is also picked up by the camera which proves that the camera is also sensitive to frequencies much higher than 7 THz. For evaluation of the beam quality this unknown frequency response is problematic since the M^2 factor should be calculated for a specific frequency. Considering the spectrum measured from the DSTMS source (shown in Chapter 3), the weighted average frequency is 2.2 THz, but the M^2 factor calculated from the DSTMS beam scan using this frequency is less than 1, which is not physically possible. Fig. 4.3 shows the

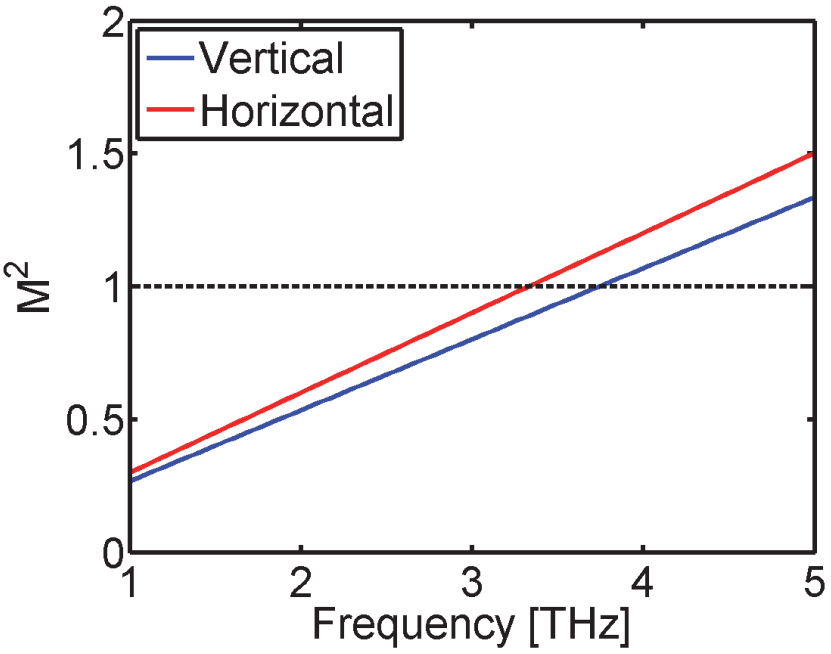

Fig. 4.3: M^2 values of the DSTMS beam in the vertical and horizontal direction within the bandwidth.

M^2-value calculated from the DSTMS beam scan when the frequency is varied over the measured bandwidth from 1 to 5 THz. Here, it is seen that only for frequencies higher than 3.8 THz the M^2 is greater than 1. This indicates that the beam profiles measured for DSTMS with the NEC THz camera is representative for the highest frequencies in the bandwidth i.e. around 5 THz. Still, at 5 THz the M^2 factor is estimated to be lower than 1.5 in both directions, meaning that the quality is comparable to the to the laser beam itself, since the M^2 factor is specified to be lower than 1.45 for the Spitfire Ace [56].

4.1.2. Beam profile from $LiNbO_3$

A similar beam characterization as described for DSTMS above has been performed for the $LiNbO_3$ THz source in the same experimental configuration as described in Chapter 3. For this beam scan it was not possible to measure the beam profile at distances longer than 2 mm from focus, possibly since most of the spectral bandwidth is below 1 THz where the camera is not specified to be sensitive. The stage was scanned in steps of 100 µm, and the results of this are shown in Fig. 4.4. The intensity profile in (a) is recorded a few centimeters from the crystal interface from where the THz beam is emitted, and the inset shows the beam focused by the pair of off-axis parabolic mirrors. The beam radii as measured at different stage positions are shown in (b) together with the corresponding fits. From these the M^2 values are estimated to 1.9 and 2.4 for horizontal and vertical direction, respectively, using $\nu = 1.4$ THz, which is the weighted mean

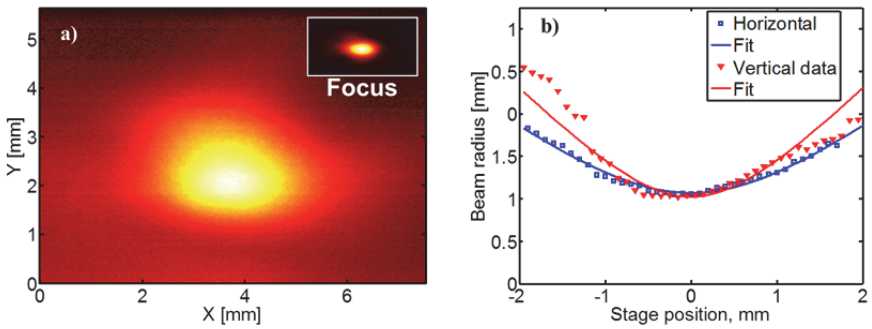

Fig. 4.4: a) THz intensity images of unfocused and focused THz beams generated in the $LiNbO_3$ crystal. b) Measured beam diameters when scanning through focus of the $LiNbO_3$ beam. The solid lines show fit to beam diameter of a Gaussian beam.

average frequency of the spectrum above 1 THz.

4.2. THz beam profile from a two-color air plasma

In this section it will be shown that the THz beam generated from a 2-color air plasma is spatially significantly different from a Gaussian beam. The intensity profiles of this beam are measured with the NEC THz camera in the same way as described above, but due to the non-Gaussian behavior the beam quality analysis used for the beams generated in EO crystals cannot be applied here. Instead a Bessel-Gauss model is proposed to understand the behavior of this beam through a focal plane.

The unknown frequency dependent sensitivity of the THz camera is even more critical when measuring a beam generated from a 2-color air plasma since the generated spectrum spans over more than 10 THz. For this reason a second technique based on measuring the Gouy phase shift is implemented in order to characterize the frequency dependent beam size in focus. The

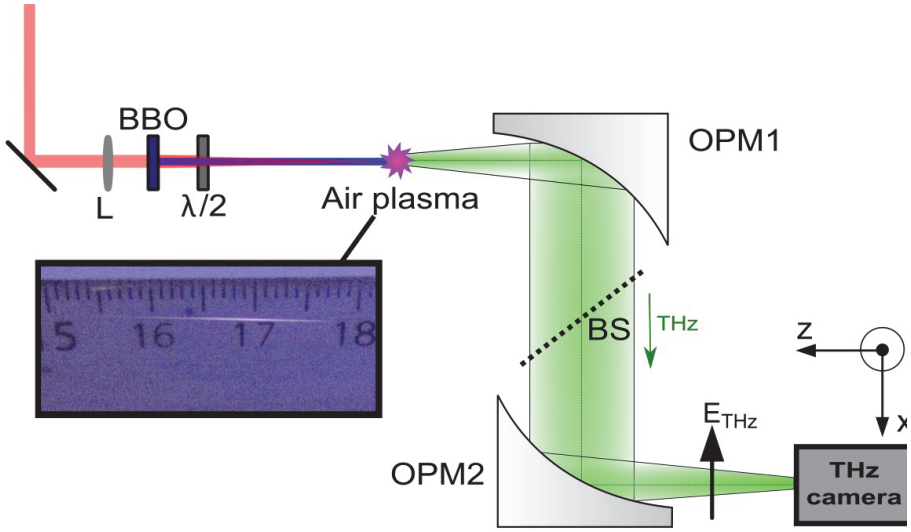

Fig. 4.5: Setup for THz generation in a two-color air plasma. By focusing both an 800 nm and its second harmonic with a 300 mm lens (L), a two-color plasma can be generated, which produces a terahertz pulse with a broad frequency range 0.2-12 THz (10% bandwidth). The inset shows a photo of the air plasma. The beam scan is performed by scanning the THz camera through the focus point on a translation stage. OPM1: 4" off-axis parabolic mirror, OPM2: 3" off-axis parabolic mirror, BS: Silicon beam splitter, BBO: β-barium borate.

Gouy phase shift is the additional phase shift experienced by an electromagnetic wave as it propagates through a focus, compared to the phase of a collimated beam over the same distance. In addition to this, beam profiles transmitted through THz bandpass filters are measured in order to study the frequency dependence of the focused as well as the unfocused THz beam. The beam profiling experiments presented in section 4.2.1 to 4.2.4 are performed with the Spitfire Pro XP in a configuration where the pulse duration is 100 fs. In section 4.2.5 a comparison of the beam profile emitted from two-color plasmas generated with 100 fs pulses versus 35 fs pulses will be presented with the overall conclusion that the two beam profiles are not significantly different. The final experiment presented in this chapter is the observation of a significantly weaker forward propagating mode in addition to the conical emission discussed in the previous sections.

The setup for THz generation with a two-color air plasma is shown in Fig. 4.5. The incident laser beam consists of 100 fs, 2.9 mJ pulses centered at 800 nm with a repetition rate of 1 kHz. The 800 nm pulses generate their second harmonic (400 nm) in a 100 μm thick β-barium borate (BBO) crystal, and both beams are focused collinearly using a biconvex lens with a 300 mm focal length. From this, an air plasma with a length of approximately 20 mm is generated. A photo of the air plasma is shown as the inset in Fig. 4.5. The THz light emitted from the plasma is collimated and focused by two off-axis parabolic mirrors, OPM1 and OPM2, with effective focal lengths of 4" and 3", respectively. A silicon beam splitter transmits the THz light but reflects the residual optical beams so that only the generated THz light is detected on the camera. The frequency range of the THz light generated with this setup spans from ~0.2 - 12 THz (10% bandwidth), as seen as the inset in Fig. 4.11 (b).

4.2.1. Beam scan through the focal plane

A beam scan is performed over a total scanning distance of 52.8 mm, and a THz radiation profile image is recorded for each step by integrating over 128 frames. Two examples of recorded intensity images are shown in Fig. 4.6. A representative image of the unfocused beam is shown in Fig. 4.6(a) whereas Fig. 4.6(b) shows a measurement of the focused beam. In the unfocused intensity profile a conical emission pattern is observed appearing as donut shaped beam profile, which is focused down to a single spot as seen in Fig. 4.6(b). A slightly uneven intensity distribution of the emission pattern through the whole beam scan is observed, which was also seen in [110] for

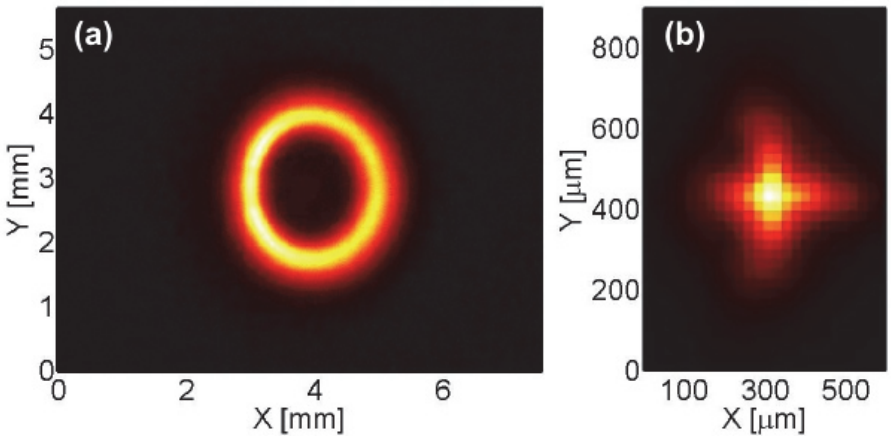

Fig. 4.6: (a) Intensity image recorded with the THz camera of an unfocused beam. (b) Intensity image recorded of the focused beam.

higher frequencies up to 10 THz. This is present in Fig. 4.6(a) as a slightly brighter emission pattern in the left half of the image. It has been discussed whether this can be avoided with spatial beam shaping of the incident fs pulses, but until now no experimental proof of this has been measured [137]. The THz beam is linearly polarized, both in the focal plane and in the unfocused parts of the beam, as determined by insertion of wiregrid polarizers. The full movie of the beam scan can be found at http://terahertz.dk/wp-content/beamscan_donut.mp4.

To investigate the evolution of the intensity distribution over the entire beam scan in a manner which is independent of the beam shape, the standard deviation ($\sigma_x = \sqrt{\int_x (x - < x >)^2 I(x) dx}$) is calculated for the X (horizontal) and Y (vertical) direction for each recorded image. The calculated standard deviations in the two directions are plotted as function of the camera stage position in Fig. 4.7. The intensity of the beam is distributed in a single spot when the stage position is close to the focus position and the standard deviation is minimal in both directions i.e. the stage position is between 25 mm and 32 mm. Again, it is seen that the standard deviation for the two directions X and Y do not minimize at the exact same stage position due to astigmatism in the imaging system. The minimum FWHM widths were measured to be 127.9 µm and 140.3 µm for the Y and X direction, respectively. It should be noted that only the region of the beam scan where

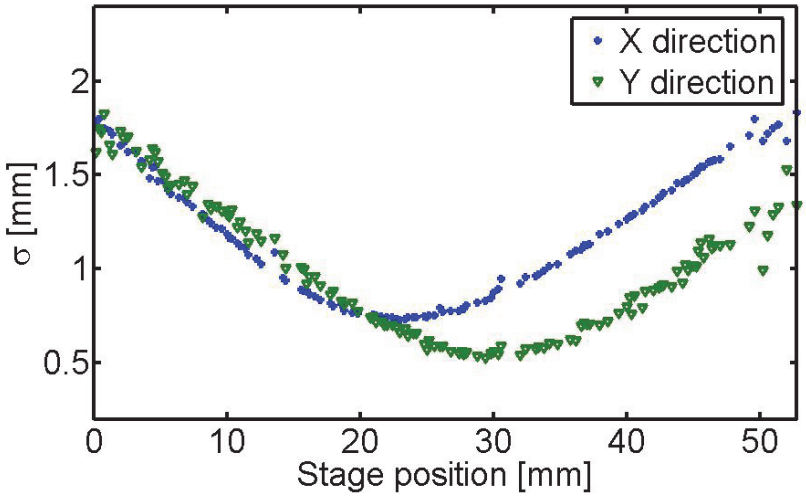

Fig. 4.7: Standard deviation calculated from the intensity profile measurements in the X- and Y direction.

the intensity pattern is a single spot is desired for nonlinear spectroscopy experiments.

The series of intensity profile images recorded with the THz camera can be combined into a 3D profile for full visualization of the beam properties. Fig. 4.8 show the measured 3D profile of the THz beam. The intensity profile is normalized at each z position in order to visualize also the weaker portions of the beam. At (http://terahertz.dk/wp-content/Rotation_donut.mpg) an animation where the beam is rotated around its focus point can be found, and Fig. 4.8 shows two screen shots illustrating the 3D beam shape. The extent of the focal region is clearly seen, indicating a very low divergence of the THz beam in this region. The rings in the outer regions of this 3D beam profile clearly show the conical shape of the beam in the far-field. The 3D visualization of the focused beam profile reveals several unusual features compared to a standard Gaussian beam that are worthy of a detailed discussion. The first unusual feature is the observation that the intensity profile is close to Lorentzian at the beam waist, and the second feature is the observation of the transition from the far field donut pattern to the spot-like profile in the focus region, with a prolonged, pencil-like focal region which is distinctly different from the focusing of a Gaussian beam. These features will be discussed in the following section. Additionally, a small off-axis pencil-like structure reminiscent of the focal

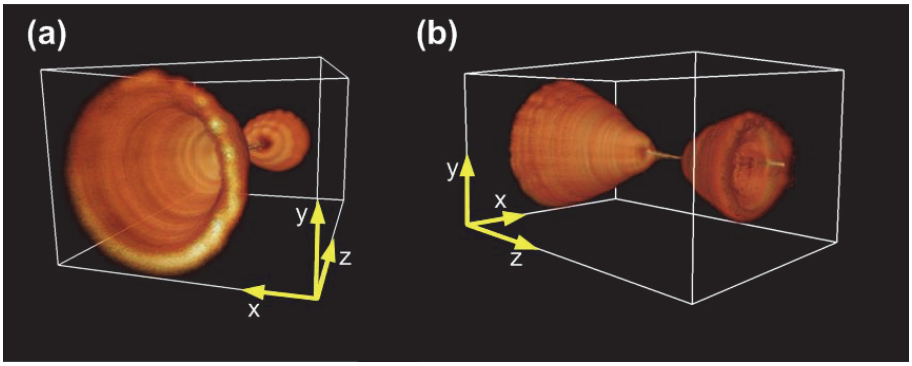

Fig. 4.8: (a) and (b) 3D reconstructed beam profile from camera measurements viewed from two different angles.

region at large z values (Fig. 4.8(b)) is observed. This feature is weak (approximately 5%) compared to the focused intensity, but is rendered visible due to the normalization procedure. This feature is due to a spurious reflection in the optical system, or possibly an on-axis forward propagating mod as discussed in section 4.2.6.

4.2.2. Modelling of a Bessel-Gauss beam

The anomalous behavior of the beam profile as it transforms from the far field to the beam waist and back suggests looking in the existing literature for solutions to the Helmholtz equation that mimic this behavior. Just such a solution, the Bessel-Gauss beam, was derived independently by both Sheppard and Wilson [138] and later Gori *et al.* [139]. The Bessel-Gauss (BG) beam is a linear superposition of traditional Hermite-Gaussian beams. While higher order solutions exist [140], only the fundamental mode of the ordinary BG beam is considered in the following. To conceptually describe a BG beam, a traditional Gaussian TEM_{00} mode propagating at a small angle, ε, from the *z*-axis is considered. If ε is large relative to the rate of beam waist expansion, *w(z)*, the Gaussian profile traverses away from the *z*-axis with increasing distance. The on-axis amplitude goes to zero except near $z = 0$, where the beam profile and the *z*-axis intersect. To construct the full BG beam, the TEM_{00} mode is swept a full period of 2π radians around the *z*-axis. This yields the full solution of [138-140]

$$U_{BG}(r,z) = A_0 \frac{q_0}{q(z)} \exp\left(\frac{ik}{2q(z)} (r^2 + r_c^2(z)) \right) J_0\left(\beta r - \frac{k r_c(z)}{q(z)} r \right) \qquad (4.4)$$
$$q(z) = q_0 + z; \quad r_c(z) = (\beta / k) z; \quad \varepsilon = \beta / k \quad .$$

where β is a length component orthogonal to the z-axis.

In particular, it is worth examining this solution at the beam waist. At $z = 0$, the profile is Gaussian with the addition of an interference term, a zeroth order Bessel function (J_0), which arises from the integration of the slight angular deviations from each independent Gaussian profile [141],

$$U_{BG}(r, z = 0) = A_0 \exp\left(\frac{-r^2}{w_0^2} \right) J_0(\beta r). \qquad (4.5)$$

To investigate how this beam compares with the experimental data, the transient photocurrent model is implemented as source of the THz field [142, 143]. The physical distribution of the induced plasma is approximated as a simple 1-dimensional line. In order to maximize the donut-like behavior of the photocurrent model, a plasma length of $2l_d \approx 40$ mm [110] was chosen, where l_d is the dephasing length. This results in a full 2π phase shift between the 400 nm and 800 nm beams for a realistic electron density of $10^{16}/\text{cm}^3$. In practice, the experimental plasma length is closer to 20 mm as seen in the inset in Fig. 4.5. However, the lengths of the plasmas in simulation and experiment are not directly comparable with each other. Changes in the incident laser intensity alter the plasma density, which will in turn alter the phase shift between the 400 nm and 800 nm beams along the filament, resulting in distinct changes to l_d and the emitted THz radiation profile. A more detailed treatment, and the resulting direct comparisons, could be achieved with a full 3D Finite Difference Time Domain (FDTD) simulation.

There are three small differences between [110] and the model implemented here. Firstly, the FWHM of the laser pulse was changed to 100 fs to better match our experimental conditions. Secondly, the Keldysh-Faisal-Reiss [144] equation for ionization is used instead of Ammosov-Delone-Krainov, and thirdly, the far field electric pattern in the time domain is calculated according to [145]

$$E(t,\vec{r}) \approx \frac{1}{4\pi\varepsilon_0 c^2} \int_{V'} d\vec{r}' \frac{[\dot{j}(t'_{ret},\vec{r}) \times (\vec{r} - \vec{r}')] \times (\vec{r} - \vec{r}')}{|\vec{r} - \vec{r}'|^3}, \qquad (4.6)$$

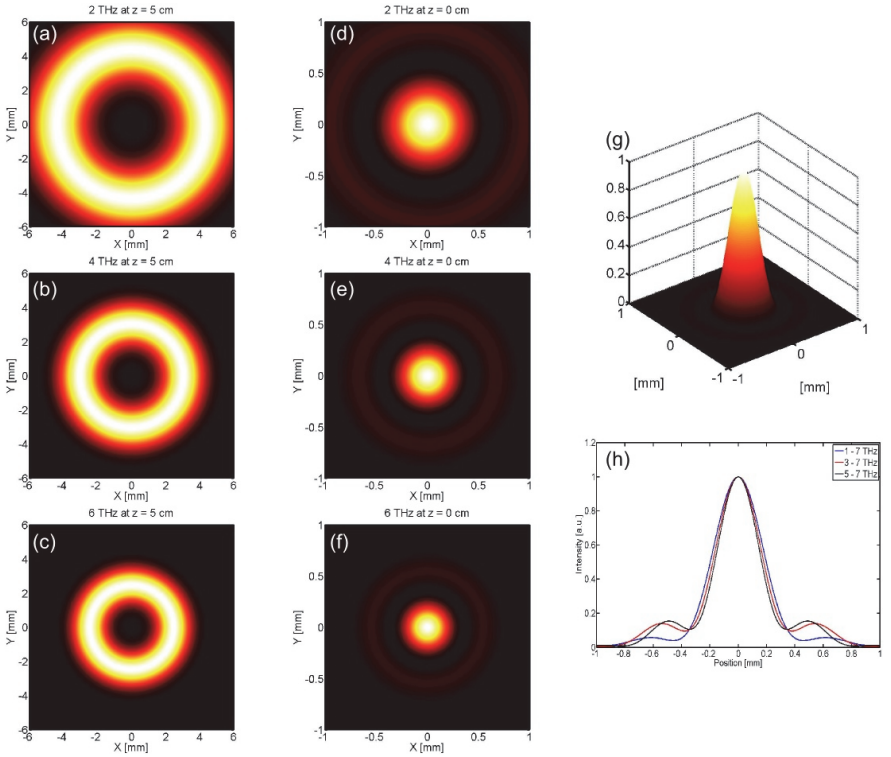

Fig. 4.9: The left column is the BG far field profile at z = 5 cm from top to bottom for (a) 2 THz, (b) 4 THz, and (c) 6 THz, respectively. The central column is the profile at z = 0 for the same frequency components (d-f). (g) is the broadband (1 – 7 THz) summation of the profiles where the external rings in (d-f) interfere destructively to generate a smooth, Gaussian spot. This is further demonstrated in (h) where the projections of the different bandwidths are shown.

where

$$\dot{j}(t'_{ret},\vec{r}) \equiv \left(\frac{\partial j}{\partial t}\right)_{t=t_{ret}} \tag{4.7}$$

is the derivative of the current evaluated at the retarded time. Using this model, the electric field is calculated in two far field planes, at z_1 = 0.5 m and z_2 = 0.75 m.

The solution at these two planes is used to analyze the beam profiles calculated from the transient photocurrent model as a BG beam. The two far field profiles are Fourier transformed in the time domain to obtain single

frequency profiles. The angle ε was determined from a simple geometric calculation i.e. $\varepsilon = \arctan((x_2 - x_1)/(z_2 - z_1))$, where x_2 and x_1 are the physical locations of the maximum value of the donut shaped profile. In this way, the only free parameter remaining is q_0.

Once the BG beam parameters are known, it is possible to propagate the beam parameters through optical systems according the ABCD matrix formalism [140, 146] (not to be confused with the ABCD – Air Biased Coherent Detection abbreviation mentioned previously) in order to take the focusing by OPM1 and OPM2 in Fig. 4.5 into account.

In Fig. 4.9 three single frequency slices that result from this full treatment are shown. It is clearly seen in (a)-(c) that the beam profiles have the experimentally measured conical profile in the far field, and collapse to a spot-like profile at the beam waist as seen in (d)-(f). However, the beam waist profiles shown in (d)-(f) also display an extra ring, resulting from the Bessel function in Eq. (4.5), which is not observed in the experiment. However, the experimental beam measurements themselves are broadband in nature, and that the extra ring radius in the BG beam is frequency dependent. When the broadband beam waist profile is reconstructed, using the full bandwidth of the model, it is seen that rings of different frequency interfere destructively with each other and gradually disappear with increasing bandwidth, resulting in the smooth, single spot shown in Fig. 4.9(g). To demonstrate the effect of added frequency components on the spot size, the horizontal projections of the beam spot with different bandwidth contributions are shown in Fig. 4.9(h). As the bandwidth increases, the wings of the projection are clearly diminished.

In the same manner as for the experimentally measured beam profile in the previous section, a broadband (1-7 THz) 3D beam profile is reconstructed in Fig. 4.10. In comparison to the measured 3D beam profile in Fig. 4.8, the same overall behavior of the simulated beam profile is observed. In both cases the donut shaped beam is focused down to a narrow single-spot intensity profile with a low divergence around the focal region. It is worth noting that the focal region is not as narrow and extended as it appears. The intensity profile of each z slice is independently normalized so that the far field donut behavior can be seen in the same plot as the focus. This makes the focal region appear highly localized over an extended range.

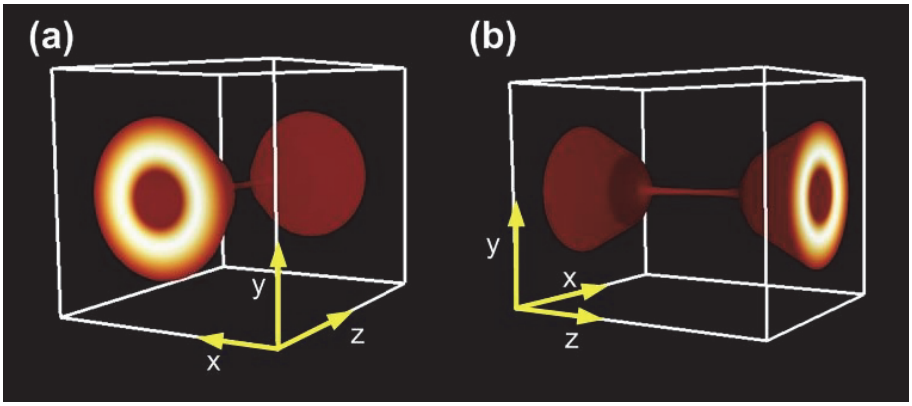

Fig. 4.10: (a) and (b) 3D reconstructed beam profile from simulated intensity profiles viewed from two different angles.

While the combined model of the transient photocurrent and BG beams qualitatively recreates the experimental data, there is an outstanding disagreement concerning the shape and size of the beam waist profile. As seen in the following section a Lorentzian profile is observed at the beam waist. The modelling here predicts a Gaussian profile, as seen in Fig. 4.9 (h). Furthermore, the FWHM from this model is approximately twice of that observed in the experiment. It is possible that the discrepancy lays in the physical length of the generated plasma chosen for the photocurrent model. Here the chosen length was $2l_d$ in order to maximize the donut like behavior and minimize the radiation in the forward direction. In practice, the experimental plasma length is expected to be different from this value, which should result in a combination of donut like emission as well as a radiation component in the forward direction, which is observed in a separate experiment as shown in section 4.2.6. Furthermore, the physical width of the plasma filament has also been neglected in this one-dimensional model. This may also explain the discrepancy through interference from different physical locations in the plasma.

4.2.3. Beam waist profile by Gouy phase shift measurements

For most THz applications, and especially for nonlinear spectroscopy, Gaussian-shaped beam profiles are desired in order to achieve localized, well-controlled high electric field values. However, Gaussian beam shape is not observed for the measurements in the focal plane. Instead much better fit is achieved using a Lorentzian profile (see the intensity image in Fig. 4.6(b) and its horizontal projection in Fig. 4.12(a)). For this reason a second

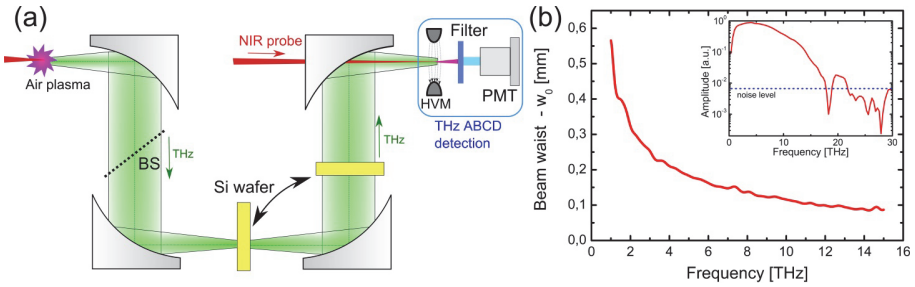

Fig. 4.11: Experimental setup for determination of the Gouy phase shift. THz transients are generated using two-color laser induced plasma and detected using the ABCD method. (b) The frequency resolved THz beam waist calculated using Gouy phase shift measurement. Inset: a typical spectrum measured by the ABCD.

experiment is performed in order to investigate the beam waist at the focal plane.

When focusing a beam as in the experiment, the wave experiences an additional phase shift – the so-called Gouy phase shift [147-149]. Kuzel *et al.* [150] defined how the Gouy phase shift affects the measurement of the refractive index of a sample placed in the focus of the THz beam compared to a sample placed in the collimated beam. By comparing those two extracted refractive indices for the same sample, the Gouy phase shift can be determined. Assuming a Gaussian beam in the focal plane of the beam, the procedure described by Kuzel et al. was applied to extract information about the beam waist size over the entire experimental frequency range. The setup used for the Gouy phase experiment is shown in Fig. 4.11(a). The THz beam is generated and focused in the same way as described previously, and now the THz spectrum is detected using ABCD technique. A typical spectrum measured with this setup without a sample is shown in the inset of Fig. 4.11(b). The Gouy phase shift is extracted by measuring the difference in apparent refractive index of a 525-µm thick high resistivity silicon wafer at two distinct positions, namely in the focal plane of the THz beam, and in the collimated part of the beam, as indicated in Fig. 4.11(a). Using these scans, the experimental beam waist for all frequencies is extracted as shown in Fig. 4.11(b). Assuming that the intensity profile at the beam waist is a superposition of frequency dependent Gaussian beams with width and with amplitudes weighted according to the spectrum in Fig. 4.11(b), the intensity profile displayed in Fig. 4.12(b) is obtained. Comparing this intensity profile derived from the Gouy phase shift with the experimental measurements it is

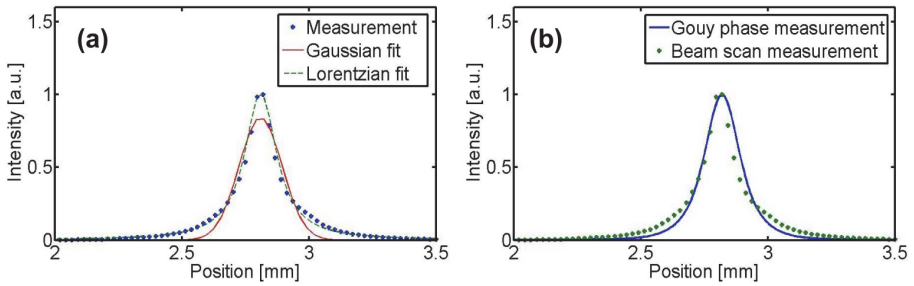

Fig. 4.12: (a) Beam profile measurement of focus together with Gaussian and Lorentzian fits. (b) Beam profile measurement together with the measurement based on the Gouy phase shift in the THz beam focus. All data points are the projection of the recorded image onto the X direction. All profiles shown are projections onto the X axis. The Y projections are similar to the X projections, and are therefore not shown.

seen that both profiles have Lorentzian shapes, and are in good agreement with each other. The low intensity part of the profile measured with the THz camera is slightly broader than the profile extracted from the Gouy phase measurement. However, this discrepancy could easily be due to additional broadening from the response function of the camera.

4.2.4. Frequency resolved beam profiling

Simultaneously with the beam profiling study presented above, THz bandpass filters made of metamaterial composites were designed and fabricated by Andrew Strikwerda, Maksim Zalkovskij and co-workers [151] based on the trapped mode excitation concept [152]. These filters have been provided for a frequency dependent beam profiling study, where beam profiles of the frequencies transmitted through the filters have been recorded. The spectral characteristics of the filters are described in Table 2. The intensity images of the unfocused THz beam are shown in Fig. 4.13 where

Table 2: Characteristics of THz bandpass filters.

Filter no.	*1*	*2*	*3*	*4*	*5*	*6*
Central frequency, THz	2.5	3.3	4.0	4.9	6.3	8.5
FWHM, THz	1.6	2.0	2.5	3.2	4.1	5.8

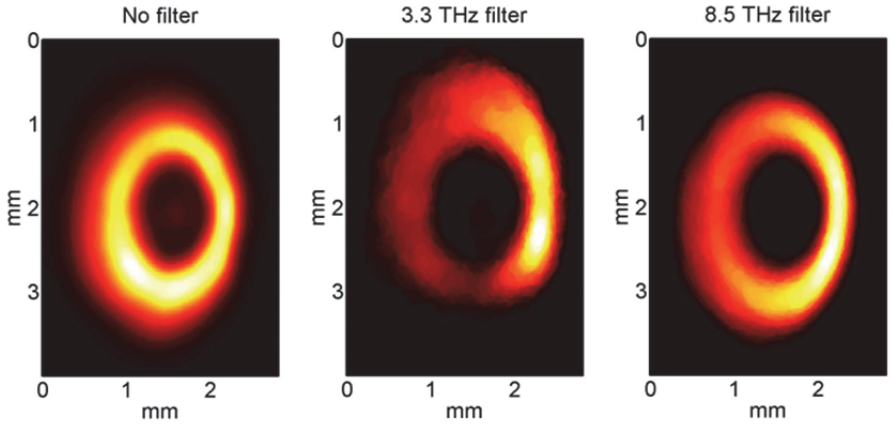

Fig. 4.13: Intensity images of the unfocused THz beam measured approximately 7 mm from the central focus position. The left panel shows the profile measured without any band-pass filter, where the center and the right panel are measured with bandpass filters with center frequencies of 3.3 THz and 8.5 THz, respectively.

the left panel is the profile recorded without bandpass filters and the central and the right panels are with the profiles measured with bandpass filters with central frequencies of 3.3 and 8.5 THz. Since the transmission through the filters is rather low and in most cases not possible to see at video-rate on the camera, each image shown in Fig. 4.13 is a sum over approximately 1000 recorded images, where each image is averaged over 128 frames. In general, the spatial shapes of the three profiles in Fig. 4.13 are relatively similar, and display a conical emission pattern in agreement with the profile presented in section 4.2.1. The slightly deformed shape of the profile recorded for the

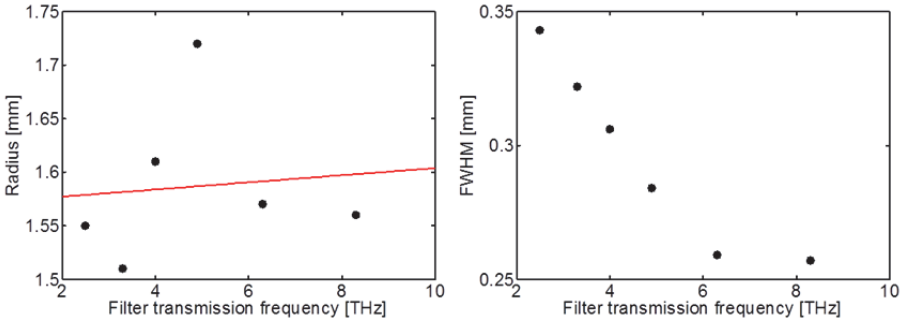

Fig. 4.14 Left: Outer radius of the unfocused beam 6 mm the from focus measured for each filter. Right: FWHM of the focus in the horizontal direction for each bandpass filter.

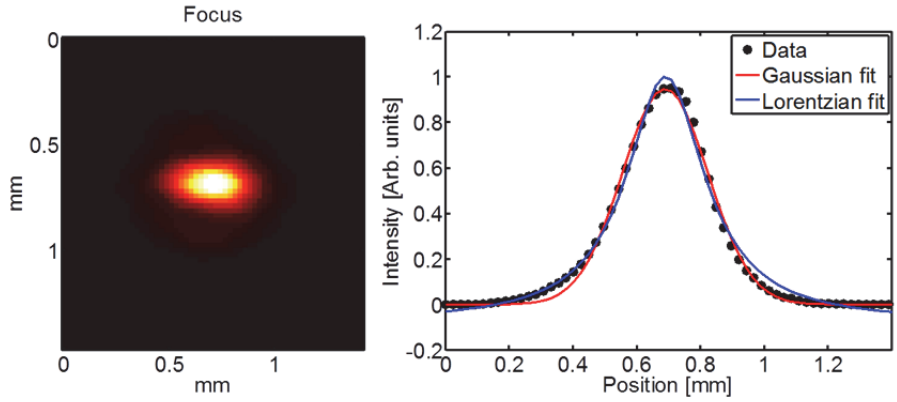

Fig. 4.15: Left: focus measured with the bandpass filter with central frequency of 4.0 THz. Right: horizontal projection together with Gaussian fit (red curve) and Lorentzian fit (blue curve)

3.3 THz filter is expected to be due to the low transmission of this filter giving a lower SNR. It is observed that the filters sharpen up the edges of beam profile as could be expected due to the low transmission bandwidth. The radius of the three profiles appears to be the same, which is in contradiction with what was predicted in section 4.2.2, where the divergence of the THz radiation emitted from the plasma is predicted to be frequency dependent for a BG beam. For this reason the outer radii of the conical emission patterns are measured 6 mm from the focus point for each filter, as shown in Fig. 4.14, together with the best linear fit shown as the red solid line. Again, no clear frequency dependence is seen and the radius appears constant with frequency. The right panel of Fig. 4.14 show the frequency resolved investigation of the beam profile in the focal plane. A rapid decrease of the size of the focus when the central frequency increases is observed, which is generally what is expected. The FWHM of the last data point recorded in focus when using the bandpass filter with a center wavelength of 8.5 THz is not significantly smaller than when the 6.3 THz filter is used. However, the FWHM of the 8.5 THz filter is 5.8 THz meaning that it is so broadband that is also covers 6.3 THz, and it is thereby reasonable that these two measurements gives a similar focus size. The left panel in Fig. 4.15 shows the profile at 4.0 THz, and the right panel shows the horizontal projection together with a Gaussian and Lorentzian fits seen as the red and blue curves, respectively. It is seen that the recorded data is no longer appearing more Lorentzian than Gaussian, which indicates that the

Lorentzian profile measured in the previous experiment may have this shape due to the broadband nature of the beam.

4.2.5. Long pulse versus short pulse 2-color air plasma

When generating the air plasma with shorter pulses, the bandwidth of the generated THz beam increases. The THz spectrum spans up to more than 20 THz when using 35 fs pulses, whereas the spectrum generated with 100 fs pulses was covering up to 12 THz. In the following the spatial differences between the THz beam profile when using long and short fs generation pulses are discussed.

A beam scan was performed through the focal plane over a distance of approximately 20 mm where the Spitfire Pro XP was configured to deliver 35 fs pulses instead of 100 fs as for the measurements presented above. All other experimental settings were similar as previously explained. In the following discussion this measurement series is referred to as the "short pulse measurement", and the measurements performed with 100 fs pulses is referred to as the "long pulse measurement".

Two intensity images recorded approximately 7 mm from the focus position are shown in Fig. 4.16. Due to astigmatism the X direction and the Y direction of the THz beam focuses at slightly different stage positions, so the stage position at the focus position, $z = 0$, is defined as the mean focus position for both axes. Fig. 4.16 (a) is recorded for the long pulse generated THz beam, where (b) is for the short pulse generated beam.

Both intensity images show the donut-shaped conical emission pattern, which is expected when the generated THz beam is not focused. To quantify

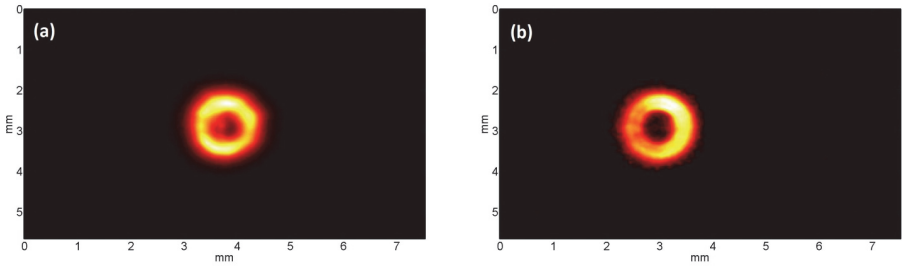

Fig. 4.16: Intensity images recorded approximately 7 mm from focus for a THz beam generated with (a) 100 fs pulses and (b) 35 fs pulses.

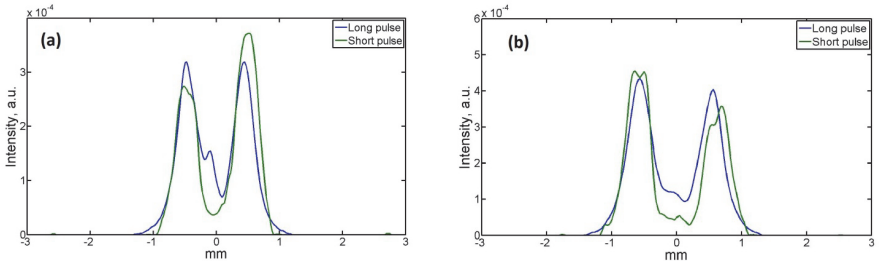

Fig. 4.17: Cross-sections through the center of the intensity profiles of THz beams generated with long and short fs pulses shown in Figure 2. (a) shows cross-sections in the X direction and (b) shows cross-sections in the Y direction.

the difference between the two measured profiles, the cross-sections through the center of the two profiles in Fig. 4.16, are plotted for the X and the Y direction in Fig. 4.17 (a) and (b), respectively. For the conical emission pattern, each cross-section has two main peaks, where the full-width-at-half-maximum (FWHM) is measured for all peaks. All measures are provided in Table 3. On average the FWHM of the peak of the short pulse beam profile is 0.425 mm, which is slightly larger than the FWHM of the peak of the long pulse beam profile which is 0.413 mm. In other words this means that the donut generated with short pulses is thicker than with long pulses, which is expected since the spectrum is broader. However, considering the large standard deviations, the difference is not significant.

For all measurements of the unfocused beam profile having the conical emission pattern, the radius of the distributions in the X and the Y direction are measured as half the distance between the two peaks in the cross-sections. The radii at each stage position in the X and the Y direction for the

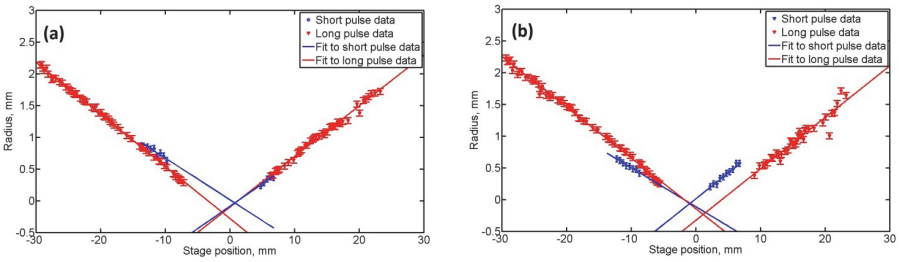

Fig. 4.18: Radius measured at different stage position for THz beams generated with long and short fs pulses in (a) the X direction and (b) in the Y direction.

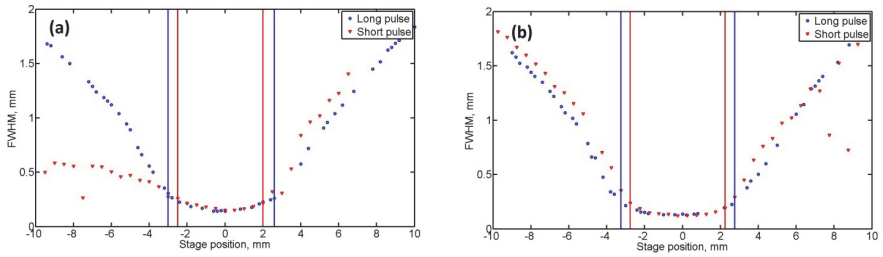

Fig. 4.19: FWHM measured at different stage positions for THz beams generated with long and short fs pulses in (a) the X direction and (b) in the Y direction.

two experiments are shown in Fig. 4.17 (a) and (b), respectively. The central region around z = 0 is the region where the beam profile collapses to a central spot, which will be discussed further below. The solid lines are linear fits to the corresponding data sets. The slopes of the fits define the divergence angles as shown in Table 3. On average the divergence angle is 4.61^{o} for the long pulse beam scan, which is slightly higher than for the short pulse profile where it was measured to be 4.05^{o}. This in agreement with the observations in [110] where the higher frequencies diverge less.

To characterize the width of the intensity distributions and the length of the focus region where the beam is a single spot instead of a donut, the FWHM of the cross-sections at each stage position are plotted for the X and Y direction in Fig. 4.19. Because of the uneven intensity distribution of the conical pattern, which is for example seen as the higher intensity in the right side of the image in Fig. 4.16 (b), the short pulse data points (shown as red symbols) at negative z values outside the focus region appears smaller than the actual FWHM values are expected to be. The focal regions are in between the solid red and blue lines for the short and the long pulse measurements, respectively. It is seen that the long pulses give a focus region 1 mm longer than for the short pulses in both the X and Y direction. The FWHM values at the beam waist are shown in Table 3. Beam parameters.It is seen that they span from 0.119 mm to 0.149 mm with no specific trend. It is important to note that the divergence in the focal region is much lower than for the conical beam outside the focal region, which was characterized in section 4.2.2 as the propagation of a BG beam.

Table 3. Beam parameters.

Parameter	Long pulse, X	Long pulse, Y	Short pulse, X	Short pulse, Y
FWHM, left peak	0.449 mm	0.404 mm	0.430 mm	0.402 mm
FWHM, right peak	0.421 mm	0.381 mm	0.454 mm	0.414 mm
FWHM, average	0.413 mm ± 0.029 mm		0.425 mm ± 0.023 mm	
Divergence angle, left	4.69^{o}	4.57^{o}	3.77^{o}	3.50^{o}
Divergence angle, right	4.64^{o}	4.61^{o}	4.05^{o}	4.90^{o}
Divergence angle, average	$4.61^{o} \pm 0.06^{o}$		$4.05^{o} \pm 0.61^{o}$	
Focus FWHM	0.140 mm	0.129 mm	0.149 mm	0.119 mm

In general, the spatial characteristics of the width of the conical emission pattern, the divergence angle, the FWHM in focus and the length of the focal region are not significantly different when generating the air plasma from 100 fs pulses rather than 35 fs pulses. Most important is that for long pulses, the conical beam diverges more and has a longer focus region.

4.2.6. On-axis propagating beam

In addition to the conical emission pattern originating from the phase matching of the different frequencies involved in the generation process along the finite length of the plasma, a small but detectable amount of radiation should be generated and emitted in the forward direction from the last section of the plasma filament, independent of phase matching conditions. To measure the forward propagating mode, an open pinhole is implemented in the beam path where the conical THz emission is collimated, indicated as P in Fig. 4.20. The pinhole has a 10 mm aperture so that the conical THz emission is eliminated from the beam path and only the forward propagating mode propagates to the THz camera. The THz camera is

scanned in the z-direction over a distance of 7 mm in steps of 0.5 mm. Due to the weak intensity of the forward propagating mode, it was necessary to record approximately 100 images (using the lock-in function), each averaged over 128 frames, that were added up to an intensity image as shown in Fig. 4.21(a). Before the summation of the images, a 2-dimensional median filter was applied to each of the images to remove the "salt and pepper" noise but maintain the THz signal, which typically appeared as a few clustered illuminated pixels in a single image. Due to the low intensity of the forward propagating mode, it was not visible in a single recorded frame.

To investigate the spatial shape of the intensity image shown in Fig. 4.21(a), the horizontal and vertical projections are calculated. The horizontal projection is shown in Fig. 4.21(b) as black dots together with a Gaussian fit shown as a red curve. It is seen that the data points fit well with the Gaussian curve. The vertical projection has similar properties as the horizontal and is for this reason not shown.

To estimate the FWHM of the spot size, the horizontal and vertical projections were calculated for the intensity profiles measured at each camera position. Over the length of 7 mm that the camera was scanned no significant focusing of the forward propagating mode was observed.

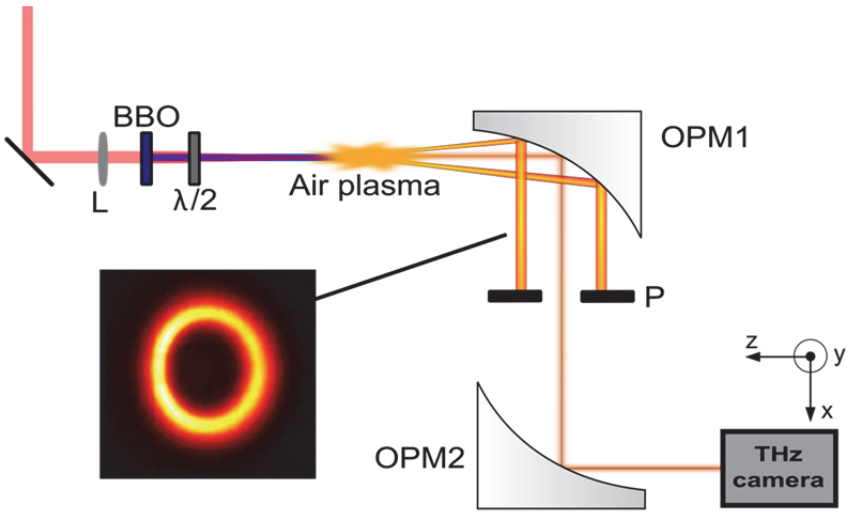

Fig. 4.20: Experimental setup where a 10 mm aperture is inserted at the point P to block the conical emission but allow the on axis emission to propagate to the camera.

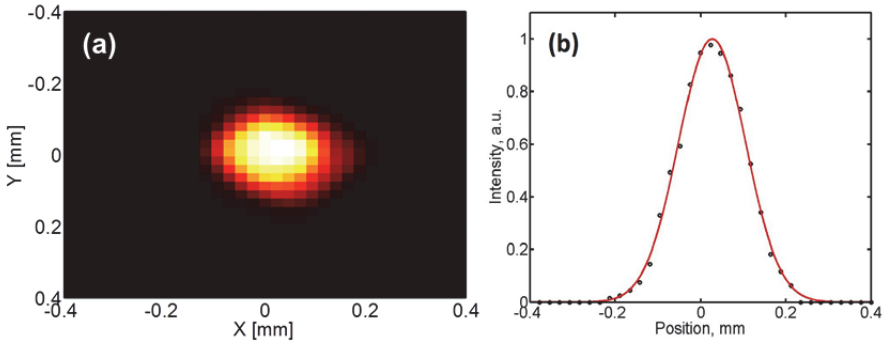

Fig. 4.21: (a) Intensity image of the forward propagating mode. (b) x-projection of the forward propagating mode. The black circles are experimental data, red curve is a Gaussian fit to the experimental data.

However, in contrast to the focused conical emission, this mode could be fitted well with Gaussian fits where the fit errors on the FWHM was less than 4.2 µm. Based on statistics for all images recorded over the 7 mm distance, the FWHMs in the vertical and horizontal directions were measured to be 174 µm ± 54 µm and 193 µm ± 65 µm, respectively. The high standard deviations are attributed to the low intensity of each recorded intensity image. The observation of collimated propagation of the forward propagating mode after OPM2 is indicative of a low divergence of the forward propagating mode emitted from the plasma, compared to the off-axis conical emission. The low-diverging forward propagating mode transmitted through the imaging optics OPM1+OPM2 would result in a tight, collimated beam after OPM2.

4.3. Conclusion

In this chapter spatial characteristics of two types of beams have been presented: beams generated from EO crystals and from a 2-color air plasma. The EO crystals DSTMS and $LiNbO_3$ both generated Gaussian beams, where the DSTMS beam achieved the highest beam quality with an M^2 value below 1.5. This is possibly because the DSTMS, in contrast to $LiNbO_3$, has a collinear phase matching geometry, and experimental setup is much simpler than for $LiNbO_3$ (ignoring that an OPA system was needed for pumping DSTMS).

It has been verified that the beam profile emitted from a two-color air plasma is conical, and collapses into a single spot when it is focused tightly. This is crucial for experiments such as THz imaging or spectroscopy, especially in case several beams need to be spatially overlapped as for example in a pump-probe or 2D spectroscopy experiment. The conical intensity profile, which collapsed into a single spot in the focus region, was modelled successfully as a Bessel-Gauss beam, with the most important difference that the measured beam profile in focus had a Lorentzian shape. In an additional experiment where the beam size was extracted from the Gouy phase shift, the results showed that the Lorentzian profile emerges when superposing beam profiles for all frequencies in the bandwidth into a broadband profile. Oppositely, measuring the focused beam profile in more narrow bandwidths using THz bandpass filters the shape showed beam profiles that appeared more Gaussian than Lorentzian. Also, the size of the beam waist decreased as expected when bandpass filters with higher center frequencies were used, but the unfocused beam did not indicate any clear frequency dependent tendency. However, a more thorough frequency dependent study of the unfocused beam is essential in order for this to be conclusive.

Chapter 5

Field enhancement in micro-slits

The previous chapters have discussed how to achieve the highest possible field strengths at THz frequencies in free-space setups. Complimentary to this, it is here proposed how plasmonic structures can be used to enhance a THz field yielding field strengths of tens of MV/cm.

Recently, nanoslits were proposed for THz spectroscopy studies of crystalline materials since the electric field as well as the absorption cross-section can be enhanced dramatically inside the slit [19]. Similarly, the properties of phonon modes in extremely small volumes of semiconductor quantum dots have been studied with the dots placed in a nanogap between closely spaced metallic antennas with strong, resonant field enhancement of the incoming THz field [153], and linear vibrational spectroscopy of monolayers of proteins in the field enhanced region near nano-antennas have been studied in the mid-infrared [154]. In both cases, a strong coupling between the vibrational modes of the sample and the resonance of the antenna was observed.

The field enhancement inside metallic apertures such as nano-holes [155] and slits [156] have been studied extensively with emphasis on the extraordinary transmission of light through such structures. At the same time it has been shown that lattice modes from a periodic array structure can couple to the resonance of the structures itself [157, 158]. While the nature of the coupling between apertures arranged in a periodic array in a metallic film has been established to be of plasmonic nature [159], comparable little information and design criteria on how to exploit this coupling for additional field enhancement inside the apertures is available in the literature. Yet, tailoring of this coupling to achieve the highest possible field enhancement

for spectroscopy systems in the THz range is important. On the other hand, uncontrolled coupling to lattice modes can distort the spectrum enhanced with a metallic structure, from which spectral effects in a potential spectroscopy experiment would be very complicated to relate to the absolute field value. Fig. 5.1 shows an example of this where an 250x250 μm array of slits have been designed to be resonant at 5 THz, and the field enhancement measured in a 2-color air plasma setup with ABCD are shown as the blue data points. The green line shows a Gaussian fit as which the resonance of the slit itself is roughly expected to behave. However, it is seen that the measured resonance does not have a smooth response like the Gaussian fit, but including all possible lattice modes for this structure on the interface between the gold layer and silicon substrate (purple bars calculated as in Eq. (5.2)), it is clearly seen that slit resonance is affected by coupling to certain modes.

Due to the high conductivity of metals in the THz range, the existence of SPPs in the THz range has been disputed, but it seems clear that coupling of the electromagnetic field to metal surfaces is a well-established fact [160], with demonstration of plasmonic localization of THz waves in parallel plate

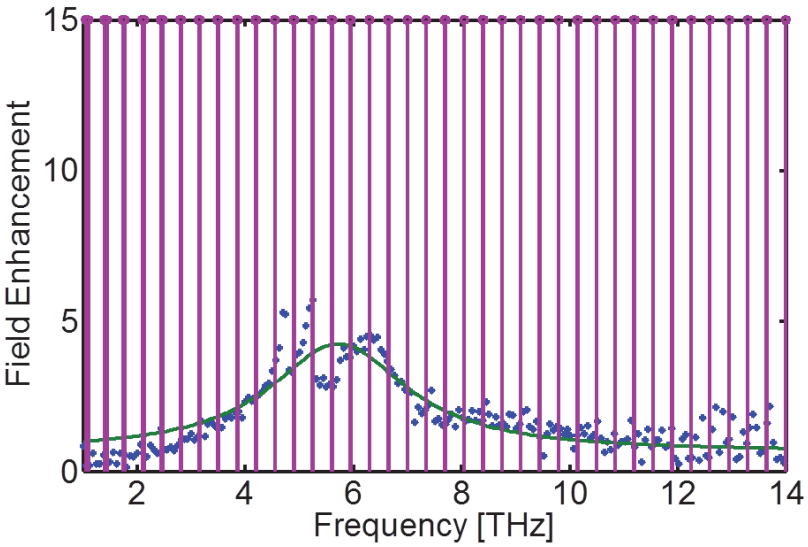

Fig. 5.1: Field enhancement measured through slits designed to be resonant at 5 THz in a 250x250 μm slit array (blue points) and Gaussian fit (green curve). Purple bars are all possible lattice modes on the silicon interface as calculated from Eq. 5.2.

waveguides (PPWGs) [161], in tapered PPWGs [162], on tapered wires [163], and along curved, featureless metallic surfaces [164].

In relation to the above mentioned field enhancing structures, apertures are preferred for this study since the detected THz fields must propagate through the field enhancing regions, which is not necessarily the case for antennas on a substrate. In the following it is demonstrated how rectangular slit apertures with transmission resonance frequency in the low THz range, arranged periodically in a metallic film, can be designed so that the lattice modes constructively interfere with the slit resonance. The coupling can lead to a field enhancement which is up to 60% larger than in the case of an isolated slit of the same dimensions. With apertures fabricated by standard UV photolithography the achieved field enhancement is up to 40 times compared to the incoming field while maintaining an overall transmission through the array of up to 10%, thus enabling sensitive detection of the transmitted field. The additional enhancement is due to a strong coupling mediated by standing surface plasmon polariton (SPP) waves between the resonant electric field in the microslit resonators and the lattice modes existing in the array of slits. The presented experiments and simulations clearly demonstrate that the coupling has all signatures of a plasmonic nature, and thus contributing to the understanding of plasmonic couplings in the THz range.

5.1. Theoretical resonance calculations

The resonant length of a half-wavelength dipole antenna is defined as the length where the reactance (imaginary part of the impedance $Z_{in} = R_{in} + iX_{in}$) is zero. This is when the length is slightly shorter than $\lambda_0/2$, where $\lambda_0 = c/\nu_0$ is the resonance wavelength in free space, and ν_0 is the corresponding frequency [165]. The resonant properties of a narrow slot antenna formed by a rectangular hole in a metallic layer are similar to those of a dipole antenna on a substrate, with correspondence between the electric and magnetic fields in the two complementary situations defined by Babinet's principle. The redshift of the resonant transmission wavelength through rectangular apertures has been observed both in simulation assuming that the metal is a perfect electric conductor [166] and in experiments at near-infrared and visible wavelengths [167] where the conductivity of metals (silver in that case) is significantly smaller than in the THz range. The finite conductivity of the metal gives a significant penetration of the field into the

metal on the order of 80 nm at 1 THz for gold, leading to a larger effective aperture, and thus further redshift of the transmission maximum [168]. The transmission through the aperture is enhanced at its resonance frequency for electric fields polarized perpendicular to the long axis of the aperture due to buildup of polarization charges along the slit walls. At resonance, the currents at the end points of the slit aperture vanish, resulting in charge accumulation at each side of the aperture and consequently strong field enhancement and enhanced transmission. When a slot antenna is placed on a semi-infinite substrate, the optimal length L for a given width w, and resonance frequency ν_0 of the antenna is given the same expression as for a thin wire antenna, modified by a factor determined by the permittivity of the substrate [165, 169],

$$L \approx \frac{0.48c}{\nu_0 \sqrt{\varepsilon_e}} \frac{1}{1 + w/L}, \tag{5.1}$$

where c is the speed of light in vacuum, and the effective permittivity is defined as $\varepsilon_e = (1+n^2)/2$ in the limit of a half-infinite substrate, and n is the refractive index of the substrate material. In the case of silicon, $n = 3.4177$ [71]. Park *et al.* [170] have shown this approximation to be valid for SiN substrates thicker than 60 μm, and for the experiments presented in this chapter a silicon substrate with a thickness of 525 μm is considered.

The enhancement of the incoming electric field at the resonance frequency in an isolated, sub-wavelength ($L, w < \lambda_0$) slot aperture in an infinite metallic ground plane is $E_{slot}/E_{inc} \approx (3/\sqrt{8})L/w$. This field enhancement is associated with a transmittance normalized to area of $T_{res} \approx (3/\pi)\cdot(L/w)$ [166]. The transmission through a periodic array of holes in a metal film is determined by the interplay between the superposition of the field transmitted through the individual apertures and the possibility of excitation of lattice modes mediated by surface plasmon polariton (SPP), with extraordinary transmission both at the individual aperture resonance and at additional resonances corresponding to the lattice modes [159]. In the THz range, where the conductivity of metals is very high, and the SPP propagation constant is close to that of free space, the lattice mode frequencies are given with high precision by

$$v_{lat}(j,k) = \frac{c}{n}\sqrt{\frac{j^2}{P_X^2} + \frac{k^2}{P_Y^2}}, \tag{5.2}$$

where j and k are integers, P_X and P_Y are the lattice constants (see Fig. 5.2), and n is the refractive index of the material above the gold film. The lattice modes can be excited on both the air-metal and metal-substrate interfaces. Here, the metal films are thicker than the skin depth, and thus SPP waves on the two sides of the metal film are independent of each other. For the same reason, the frequency-dependent transmission of the field will be mainly influenced by the SPP waves on the metal-substrate interface. Bitzer *et al.* [158] showed that at these resonance frequencies, the radiation pattern from an array of dipoles develops strong side lobes in the plane of the interface, giving rise to a significant electromagnetic coupling between the adjacent elements. In a transmission experiment with resonant elements periodically spaced on a dielectric substrate, these lattice resonances lead to losses at the lattice mode frequencies in the transmitted far field. In the case of apertures in a metallic film, the component of the scattered field at the apertures that gets coupled to SPP modes along the metal interface can interact constructively with the enhanced field in the neighboring apertures. This gives the possibility of additional enhancement of the field in the aperture compared to the field enhancement in an isolated aperture, which is observed as a further increase of the extraordinary transmission [157].

5.2. Fabrication and field enhancement measurements

In order to study the interaction between the resonant apertures and lattice modes, three series of slits in periodic arrays were fabricated using standard UV photolithography. Each sample had an area of 9x9 mm^2. Table 1 gives an overview of the three series of samples fabricated, with specification of the slit length L and lattice parameters P_X and P_Y, and the associated resonance frequencies. In all cases the slit width (w) was 1.5 μm and the thickness of the gold film was 200 nm i.e. thicker than the skin depth in the relevant THz range (70 nm at 1 THz). Fig. 5.2 shows a scanning electron microscopy (SEM) image of one of the samples, indicating the various dimensions of interest. The inset in the upper right corner shows a zoom of a section of a slit. The arrays were fabricated on a 525 μm thick high resistivity silicon (HR-Si) substrate.

The frequency-dependent transmission of the samples were measured at normal incidence with the Picometrix T-Ray 4000 fiber-coupled THz spectrometer using focusing lenses with effective focal lengths of 3", resulting in a spot size at the sample position in the focal plane of approximately 1.5 mm (full width at half maximum, FWHM) at 1 THz. The polarization of the THz beam is parallel to the width of the slit. Using Eqs. (5.1) and (5.2), the samples were designed so that the slit resonances and the lowest order lattice modes were within the useful bandwidth of the spectrometer, i.e. from 0.1-1.6 THz. The transmission of the samples was measured by the standard technique of recording a reference signal $E_{ref}(t)$ with an empty beam path, and a sample signal $E_{sam}(t)$ at normal incidence through the sample. After Fourier transformation of the signals, the field amplitude transmission coefficient through the film was then calculated as $T(\nu) = [4n_{Si}/(n_{Si}+1)^2] \cdot E_{sam}(\nu)/E_{ref}(\nu)$ to take the Fresnel losses of the substrate of the sample into account.

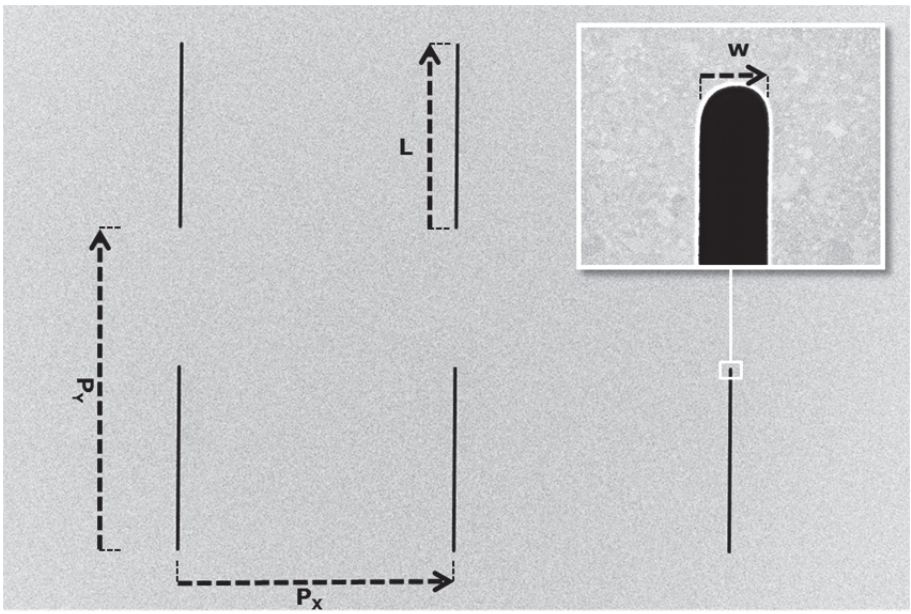

Fig. 5.2: SEM image of a typical slit array. Then inset shows a zoom of a slit. In this specific case, L = 50 µm, P_X = 70 µm, P_Y = 110 µm, and w = 1.5 µm.

Table 4: Overview of sample series, critical dimensions and resonance frequencies

Series	I	II	III
L [μm]	30 – 105	75	75
ν_0 [THz]	1.815 – 0.537	0.763	0.763
P_X [μm]	70	30 – 170	110
$\nu_{lat}(1,0)$ [THz]	1.254	2.926 – 0.516	0.798
P_Y [μm]	110	120	80 – 170
$\nu_{lat}(0,1)$ [THz]	0.798	0.731	1.097 – 0.516

5.3. Field enhancement in periodically arranged slits

The frequency-dependent field enhancement inside the slits is inferred from transmission measurements as $T(\nu)/\beta$, where $T(\nu)$ is the measured transmission through the film obtained in experiment and β is the fill factor [156]. For the slit array showed in Fig. 5.2, $\beta = (P_X \cdot P_Y)/(L \cdot w)$. The measured transmission was independent of detailed alignment of the sample in the horizontal and vertical directions due to the large spot size of the THz beam.

The results of the measured field enhancement for samples are shown in the left columns of Fig. 5.3, Fig. 5.4, and Fig. 5.5, where the right columns are corresponding full-wave electromagnetic simulations using the time-domain solver of CST Microwave Studio, using periodic boundary conditions with a unit cell size defined by P_X and P_Y, and with a broadband (0-4 THz) excitation pulse polarized in the x-direction and placing a near-field probe in the center of the slit to record the field enhancement. The calculated lattice modes are indicated as the white dashed lines showing the order (j,k).

Fig. 5.3 shows the results from sample series I where L is tuned from 30 to 105 μm in steps of 5 μm. When L is increased the resonance frequency is reduced, as expected. The field enhancement is highest when the slit resonance crosses the lattice mode resonance (0,1) whereas the lattice modes (1,0) and (1,1) result in black bands of destructive interference, which is

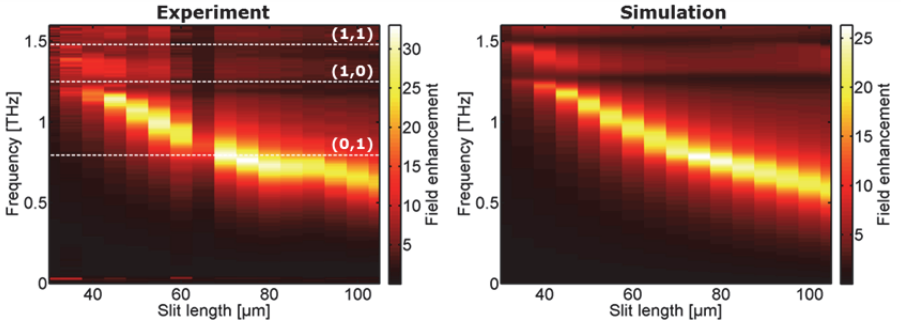

Fig. 5.3 Experimental (left) and simulation (right) results of field enhancement inside slits when the length is varied and the lattice parameters are P_X=70 μm and P_Y=110 μm. The white dashed lines indicate lattice modes.

typically seen for Fano resonances in plasmonic structures [171]. It is noted that this Fano resonance behavior is observed for coupling to lattice modes having a non-zero mode order in the horizontal direction $(j \neq 0,k)$, as expected due to the polarization of the THz field. However, there is still coupling to $(0,k)$ lattice modes, leading to additional enhancement of the field as the slit resonance crosses the (0,1) lattice mode. Although the (0,1) lattice mode itself is not visible in neither experiment nor simulation, the effect on the field enhancement is obvious. Field fringing at the ends of the slit leads to a non-zero *z*-component of the field at these positions that couples to SPP waves in the *y*-direction. The coupling is weaker than in the x-direction by a factor given approximately by the aspect ratio of the slit, *w*/*L*, although a significant influence on the field enhancement can still be observed. It is noted that in the experiment, the sample with L = 65 μm shows significant lower transmission (and thus lower field enhancement) than the neighboring samples, although the transmission resonance is at the expected frequency. No visible damage to the surface or unexpected deviations from the design dimensions have been found, so the reason for the isolated discrepancy is not clear. It is suspected that residual photoresist unintentionally left on the sample surface may be a possible origin of this unexpected behavior.

To investigate the coupling of the slit mode to the lattice modes in the horizontal direction, sample series II is designed so that L and P_Y are fixed, and P_X is varied so that the lowest order lattice mode resonance (1,0) crosses the slit resonance. The results of the experiments and simulations

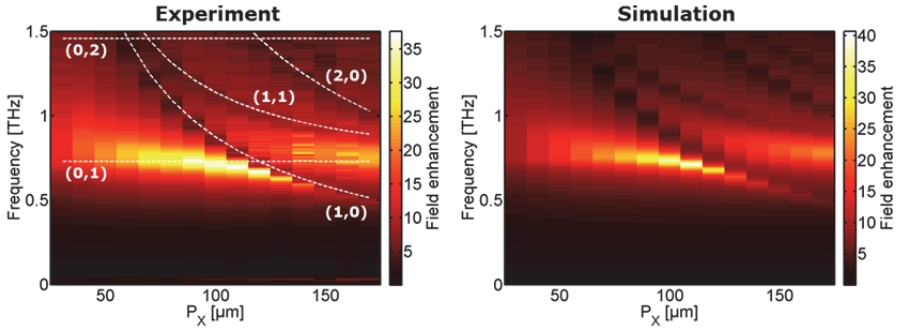

Fig. 5.4: Experimental (left) and simulation (right) results of field enhancement inside slits when P_X is varied while L=75 μm and P_Y=*120* μm.

when varying P_X are shown in Fig. 5.4. The calculated lattice modes that only have a component in the y-direction, i.e. of the orders $(0,k)$, are indicated with horizontal dashed lines, whereas the frequencies of the calculated lattice modes $(j \neq 0,k)$ are reduced when P_X is increased. These lattice modes are again clearly visible in the measurements and simulations as black bands due to the Fano-like behavior, and agreeing well with the calculated lattice mode frequencies. Most significant is the (1,0) mode. When this approaches the slit resonance, the slit resonance redshifts slightly and sharpens. When the lattice mode crosses the slit resonance, the slit resonance blueshifts rapidly and broadens as expected for an avoided crossing due to the coupling between the two modes. The field enhancement of the slit resonance reaches its highest value of more than 35 just before this avoided crossing. The (0,1) lattice mode is again not visible, but serves to further strengthen the field enhancement with the avoided crossing between the slit mode and the (1,0) lattice mode pushes the slit mode into resonance with the (0,1) mode.

The results of the series III of samples where P_Y is varied is shown in Fig. 5.5. The fixed value of P_X is chosen so that the (0,1) lattice mode is slightly blueshifted from the slit resonance. Even though no spectral signatures from the lattice modes (0,1) and (0,2) are seen, an additional enhancement when the frequency of the lattice mode (0,1) approaches the slit resonance is observed, similar to the behavior seen in sample series I and II.

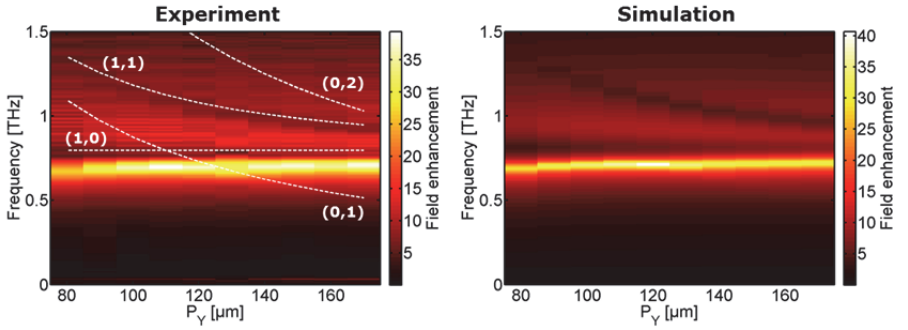

Fig. 5.5: Experimental (left) and simulation (right) results of field enhancement inside slits when P_Y is varied while L=75 μm and P_X=*110* μm.

The spectral features of experiments versus simulations for the three series of samples shown above are in very good agreement. The magnitude of the field enhancement for the experiments and simulations of all cases are shown in Fig. 5.6. In general, the experimentally observed field enhancements are in reasonably good quantitative agreement, both concerning the magnitude and the behavior when the different dimensions are varied. A behavior with additional enhancement when the lattice modes match the slit resonance is observed, both with variation of L, P_X and P_Y. This is in contrast to the expected enhancement for an isolated slit which should increase monotonically with L, and demonstrates the positive effect of coupling between the lattice modes and the slit resonances on the obtainable field enhancement.

5.4. Field distributions

Especially in Fig. 5.6(a) the measured field enhancements are slightly higher

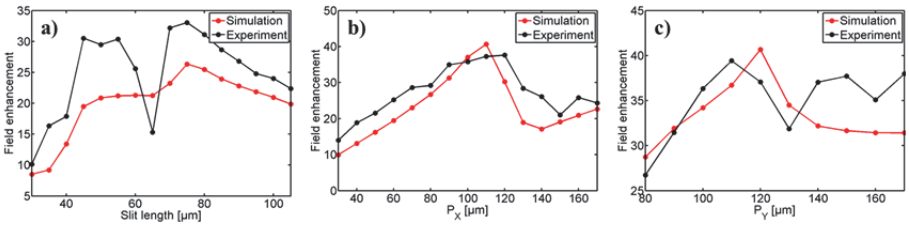

Fig. 5.6: Field enhancements obtained by simulation (black) and experiment (red) when a) L is varied while P_X = 70 μm and P_Y = 110 μm, b) P_X is varied while P_Y = 120 μm and L = 75 μm, and c) P_Y is varied while P_X = 110 μm and L = 75 μm.

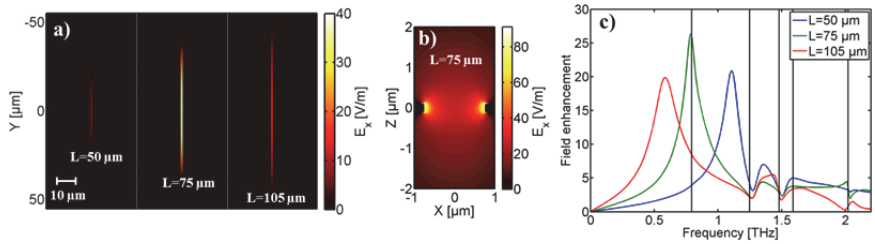

Fig. 5.7: (a) Field distribution of E_x shown in the *XY*-plane ($Z = 0$) inside three slits of lengths L = 50, 75 and 105 µm, with P_X = 70 µm and P_Y = 110 µm at $\nu = 0.79THz$. b) E_x shown in the *XZ*-plane ($Y = 0$) on resonance for L = 75 µm. c) Spectral distribution of the field enhancement probed in the center of the slits. Vertical lines indicate lattice modes.

than the field enhancement obtained in the simulation results. The reason for this discrepancy may be found in the way the field enhancement is inferred experimentally. Comparing the field enhancement deduced from the far-field measurements with the simulations based on a near-field probe in the center of the slit assumes that the field is uniform within the slit, an assumption which may not always be precise. For this reason the field distribution inside the slit is investigated as shown in Fig. 5.7. For the consideration of the field enhancement inside the slits at a specific frequency, Fig. 5.7(a) shows the field enhancement of slits of three different lengths each in an array of identical slits with lattice pitch P_X = 70 µm and P_Y = 110 µm at 0.79 THz, i.e. the frequency of the (0,1) lattice mode. It is seen that the field distribution is similar to the TE_{01} rectangular waveguide mode, with the highest field strength at $L/2$. The field enhancement is largest for $L = 75$ µm, where the slit resonance overlaps well with the lattice mode. In a view of the field distribution of E_X in the XZ-plane (Y = 0) it is seen that the field is highest close to the edges where the field enhancement reaches a value of more than 80, which is over twice that of the center of the slit (Fig. 5.7(b)). Here the center of the gold layer is centered Z = 0 with a thickness of 0.2 µm, and the silicon substrate is located at positive Z values larger than 0.1 µm. The spectral distributions of the field enhancement in the center of the three slit lengths are shown in Fig. 5.7(c) where the coupling of the slit resonance to the lattice modes again is clearly seen. Thus, the average field strength in the slit is actually larger than the value sampled in the center of the slit, and this may be the reason for the higher enhancement deduced from experiment than from simulation (Fig. 5.6).

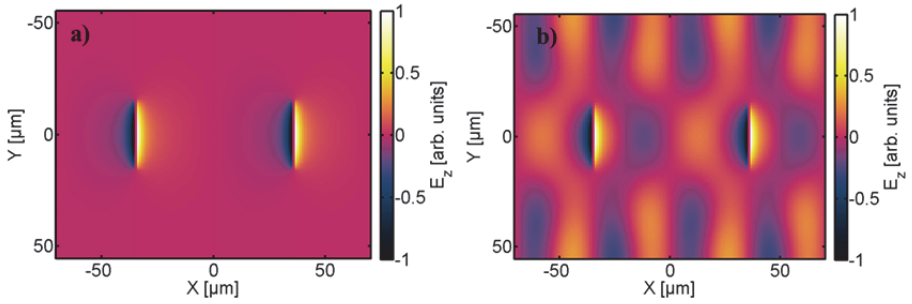

Fig. 5.8: Field distribution (E_z) of lattice modes in slit arrays of $L = 30$ µm, $P_X = 70$ µm and $P_Y = 110$ µm probed in the silicon substrate at $Z = 0.1$ µm above the metal at the frequencies (a) $\nu_{lat}(0,1) = 0.79$ THz and (b) $\nu_{lat}(2,1) = 2.61$ THz.

To investigate the spatial distribution of the lattice modes, which in the case of slits in a metallic film are expected to be SPP modes, simulations of the Z-component of the field (E_Z) are performed. Fig. 5.8(a) and (b) show the field distribution of E_Z in the XY-plane on the backside of the gold surface, 0.5 µm into the substrate. To enable excitation of higher-order lattice modes, the slit length is here chosen to be L = 30 µm, while the lattice size is again 70x110 µm. For the lowest lattice mode (0,1) shown in Fig. 5.8(a) the field is concentrated around the slits (located at X = ±35 µm, respectively). The field pattern for the lattice mode (2,1) is shown in Fig. 5.8(b) where the standing SPP waves between the neighboring slits are clearly seen.

5.5. Coupling mechanism

In order to study how the electric field decays from metallic surface compared to plasmonic waves, the Z-component in the XZ-plane is investigated. In Fig. 5.9 E_z is shown in the XZ plane where the slit is at (0,0), the air side is at Z < 0, and Si is at Z > 0. The field pattern of standing waves as observed in Fig. 5.8(b) is present again in Fig. 5.9(a), and it is observed that the field is concentrated in the Si substrate. To study the field distribution along Z isolated from the enhanced field close to the slit, a cross section at the second local maximum in Si substrate at X = 26 µm (dashed line in Fig. 5.9(a)) is plotted in Fig. 5.9(b) as the red curve. The simulation shows the full electromagnetic solution, but a simple superposition of a spherical wave and a standing SPP wave (exponentially decaying in the Z direction), shown as the black curve, reproduces most of the features. The

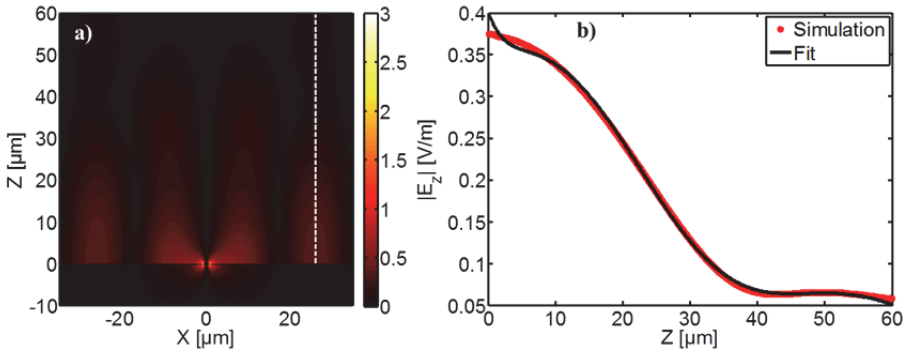

Fig. 5.9: Z component of the electric field ($|E_z|$) simulated at $\nu = \nu_{lat}(2,1) = 2.61$ THz for slit arrays of L=30 µm, $P_X = 70$ µm and $P_Y = 110$ µm in (a) the XZ plane and (b) along Z at X = 26 µm (red curve, marked with the dashed line in (a)). The black curve is a fit to the simulated data based on a superposition of a spherical wave and a SPP wave.

SPP penetration depth into the substrate is substantial (tens of µm) due to the high conductivity of the metal. Nevertheless, the characteristics of an SPP wave are clearly present, indicating that the coupling between slits is indeed due to SPP waves, and not unbound waves which form the coupling mechanism in [158]. The amplitudes for the spherical wave and the SPP wave in the fit suggest that the coupling to the spherical wave is approximately twice as strong as to the SPP wave.

5.6. Conclusions and outlook

In this chapter it has been investigated how the resonance of microslits in a metallic film arranged in a periodic array can couple to the lattice modes of the array. Energy from the incident THz pulse can be coupled to SPP waves, and is lost in the case of a single, isolated slit, while it can be coupled back into the adjacent slits in an array, and thus contribute further to the field enhancement and the extraordinary transmission. By careful tuning of the lowest-order lattice modes in both directions of the 2D periodic array to the resonance frequency of the slit mode, a significant additional field enhancement achieved, here in the order of 60%, and specifically with a field enhancement increasing from 25 to 40 for a slit with resonance frequency at 0.7 THz. In this frequency range, $LiNbO_3$ sources offer THz fields strengths of 1 MV/cm, and thus, it becomes possible to reach into the multi-10-MV/cm field regime at low THz frequencies, using a simple

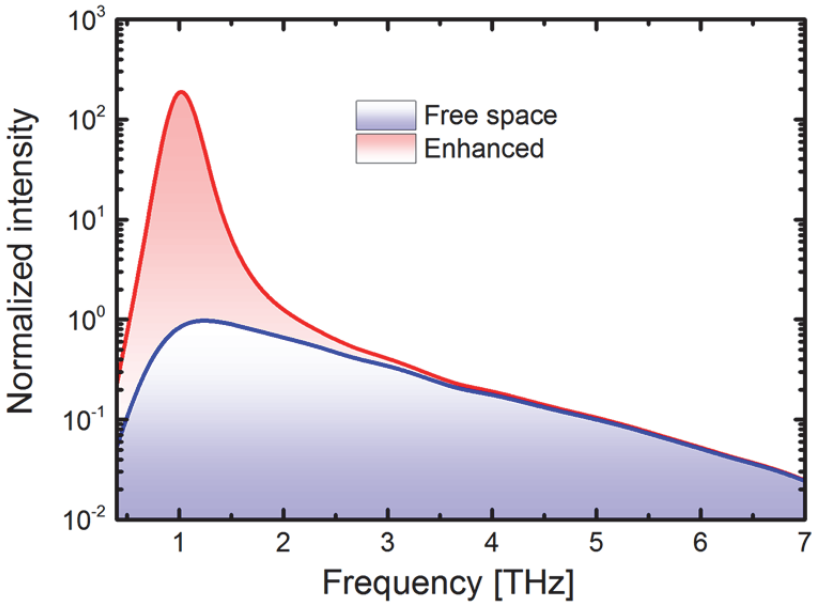

Fig. 5.10: THz spectrum measured from a 2-color air plasma with 1300 nm as the fundamental wavelength (blue curve) together with an illustration of field concentration from a slit array resonant at 1 THz (red curve).

structure which is easily fabricated by standard UV photolithography. At the same time, the overall transmission coefficient through the sample is of the order of 5%, ensuring good signal-to-noise ratio in the detection of the transmitted signal, even in the case of low-repetition-rate experiments. Alternatively, laser systems operating at high kHz to low MHz repetition rates can be applied to generate THz fields in the range of 1-10 kV/cm [1], which then can be enhanced to several hundred kV/cm in the structure. Significant nonlinear effects can be expected in particular in semiconducting systems at such field strengths [172-174], and therefore, the slit array structures may enable highly sensitive nonlinear studies using high repetition rate spectroscopic systems, with all the advantages in terms of stability noise such systems offer, compared to low-repetition rate amplified laser systems.

Plasmonic structures such as those employed here as field enhancing slit arrays can be scaled to cover other frequencies than the frequencies within a PCA spectroscopy system as shown here. For example, the 2-color air plasma THz sources can generate frequencies up to more than 30 THz, but if a specific frequency band of a few THz is considered within this bandwidth, the intensities within this band will be low. However, field enhancing slits

designed by using the here described criteria can be used to concentrate the field near a specific frequency, which is illustrated in Fig. 5.10, where the spectrum measured from the 1300 nm 2-color air plasma has been enhanced at 1 THz using simulation results of a lattice-mode optimized slit array resonant at 1 THz. It is seen how the field enhancement results in a spectrally concentrated intensity that is orders of magnitude higher than in free-space.

Related to the study presented here, samples resonant at 2.0 and 2.6 THz have been fabricated with the purpose of studying resonances of Riboflavin with a 2-color air plasma source. However, it was found that absorption cross section when depositing the sample into the 1.5 μm wide slits was too low to achieve significant sensitivity enhancement to resolve the Riboflavin phonons sufficiently. In future studies this experiment will be repeated with slit arrays where the width is reduced to 200 nm, which, according to [19] will increase the absorption cross section by 7.5 times. The samples with reduced slit width are fabricated with e-beam lithography, which is significantly more costly and time consuming than with UV lithography.

Chapter 6

Nonlinear terahertz spectroscopy

In this chapter two methods of nonlinear THz spectroscopy will be demonstrated and discussed: first in a configuration where nonlinear effects are induced by a single, intense THz pulse, and the nonlinear response of the sample is detected as the modifications on the transmission of that same pulse (one dimensional spectroscopy), and secondly when two THz pulses interact with a sample. Traditionally, THz spectroscopy in an ordinary THz-TDS configuration has been known as "static spectroscopy" meaning that the optical properties are measured from the sample while the field strength of the incident THz field is low and thereby not expected to cause any change in the dynamics in the sample. However, in Chapter 2, results of MD simulations showed that nonlinear effects in hydrogen-bonded crystalline materials can be expected with field strengths of the order of MV/cm, and as described in Chapter 3, intense THz sources based on amplified laser systems now offer such field strengths. Nonlinear 1D spectroscopy has already been performed by Jewariya *et al.* where intense THz pulses generated from a $LiNbO_3$ crystal was used to induce nonlinear effects in crystals of amino acids [16]. In that investigation, bleaching together with a redshift of an absorption peak was observed when the sample was exposed to field strengths in the order of 100 kV/cm. Inspired by this, the first part of this chapter will study if a single, intense THz pulse can induce nonlinear effects in samples of lactose and sucrose. Additionally, THz spectroscopy using intense pulses has also been performed on well-known nonlinear semiconductor samples of ZnTe and Si, but these results are only discussed briefly here.

It is possible to study the dynamics in samples by performing an experiment in a pump-probe configuration where the sample is exposed to two

independent pulses, and the time delay between the two pulses is controlled by a delay stage. Essentially, the first pulse pumps the sample and the second pulse probes the pump-induced dynamics in the sample some time later. The choice of pulses obviously depends on the application; for example optical-pump THz probe has been used to investigate carrier dynamics above the bandgap in semiconductors [175-177], superconductors[178], solar cell materials [125] etc. In the opposite configuration, THz-pump optical-probe experiments have been performed in order to demonstrate THz induced phenomena such as the Kerr effect in various liquids [179], soft glasses [180] and EO crystals [181]. Alternatively, THz induced effects can also be investigated by probing with another THz pulse, in a THz-pump THz-probe experiment. In this case the two THz pulses are typically generated from the same emitter, but the THz probe pulse is much weaker than the pump pulse. This method has the advantage of directly probing the THz induced effects while eliminating any effects from optical light [182] and for this reason it has been able to prove several THz phenomena such as impact ionization [173], self-phase modulation [183] and nonlinear responses of electrons in semiconductors [174].

A more extended method for measuring dynamics in samples is 2 dimensional (2D) spectroscopy. Similar to THz-pump THz-probe spectroscopy, two THz pulses interact with a sample in a 2D spectroscopy experiment. However, the two methods are different in several ways. From an experimental point of view, the two THz pulses should be scanned across each other in the sample, and for this reason the pulses are most often generated from two different THz emitters. Secondly, both pulses can influence the sample, and for this reason the two pulses are typically similar in field strength. 2D spectroscopy has been widely used for investigation of vibrational IR modes where the pulses excite the sample in a non-collinear geometry in order to spatially separate the generated nonlinear contributions with respect to their k-vectors [1, 184]. Using the advantages of THz-TDS (field-resolved detection) it has been shown that 2D spectroscopy can be performed in a collinear geometry in a manner so that the nonlinear responses from mixing processes are separated in time domain [4, 185]. Such 2D THz experiments have been performed on semiconductor quantum wells [4], bulk semiconductors [186-188] and graphene [189], where the detection scheme simultaneously measures the response of the sample when both pulses are applied versus when each of the pulses are applied

individually. This gives the possibility to directly map out nonlinear responses.

While most of the above mentioned experiments have been applied on semiconductors and quantum systems, the scope of this thesis chapter is to investigate nonlinear phonon responses in crystalline hydrogen bonded materials such as sucrose. With the 1 dimensional spectroscopy results of lactose and sucrose presented in section 6.1, supported by the CASTEP simulated results presented in Chapter 2, a 2D spectroscopy platform for investigation of nonlinear molecular dynamics is presented in section 6.2. Using this 2D configuration, nonlinear effects have for the first time been observed in sucrose, and are presented and analyzed in section 6.2.2.

6.1. One dimensional spectroscopy

In 1D THz spectroscopy the optical properties of a sample are extracted from the change in optical path length, phase and amplitude of a THz pulse after interacting with the sample. A spectroscopic investigation of a sample can be done in several different geometries. In this thesis all experiments has been performed in a transmission geometry i.e. the electric field transmitted through the sample is detected. The transmission geometry, which is the simplest and most convenient experimental geometry, requires that the sample is fairly transparent to THz radiation. If this is not the case samples can also be investigated in an ordinary reflection geometry, or the attenuated total reflection (ATR) geometry where the THz pulse interacts with the sample through a silicon prism [190, 191]. A challenge associated with reflection spectroscopy measurements is to precisely obtain a reference measurement and thereby obtain the phase change information. Examples of solutions to this are using a THz transparent window in front of the sample and use the reflection from the first interface as reference [192, 193] or using a reflective surface next to the sample [194].

The study of optical properties of a sample such as its absorption or transmission when the field strength is varied can be done in a z-scan experiment, where the field is increased as the sample is moved in the z-direction towards the focus of the beam [195], or by placing the sample in focus and attenuating the incident THz beam. Since the sucrose samples used here did not have a completely uniform interface, the latter method is chosen for the experiments presented in the following using a pair of wiregrid polarizers for attenuating the THz beam before the sample. In this

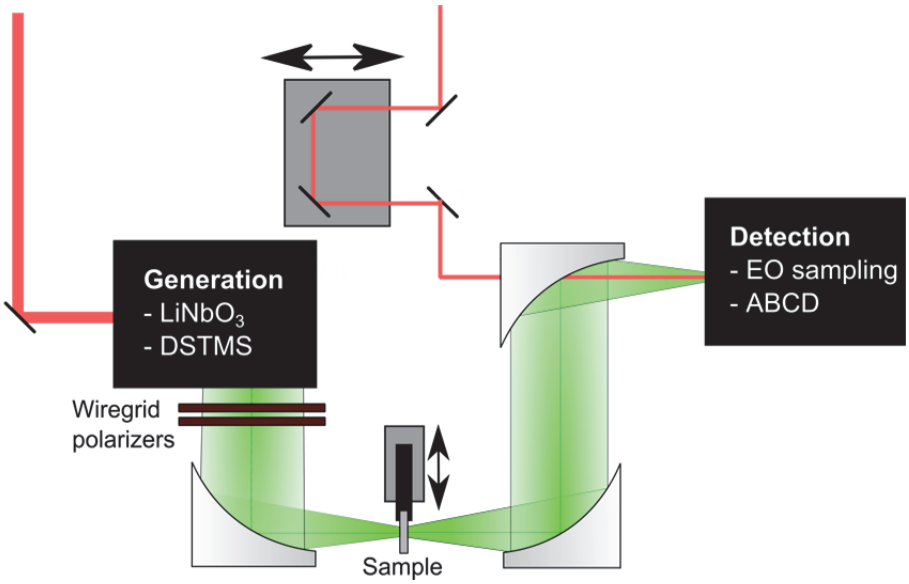

Fig. 6.1: Setup used for 1D spectroscopy. The THz source is either a DSTMS or a $LiNbO_3$ crystal and the detection is EO sampling or ABCD.

manner, the spot size remains constant at different field strengths, and any effects from an inhomogeneous sample thickness are minimized. Si wafers can also be used to attenuate the THz beam, but it was observed that the transmission of the most intense THz beam generated from DSTMS through Si was nonlinear, even if the wafer was placed in the unfocused beam, and for this reason it has here been avoided to use Si wafers as an attenuation parameter.

In the following the mathematical relations needed for extracting the refractive index and absorption spectra are explained in section 6.1.1, and the subsequent sections present the results. All experiments are performed in the configuration shown in Fig. 6.1 where the THz generation is either based on $LiNbO_3$ or DSTMS, and the detection method is either EO sampling or ABCD. In either case the THz field strength is controlled by a pair of wiregrid polarizers. The rear polarizer is fixed to ensure a horizontal polarization while the front polarizer is rotated between 0 and 90 degrees with respect to the rear polarizer. The THz beam is focused onto the sample using a 2" off-axis parabolic mirror, after which the THz beam is collimated and refocused onto the detection medium with a 4" and 2" off-axis parabolic mirror, respectively. The sample is mounted on a μm precision stage

allowing for translaton out of the beam path for reference measurements, and returning afterwards returning the sample to the same position as before.

6.1.1. Absorption spectra and the refractive index in transmission spectroscopy

The measured amplitude and phase change of an electric field transmitted through a sample makes it possible to extract both the frequency dependent permittivity, conductivity, refractive index and absorption of the sample [196]. For the investigation of nonlinear dynamics in phonon modes, absorption spectra are the most convenient characterization of the studied samples. Below it is described how absorption spectra are extracted from the time traces recorded in a THz transmission spectroscopy experiment. Without taking the roundtrip reflections in the sample into account, the THz field transmitted through a sample is given by

$$E_{sam}(\omega) = E_0(\omega) T e^{-\alpha d/2} e^{in\omega d/c} \tag{6.1}$$

where α is the absorption coefficient, d is the sample thickness, n is the refractive index and T is the total amplitude transmission factor calculated from the Fresnel equations [197]

$$T = T_{air\to sample} \cdot T_{sample\to air} = \frac{2n_{sample}}{n_{air}+n_{sample}} \cdot \frac{2n_{air}}{n_{sample}+n_{air}} = \frac{4n(\omega)}{(n(\omega)+1)^2}. \tag{6.2}$$

From the experiment the sample pulse $E_{sam}(\omega)$ and a reference pulse $E_{ref}(\omega) = E_0(\omega)e^{i\omega d/c}$ are compared so that

$$\frac{E_{sam}(\omega)}{E_{ref}(\omega)} = Ae^{i\phi(\omega)} = Te^{-\alpha d/2} e^{i(n-1)\omega d/c}, \tag{6.3}$$

where A is the amplitude change and ϕ is the phase change. The index of refraction can then be extracted from the phase change

$$n(\omega) = 1 + \frac{\phi c}{\omega d}, \tag{6.4}$$

and the absorption is extracted from the amplitude change (including the Fresnel coefficient)

$$\alpha(\omega) = \frac{-2}{d} \ln\left(\frac{(n+1)^2}{4n} \cdot \frac{|E_{sam}(\omega)|}{|E_{ref}(\omega)|} \right). \tag{6.5}$$

When measuring absorption spectra using a specific THz source and detector it is important to consider in which frequency range the system can actually measure the absorption, and how high an absorption can be measured within this spectral range. This maximum absorption range can be expressed as

$$\alpha_{\max} = \frac{2}{d}\left(DR \frac{4n}{(n+1)^2} \right) \tag{6.6}$$

where *DR* is the dynamic range i.e. the reference spectrum normalized so that the noise floor equals 1 [43]. In other words, $\alpha_{\max}$ corresponds to when the absorption is so high that the transmission through the sample is at the same level as the noise floor. In practice, measuring on single crystals with sharp absorption lines such as sucrose, it is desirable to use a crystal which is as thin as possible to avoid that the absorption saturates within the frequency range of interest. For polycrystalline materials, this problem is often solved by pressing the sample into a pellet which is a mixture of polyethylene (PE) and the sample powder itself. Since PE can be transparent for THz frequencies up to 10 THz [121], the sample can be mixed in a ratio so that the absorption of the pellet is suitable for the dynamic range of the spectroscopy system.

6.1.2. Lactose

Lactose ($C_{12}H_{22}O_{11}$) is an example of an organic material, which, because of its large molecular weight, has resonant absorption features in the lowest part of the THz spectrum. Particularly, it has an absorption peak at 0.53 THz, which originates from a collective vibrational transition in the molecule [198]. With the general prediction of anharmonic vibrational potentials for hydrogen-bonded crystalline substances [36, 199] and the 0.53 THz resonance positioned at the peak of the spectral energy distribution of the THz spectrum generated with $LiNbO_3$, lactose seems like an obvious candidate for a nonlinear study.

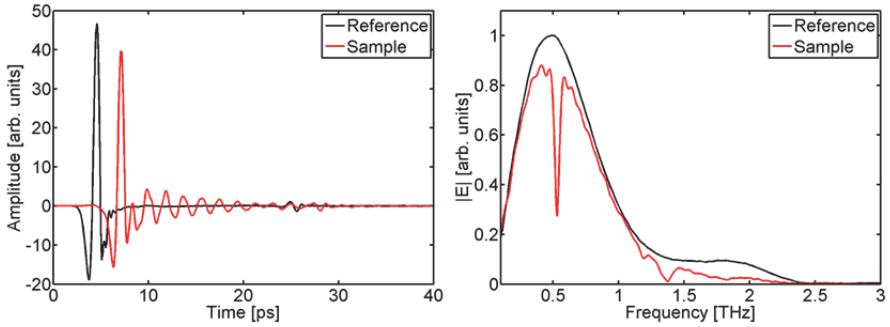

Fig. 6.2: Time-domain traces (left) and corresponding spectra (right) measured for lactose (red traces) and through air (black traces).

The sample studied here is a 50/50 mixture of α-lactose monohydrate (Sigma-Aldrich L3625) and PE (Sigma-Aldrich 434272) pressed into a pellet with a thickness of 1.39 mm. The sample was investigated with a THz-TDS system where $LiNbO_3$ was the THz source and the EO sampling method was used for detection. As described in Chapter 3, 120 fs pulses at 800 nm with tilted pulse fronts were used for THz generation in $LiNbO_3$, and the THz beam was focused onto the sample using three off-axis parabolic mirrors as described by Hirori *et al* [93]. At the sample position, the peak field strength is estimated from the EO sampling signal to be approximately 400 kV/cm. The EO sampling was performed with a 1 mm thick ZnTe crystal since the bandwidth generated with $LiNbO_3$ is covered with ZnTe detection. In total 8 sample and reference measurements were recorded at different peak field strengths by adjusting the front wiregrid polarizer. The time traces measured with the maximum field strength are shown in Fig. 6.2 where the black curve is the reference pulse recorded without the sample, and the red curve is the pulse transmitted through the lactose pellet. It is seen that the sample has been mixed so that the transmission is high i.e. more than 80% of the peak field. For both pulses the first roundtrip reflection in the detection crystal (ZnTe) is seen approximately 21 ps after the main peaks. For the subsequent data analysis this reflection is eliminated by multiplying a Tukey window to the time trace. A Tukey window is a tapered cosine window meaning that it has a value of 1 in the region of interest and smoothly decays to 0 where the signal should be eliminated (see Appendix C). Since the frequency resolution is related to the length of the time scan via the Nyquist criterion [200]

$$\Delta\nu = \frac{1}{\Delta t \cdot N} \tag{6.7}$$

where Δt is the time resolution and N is the number of datapoints, the time scan should be as long as possible to achieve a high frequency resolution. However, any reflections (from detection crystals, samples, silicon wafers etc.) are eliminated using the Tukey window in order to avoid interference ripples in the spectrum. A round-trip reflection in the lactose sample used here should arrive at the detection spot approximately 15 ps after the main peak, but is not observed, possible due to the low refractive index of the pellet. Additionally, zero padding is used to achieve smooth spectral curves. The spectra corresponding to the windowed and zero-padded time traces are shown in left panel of Fig. 6.3. The absorption features at 0.53 and 1.37 THz are already clearly seen in the sample spectrum, but for a more thorough

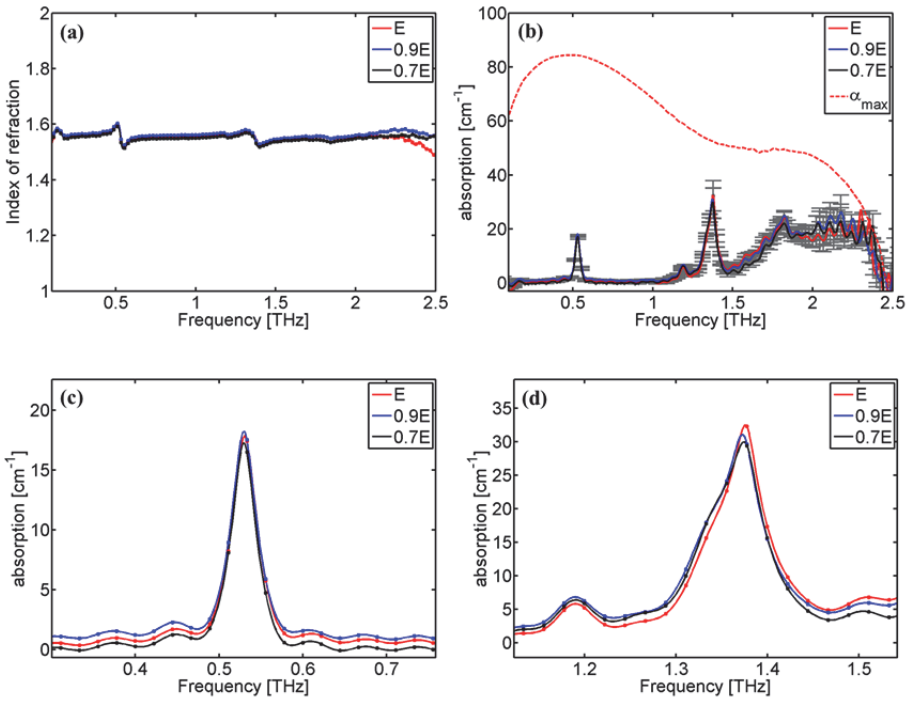

Fig. 6.3: Results from the spectroscopic investigation of lactose shown for three different field strengths of E, 0.9E and 0.7E as the red, blue and black curve, respectively. (a) is the refractive index, (b) is the absorption spectrum with errorbars and α_{max} calculated as the red dashed line, (c) is a zoom of the 0.53 THz peak and (d) is a zoom of the 1.37 THz peak.

analysis the refractive index and absorption spectra are calculated as described in section 6.1.1. The results of this are shown in Fig. 6.3, where the three field strength measurements of E, 0.9E and 0.7E are selected for illustration and indicated with the red, blue and black curves, respectively. The measured index of refraction is shown in (a), where mean refractive index of the PE-lactose mixture is approximately 1.56, which is well in agreement with the previous reported refractive index of pure lactose of approximately 1.7 [201]. The three curves are overlapping well up to frequencies higher than 2 THz after where the dynamic range becomes small. The absorption spectra are shown in (b) together with the maximum absorption, $\alpha_{\max}$, indicated as the red, dashed line. Each of the time traces is averaged over three individual scans, and the grey errorbars are calculated from the standard deviation of these. It is seen that the size of the errorbars increases significantly when the frequency increases, and at the same time $\alpha_{\max}$ decreases. The measured absorption exceeds $\alpha_{\max}$ at approximately 2.3 THz so the apparent absorption at higher frequencies than that cannot be reliably extracted from this experiment. Zooms of the two main absorption features at 0.53 and 1.37 THz are shown in (c) and (d), respectively. Here, the solid curves are the absorption extracted when the zero padding and Tukey window is applied to the time traces, while the dots on the curves indicate the absorption calculated from the raw time trace manually cut at a zero-crossing before the reflection from the detection crystal. Both are shown here in order to ensure agreement between the two cases, since a wrongly applied window on a time trace can change the spectral features and unphysical artifacts of this can appear as absorption features. Here, the dots are well in agreement with the curves. As mentioned above, the response when increasing the incident field strength is expected to be most significant for the 0.53 THz phonon since the spectrum of the reference pulse maximizes roughly at this frequency. Considering the peaks of this phonon in Fig. 1.3(c) when the field strength is increased, the absorption appears to decrease slightly, which is both in agreement with the simulation in Chapter 2 and [16]. However, the change is so small that it does not overcome the experimental uncertainties indicated by the errorbars and is thereby not conclusive. Instead, considering the 1.37 phonon shown in Fig. 1.3(d), a somewhat more clear indication of a blueshift is seen. However, the errorbars are even larger here at these higher frequencies. Overall, any field dependent change of the absorption features cannot be concluded from this experiment. Nevertheless, this experiment *indicates* that it may be worth to

study nonlinearities at frequencies higher than 1 THz since this region hosted the most convincing indication of spectral changes when the field strength is increased. At the same time, this also suggests that $LiNbO_3$ is not the most ideal source for the study of nonlinear response of vibrational modes since its intensity above 1 THz is limited.

6.1.3. Sucrose

As discussed already for the CASTEP simulation in Chapter 2, sucrose is another hydrogen-bonded organic material which has several absorption peaks in the in the lower THz region, especially from 1 to 4 THz [2]. Ideal sources for this frequency range are the organic crystals of DSTMS and DAST. As shown in Chapter 3, these sources cover a bandwidth from approximately 1 to 5 THz and at the same time field strengths on the order of 5 MV/cm has been achieved in the focus of the DSTMS-generated beam. For the spectroscopic investigation of sucrose presented here, the DSTMS THz source in the configuration presented in Chapter 3 is used together with ABCD detection in order to ensure that the full bandwidth of the DSTMS spectrum transmitted through the sucrose sample is detected. In other to protect the DSTMS crystal from laser-induced damage, the repetition rate of the Spitfire Ace laser was set was set to 100 Hz instead of the 1 kHz delivered as standard by the system, and the TOPAS-Prime OPA wavelength was set to 1300 nm. Because of the low repetition rate it was necessary to record more scans to be averaged for each time trace in order to achieve a decent SNR, and here 15 scans were averaged for each measurement. Samples were prepared as slices from sucrose single crystals with a thickness about 1 mm to achieve the best compromise between mechanical

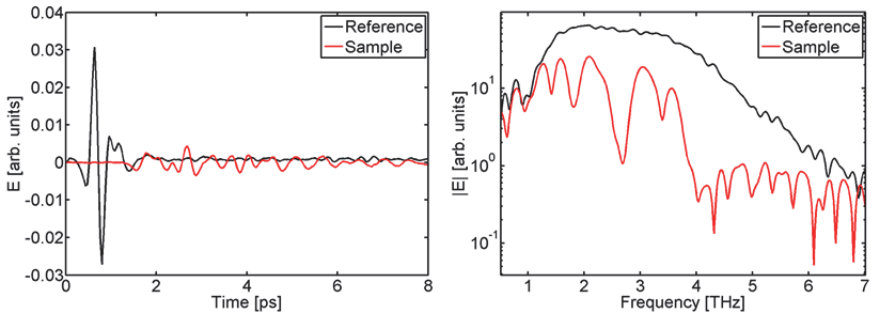

Fig. 6.4: Time-domain traces (left) and corresponding spectra (right) measured for lactose (red traces) and through air (black traces).

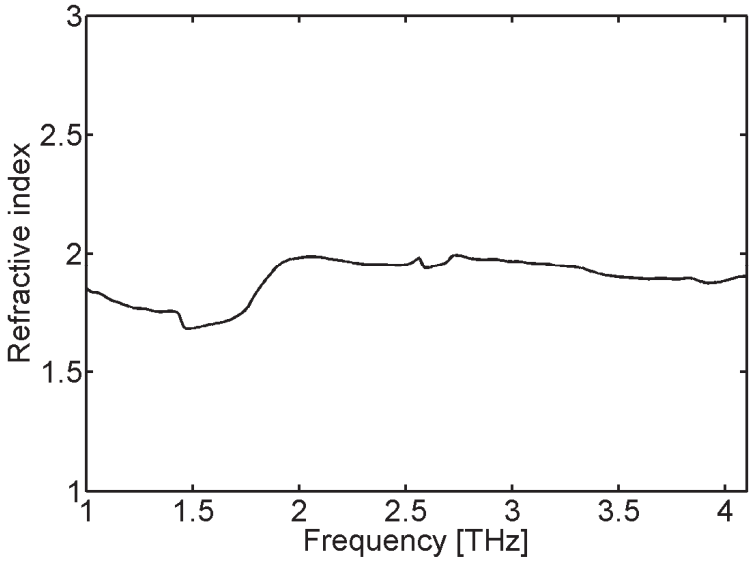

Fig. 6.5: Refractive index measured for sucrose.

stability and sufficient THz transmission. Thin sucrose slices are very fragile and it would easily break when polishing them in order to reduce the thickness, and at the same time scratches from the polishing results in a scattering surface. Instead the samples where cleaved by applying a slight impact force with a blunt object (a hammer) on the crystal planes perpendicular to the plane of interest. After some practice, thin samples could be easily prepared without scratches on the surface. A consequence of the cleaving is that the thickness is not always constant over the sample area. Typically, a sample with size 3x3 mm would have a thickness variation of 0.2 mm, and for this reason the sample is kept stationary over the experiment (with the exception of moving the sample in and out of the setup with a μm precision stage for reference acquisition). The optical properties of the different crystal planes have already been published [201-203], so here it has been chosen to perform the nonlinear study on the c'-axis (vertical axis of the (-100)-plane) since this has most has sharpest absorption features within the THz bandwidth achieved from DSTMS.

The time traces measured for the highest incident field is shown in Fig. 6.4 (left), where it is seen that the transmission of the peak field through the sample is only around 10 %. The corresponding spectra are shown in the right panel. For comparison with the literature the refractive index for this

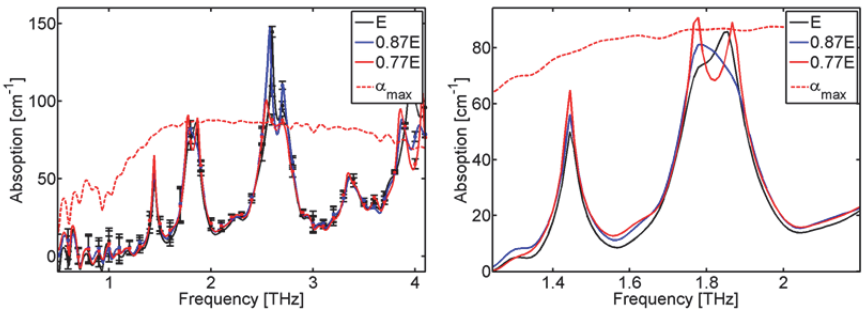

Fig. 6.6: Absorption spectra measured for sucrose from 0.5 to 4.1 THz (left) and a zoom of the features at 1.4 and 1.8 THz (right).

measurement is shown in Fig. 6.5, where the value just below 2 is well in agreement with the refractive index with what was reported in [36]. The measured absorption spectrum is shown in Fig. 6.6, where it further can be concluded that the absorption features are well in agreement with that was observed for the c'-axis for sucrose by Fischer [201] and Kröll *et al.* [202, 203]. Four distinct features are seen at 1.4, 1.8, 2.7 and 3.3 THz, where the 2.7 THz feature is exceeds the level of α_{max}. Most interesting is the absorption peak at 1.4 THz, which is identified to be the same feature as the 1.38 THz peak studied with CASTEP simulations in Chapter 2. In agreement with the MD simulations for sucrose, the absorption peak bleaches when the field strength is increased. The feature at 1.8 THz is possible a superposition of two absorption peaks, where the low-frequency peak seems to bleach in the same way, where the high-frequency peak does not show a clear trend.

To conclude the field dependent measurements on sucrose, a much clearer indication of phonon bleaching has been observed here than for the experiment performed on lactose. Possibly because the field strength for DSTMS is estimated to be around 10 times higher than for $LiNbO_3$, but another explanation can also be the advantage of the slightly higher frequencies of the modes suggest that the molecular vibrations may be a bit more confined. At the same time the many modes within considered bandwidth allows for nonlinear mode beating, which was observed in the MD simulations of sucrose. This will be investigated further in the 2D spectroscopy section.

6.1.4. ZnTe

In addition to the study of the two hydrogen-bonded organic crystals of lactose and sucrose presented above, two other obvious candidates for nonlinear spectroscopy are investigated. The first one discussed here in this section is ZnTe, which has been discussed several times previously in this thesis, since its high nonlinear coefficient makes it very applicable both for generation and detection of THz radiation. The absorption features above 3 THz that usually limits the generation and detection bandwidth when using ZnTe, are here investigated in a field-dependent study using the DSTMS source and ABCD detection in the same way as described in the previous section. The results of experiments performed on a 0.5 mm ZnTe crystal is shown in Fig. 6.7. The measured refractive index for the lowest field strength setting is shown in (a). With a value starting just below 3.2 and gradually increasing to approximately 3.6 at 4 THz, this is in excellent agreement with the results presented by Gallot *et al.* [85]. Considering the transmission spectra shown in Fig. 1.7(b), it is clear that transmission is significantly higher for the highest field strength, especially in the flat region

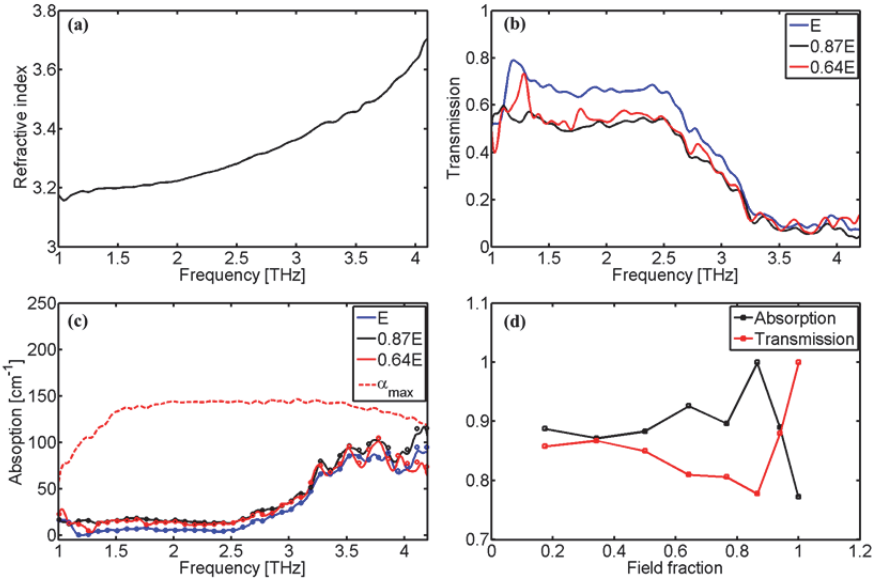

Fig. 6.7: Results of the spectroscopic investigation of ZnTe. (a) The measured refractive index at the lowest incident field strength, (b) transmission spectra, (c) absorption spectra and (d) mean transmission from 1.5 to 2.5 THz (red curve) and integrated absorption from 1.5 to 4 THz (red curve).

between 1.5 and 2.5 THz. Looking at the measured absorption in Fig. 1.7(c) in the same low-absorption region, the absorption is also clearly lower. This is possible bleaching of the from difference frequency modes from longitudinal and transverse optical and acoustic phonons (LO, TO, LA and TA) present in the two frequency bands around 1.6 and 3.7 THz [204]. Considering the weakest applied field strength (red solid curve) the absorption feature around the 3.7 THz band (centered at 3.5 THz) seems to split up in three peaks, as also observed by Gallot *et al.* [39], and when the field is increased a broadening is first observed (black curve) and then a bleaching is seen (blue curve). To give an overview of this behavior, the transmission and absorption as function of field strength are shown in (d) as the red and the black curve, respectively. The two curves have been normalized to their respective maximum values. The transmission is calculated as the mean value obtained in the flat spectral range between 1.5 and 2.5 THz, while the absorption curve is the summarized absorption between 1.5 and 4 THz. The overall trend is that the transmission decreases slightly until 0.87E, after which it increases dramatically, which is likely to be the bleaching of the 1.6 THz absorption band. For the absorption in the 3.7 THz band the same overall trend is seen meaning that the absorption first increases, but drops significantly for the two measurements at the highest field strengths. This also means that the bleaching of the two absorption bands at 1.6 and 3.7 THz seems to occur at the same field strength.

The results of phonon bleaching achieved for ZnTe is even more convincing than for the organic materials, which may be expected since ZnTe is naturally a very nonlinear material. This also confirms that the focused THz pulses generated with this DSTMS source achieve field strengths high enough to see nonlinear responses from phonons.

6.1.5. Silicon

The final 1D spectroscopy experiment presented here is an investigation of the field-dependent transmission in Si. In contrast to the materials examined above, Si does not have any resonant absorption lines in the THz range. Instead the physical mechanism which can cause transmission changes in a THz-TDS experiment is impact ionization of electrons. Using intense THz pulses, impact ionization has been observed in direct and low-bandgap semiconductors of InSb [173] and GaAs [205]. In short, impact ionization is when a carrier in the conduction band is accelerated by the THz pulse and during a collision transfers its kinetic energy to another carrier in the valence

band, which is then excited to the conduction band. Recently Abebe Tarekegne and co-workers in the THz labs at DTU were the first to observe THz-induced impact ionization in silicon, by using the $LiNbO_3$ spectroscopy setup [206], which was also used for the lactose experiment described above in section 6.1.2. Because of the indirect bandgap in silicon, a very high field strength is necessary in order accelerate carriers sufficiently so that the impact ionization will occur [207, 208]. To achieve this, field enhancing antennas resonant within the bandwidth of the $LiNbO_3$ source were in that investigation fabricated on the silicon substrate. The impact ionization was then verified by the observation of a redshift of the antenna resonance frequency at high fields, which in turn was caused by the higher refractive index of the Si substrate in the regions with high concentration of carriers generated by impact ionization.

In the experiment presented here, a bare 525 µm thick high-resistivity silicon wafer has been inserted at the sample position of the DSTMS spectroscopy setup with ABCD detection, and transmission was measured as function of field strength, as described for the previous experiments. The results are shown in Fig. 6.8, where the left panel shows the time traces recorded for three different field strengths. The pulses at approximately 1 ps are the reference pulses while the weaker pulses just before 6 ps are the pulses transmitted through the silicon wafer. The right panel is the transmission for all field strengths calculated from the spectral amplitudes as the mean transmission between 1.5 and 3.5 THz. As mentioned previously, the Fresnel losses give that the amplitude transmission should be approximately 70 % for silicon using n = 3.42. This value is measured for the lowest incident field strength, but when increasing the field, the transmission graduately

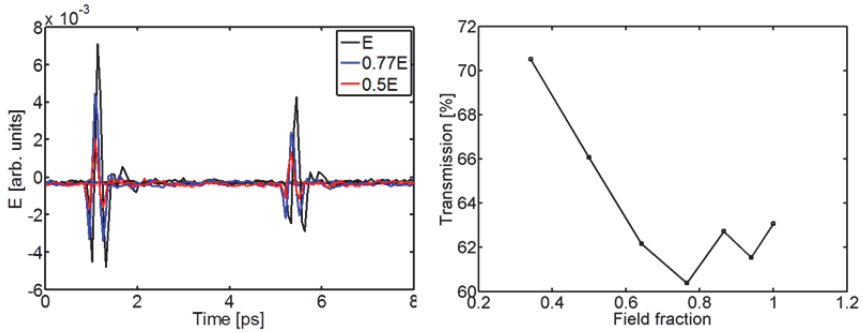

Fig. 6.8: Left: Time-domain traces with different field strength. Right: transmission through silicon as function of field strength.

decreases to below 61%. Above $0.8E_{max}$ the transmission saturates and there is even indication that it slightly increases again at the highest field strength. This decrease is a signature of the first experimental observation of THz-induced impact ionization using a free-space THz beam without further field enhancement techniques, and with the comparison to the results achieved in [206], this proves that the field strength achieved with the DSTMS source, even without field enhancing structures, is in the order of several MV/cm.

6.2. Two dimensional spectroscopy

2D IR spectroscopy is today a well-established method which both has been used to study molecular vibrations and electronic responses. Compared to 1D spectroscopy, the extra dimension in 2D spectroscopy adds the ability to directly map coupling between modes and to study line broadening mechanisms [185]. A typical 2D IR spectroscopy experiment is sketched in Fig. 6.9 where a non-collinear geometry of the incident beams is used. A sequence of two pulses are first exciting the sample, and then a third pulse probes the sample at a certain delay time later. Most often the aim is to detect four-wave mixing (FWM) signals including photon echoes, and using a non-collinear geometry, each signal can be spatially separated according to their k-vectors. This is illustrated in the photography shown in Fig. 6.9 (b) reprinted from Ref. [1], where all the signals marked with a grey ring originates from various FWM signals. The weak FWM signal can be detected using a local oscillator for heterodyne detection, which also provides the phase information. The excitation signal is simultaneously

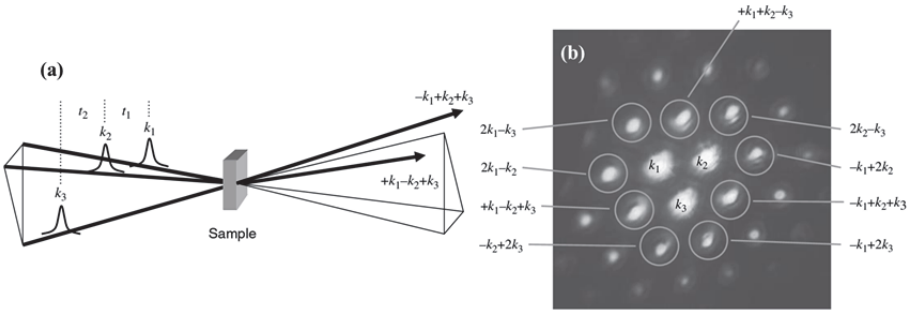

Fig. 6.9: (a) Typical non-collinear experimental geometry in a 2D IR spectroscopy experiment. (b) photography of contributions from combinations of k-vectors. Illustrations are reprinted from [1].

measured directly with a monochromator and a detector such as a mercury cadmium telluride (MCT) IR detector array. From this, a typical 2D map can be extracted showing the pump frequency on one axis and the probe frequency on the other. In such a spectrum the peaks lying on the diagonal corresponds to linear absorption features, while off-diagonal elements typically are nonlinear features such as anharmonic shifts or cross-peaks orginating from coupling between modes [1].

As shown previously in this thesis, non-collinear phase matching geometries as for example the tilted-pulse-front method for THz generation in $LiNbO_3$ significantly complicates an experimental setup, especially when more than one THz pulse is needed. However, it has been shown that if the electric field can be measured directly, and thus preserving the phase information, 2D spectroscopy can be performed in a collinear geometry [4]. While the non-collinear method often suffers from low signal due to phase mismatch, the collinear geometry allows for the pulses to interact over a longer distance depending on the thickness of the sample, and four-wave mixing signals can be observed just with two pulses instead of three. The concept of collinear 2D spectroscopy is explained in Fig. 6.10 (reprinted from [4]). First, two pulses are considered (A and B) in a non-collinear geometry as shown in the left panel. In the same way as shown in Fig. 6.9, the nonlinear signals will be spatially separated according to their k-vectors. Here, the red arrows are pump-probe signals, the dashed arrows are FWM signals, and dotted arrows

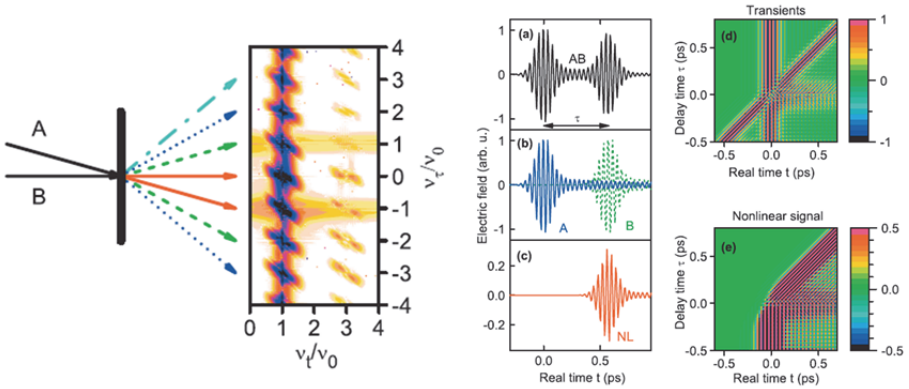

Fig. 6.10: (left) correspondence between the nonlinear elements in the usual k-vector space and the frequency map. (a) and (b) show simulated AB, A and B traces, where (c) is the resulting nonlinear trace when (b) is subtracted from (a). (d) is the time domain map of the AB signal and (e) is for the nonlinear signal. Figures are reprinted from [4].

are six-wave mixing. In a collinear experiment, different k-vectors can be separated based their respective frequencies. Next to the arrows is the corresponding two-dimensional frequency map from a phase-resolved, collinear experiment, where it is seen that the signals appear at different frequency positions according to the nonlinear process responsible for the signal. For instance, the FWM signal at $2k_A$-k_B is found at $(\nu_t/\nu_0 = 1, \nu_\tau/\nu_0 = 1)$. Having a collinear geometry, the obvious challenge is how to separate the nonlinear signal from the much stronger linear signals, especially in the case where spectrally broadband pulses such as the THz pulses used here, excite a sample. For signal discrimination, such broadband signals might even be troublesome to separate in a non-collinear case. Nevertheless, the ability of measure the electric field of the THz pulses with EO sampling or ABCD, makes it possible to directly detect the nonlinear signals. The nonlinear signal measured from the two pulses measured in real time t is

$$S_{NL}(t,\tau) = E_{AB}(t,\tau) - E_A(t) - E_B(t,\tau) \tag{6.8}$$

where τ is the delay time between the two pulses. Fig. 6.10 (a) (reprinted

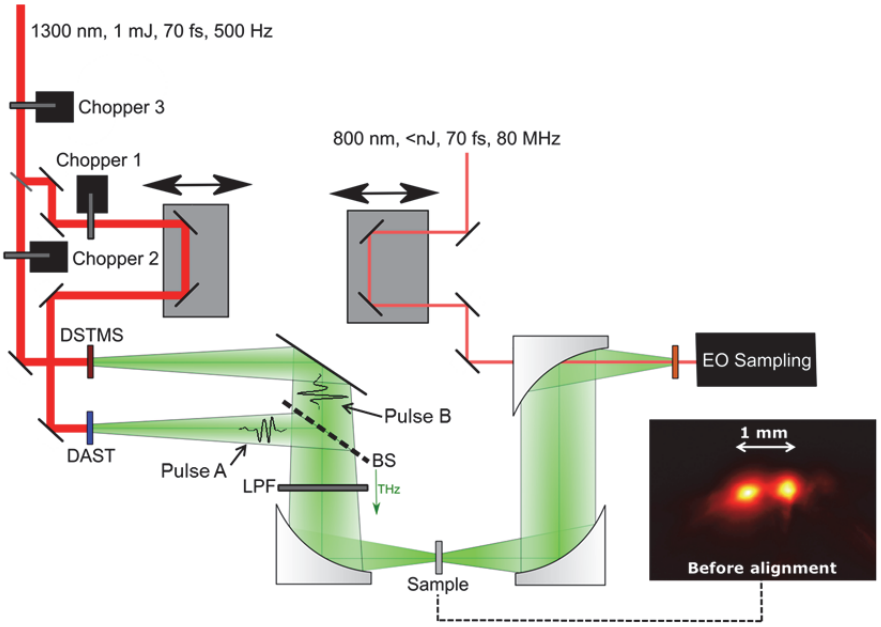

Fig. 6.11: Experimental setup for 2D spectroscopy.

from [4]) illustrates the AB trace where both pulses are incident on the sample, and (b) shows the individual A and B signals. In agreement with the equation above, the subtraction of the signals in (b) from (a) gives the nonlinear signal in (c). For a variable delay time where the pulse B is scanned across the pulse A, the AB signal will appear as a 2D time-domain map, where the horizontal axis shows the real time t and the vertical axis is the delay time τ as shown in (d). This map represents both the linear and nonlinear signal, but the nonlinear signal can be extracted using the above relation. By Fourier transforming the nonlinear signal map, the nonlinear contributions can be sorted according to their frequencies, and thereby the physical mechanism responsible for each signal can be revealed.

In the following section an experimental scheme for recording the nonlinear signal in a collinear 2D THz spectroscopy experiment will be presented. Here, nonlinear signals have successfully been detected in a sucrose crystal, most significantly when the crystal was cooled to below 10 K. These data are analyzed and discussed in section 6.2.2. For the reference and as a critical sanity check of the rather complicated experimental setup, it is shown that no nonlinearities are observed when no sample was in the beam line. Additionally, a sample of glutamic acid, where nonlinearities could be expected, did not show any nonlinearities using the same experiment and data analysis, and can therefore also be considered as a linear reference measurement. Both of the two reference studies are presented in section 6.2.3.

6.2.1. Experimental setup and detection scheme

The experimental setup used for 2D spectroscopy is shown in Fig. 6.11. The

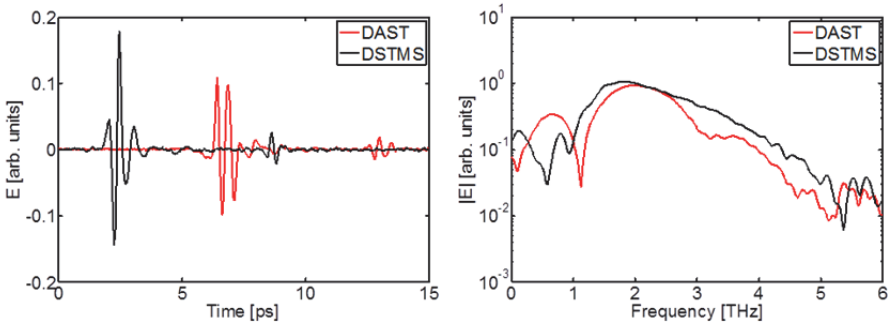

Fig. 6.12: Pulses (left) and spectra (right) generated from DAST and DSTMS in the 2D configuration.

incident beam with pulse energies of 1 mJ and a center wavelength of 1300 nm is split in two beams with a 50/50 beam splitter. The reflected beam (A) is sent through a delay stage before reaching the DAST THz emitter, while the transmitted beam (B) was sent directly to the DSTMS THz emitter. The two THz beams were overlapped on a silicon beamsplitter, and the alignment of the beam overlap was carefully done using the NEC THz camera. The silicon beamsplitter is possibly affected by impact ionization, however, since this is a stationary component this is not expect to influence the experiment. The inset in Fig. 6.11 shows the two focused beams displaced spatially before alignment. In the appropriate alignment the beams were perfectly overlapped. The off-axis parabolic mirror focusing the beam onto the sample, collimating the beam and refocusing onto the detection crystal have a focal length of 2", 4" and 2", respectively. The beams are detected with EO sampling using a 300 μm thick GaP crystal. It has been found that the GaP detection is capable of resolving the full DSTMS bandwidth similar to what was detected with ABCD. The higher sensitivity offered by the EO sampling technique is crucial for the 2D spectroscopy experiment, where the targeted nonlinear signals are expected to be much smaller than the transmitted signals detected in the 1D spectroscopy experiments. The detection beam is sampled with a fraction of the seed oscillator beam (not the amplified laser pulses). The advantage of this is that

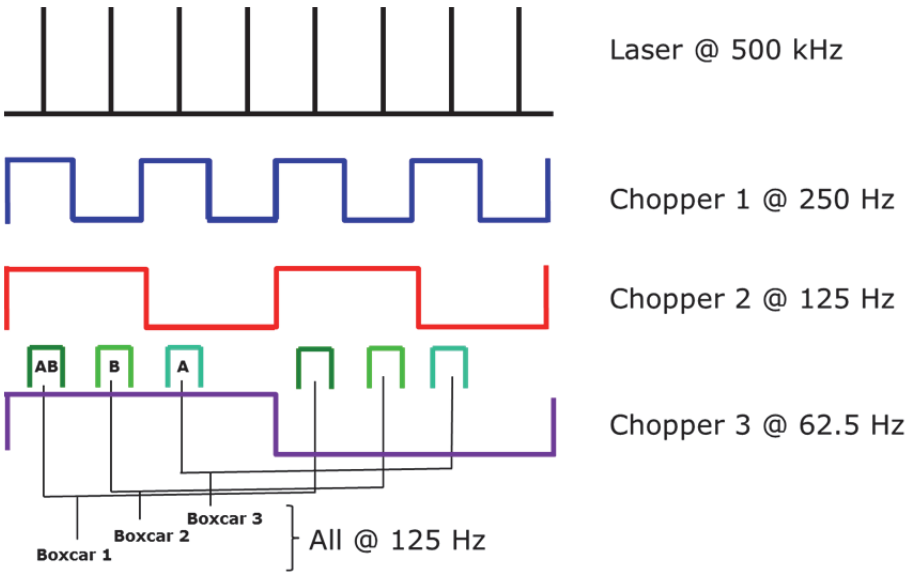

Fig. 6.13: Chopper scheme for 2D spectroscopy.

in this case no beam splitter between the amplifier and OPA is needed, giving a significantly higher output from the OPA. Since the repetition rate of the detection beam now is much higher (80 MHz) than of the amplified laser beam (maximum 1 kHz), it is necessary to select the correct detection pulse, for example by using a boxcar integrator. Three synchronized choppers are used in the 2D setup: one in each of the two generation arms allowing for simultaneous detection A, B and AB signal in Eq. (6.8) (Chopper 1 and Chopper 2), and one before the beam is split, allowing for the lock-in detection (Chopper 3). It has been mentioned previously that the repetition rate should be around 100 Hz to avoid damage on the organic crystals of DAST and DSTMS, but since both the choppers and the beam splitter reduce the power incident on each crystal, it was possible to set the laser repetition rate to 500 Hz without damaging the crystals. Inspired by [4] the detection scheme is shown in Fig. 6.13. Having Chopper 1 at first subharmonic of the laser beam (250 Hz) and Chopper 2 at the third subharmonic (125 Hz), the correct pulse sequence for detecting the nonlinear signal is achieved: first pulse A and B is present at the sample ("AB"), secondly only pulse B is present ("B") and thirdly only pulse A is present (A). At the fourth slot in this sequence both beams are blocked. Chopper 3 is set to the seventh subharmonic of the laser beam (62.5 Hz) in order to perform lock-in detection on this sequence. In order distinguish the signals of AB, A and B in the pulse sequence within the cycle of Chopper 3, three boxcars are used, each connected to a lockin amplifier. Each boxcar receives a 125 Hz trigger signal from a delay generator, where trigger for signal B is delayed by 2 ms from signal AB, and signal A is delayed further 2 ms. The three boxcar windows were set to be as identical as possible, each with a width of approximately 9 ns. With this three signals AB, B and A are each read simultaneously from three lock-in amplifiers while the delay stage of the detection beam is scanned. The full data acquisition sequence is controlled by a Matlab program.

6.2.2. Sucrose

A 2D spectroscopy experiment has been performed on the same sucrose crystal which was also studied in the 1D experiment described in section 6.1.3. The 1D absorption spectra showed some absorption peaks which seemed to be broadened or to consist of several peaks, especially the two features located at 1.8 THz and 2.7 THz. It has been shown that cryogenic cooling prevents the thermal broadening of the absorption peaks in sucrose

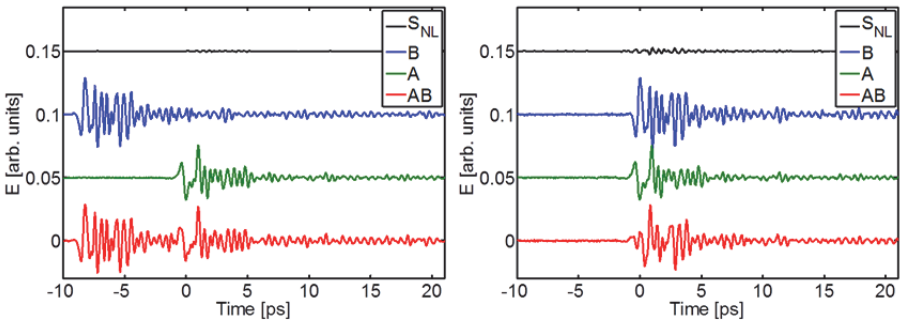

Fig. 6.14: Time traces for the AB (red), A (green), B (blue) and nonlinear (black) signals at the first delay stage position where $\tau = -8$ ps (left) and where the A and B pulse overlap i.e. $\tau \approx 0$ ps (right). For clarity, the traces are offset vertically.

[36], and for this reason the sample was mounted in a helium cryostat allowing for sample cooling down to below 4 K. The first results presented here are measured at 10 K, while experiments performed at 150 K and 300 K are presented subsequently. The 2D experiments are performed with the setup shown in Fig. 6.11 and using the chopper- and boxcar scheme seen in Fig. 6.13. The delay stage controlling the delay of the DSTMS generated THz pulse (pulse B) is scanned in steps of 200 fs, and at each step the detection stage is scanned in steps of 50 fs. The number of steps i.e. the length of the two time axes depends on the sample. For cryogenically cooled samples with phonon resonances within the bandwidth of the THz sources it was necessary to scan both stages approximately 20 ps, since the sharpened phonon lines lead to oscillations in the time-domain trace for more than 20 ps after original THz peak. For each delay step the time traces are averaged over two scans in order to reduce noise. The time-domain traces recorded at two selected delay times are shown in Fig. 6.14. Here the AB signal is shown as the red curve, A is the green curve, B is the blue curve, and the calculated nonlinear signal is the black curve. The traces in the left panel are recorded the first delay position (-8 ps), where only the tail of the B pulse overlaps with the A pulse. The nonlinear signal is absent over most of the trace except from a minor modulation where the amplitude of A is largest and is overlapping with the B pulse. It should be noted that for this case where sucrose is cooled to 10 K both the A and B time traces oscillate over the entire time window. Consequently, the two pulses are here much more difficult to separate than the pulses measured without the sample (see Fig. 6.12 (left)).

The right figure shows the traces at a delay time close to zero where the nonlinear signal is significantly larger. With the scan parameters given here, the time taken to record a full 2D map was between 22 and 30 hours, over which period the full laser system and experimental conditions must remain stable. The recorded 2D time-domain maps recorded for sucrose cooled to 10 K are shown in Fig. 6.15, where (a) is signal A (the DAST generated THz pulse), (b) is signal B (the DSTMS generated THz pulse), (c) is signal AB (both the DAST and DSTMS THz pulses), and (d) is the nonlinear signal extracted by using equation (6.8). The origin of the map has been defined approximately where pulse B crosses pulse A. The A signal in (a) appears as vertical lines since the beam line is fixed, i.e. the timing between this pulse and the detection pulse is constant. The delay of signal B expresses itself as the diagonal lines in (b). In (a) weak, vertical lines are observed even after 20 ps on the real time axis, which are the oscillations of the absorption lines. Considering the room temperature recorded 1D spectrum for sucrose (Fig. 6.4), these oscillations fully decayed after ~8 ps, indicating that the absorption peaks as expected are much sharper for the cold sample. The

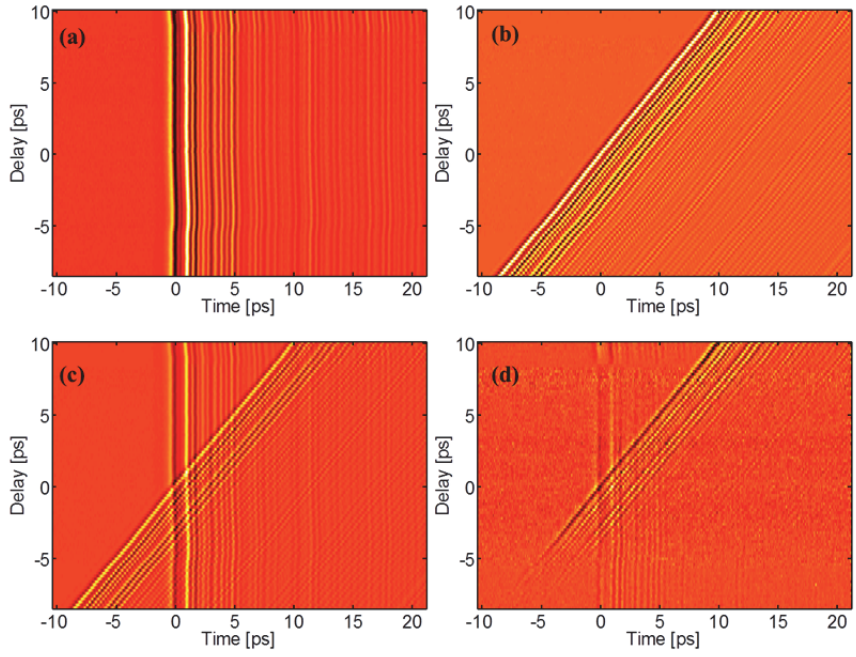

Fig. 6.15: Signals measured for sucrose at 10K where (a) is Signal A, (b) is Signal B, (c) is Signal AB and (d) is the nonlinear signal.

slight shift in the timing between the THz pulses and the detection pulse over the time that the experiment was performed is expected to be due to thermal effects in generation crystals and the regenerative amplifier (Spitfire Ace) affecting the length of the generation beam path.This is most evident as the shift in the vertical lines in (a) the delay times of -5 ps and 10 ps, but since the three time traces of the A, B and AB signals are recorded simultaneously, this is not critical for obtaining the nonlinear signal. In (d) it is seen that the nonlinear signal appear mostly on the diagonal in the same direction as pulse B. To show clearest representation of all signals the colorbar has been scaled to the peak amplitudes of each signal. The maximum amplitude of the nonlinear signal is approximately 14 % of that of the AB signal. For this reason the noise floor is also much more visible in the nonlinear map. The increased noise appearing between the delay time of -5 and 7 ps are mostly due to stray light in the laboratory. The fact the nonlinear signal arises already at negative values of the real time is somewhat counter intuitive, since causality should be so that the nonlinearity only appears when there pulse A and B overlap in time. However, dispersion

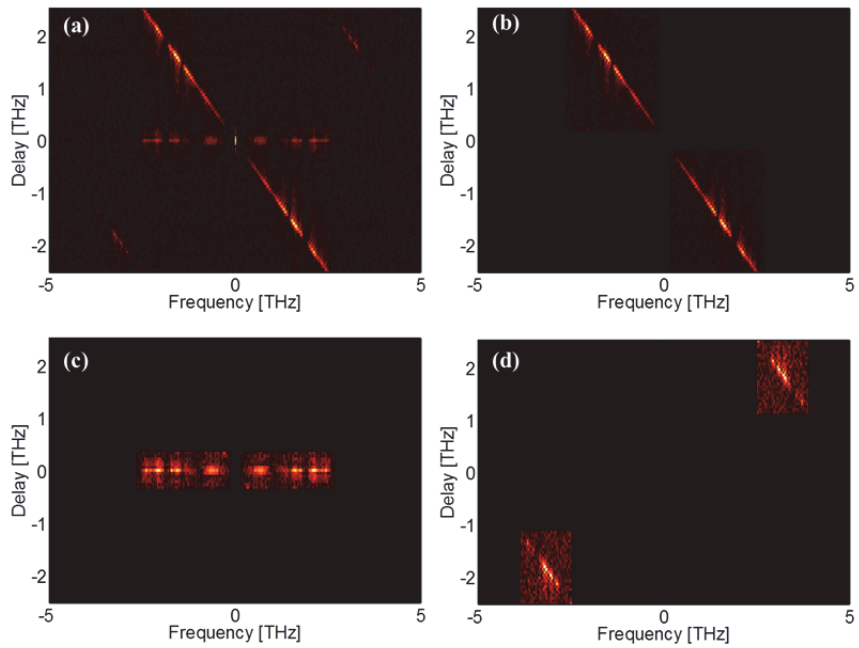

Fig. 6.16: Amplitude maps of the Fourier transformed nonlinear signal where (a) is the full map, (b) is pump-probe signal 1, (c) is pump-probe signal 2 and (d) is the residual signal.

effects inside the sample complicate this causality interpretation since the pulse delay in the experimental case is measured in the GaP detection crystal, and thus after the pulses have propagated and dispersed in the sample. Future studies will address this relation to causality in more detail.

The absolute value of the Fourier transformed nonlinear signal is shown in Fig. 6.16 (a). Overall, three types of signals, separated in (b)-(d), are seen: a diagonal element at where $\nu_t = -\nu_\tau$ shown in Fig. 6.16 (b), a horizontal element at $\nu_\tau = 0$ shown in Fig. 6.16 (c) and a residual signal where $\nu_t = \nu_\tau$ (d), which is a folding of the signal in Fig. 6.16 (b) since the Nyquist criterion of the delay axis resolution (200 fs) only allows for a frequency sampling up to ± 2.5 THz. The diagonal element corresponds to the nonlinear A-pump/B-probe signal i.e. the superposition of the signals in Fig. 6.16 (b) and (d), and oppositely, Fig. 6.16 (c) is the nonlinear B-pump/A-probe signal. In the following these two pump/probe signals are analyzed separately. The superposition of the two elements in the A-pump/B-probe signal is shown in Fig. 6.17 (a), and the real part of the inverse Fourier

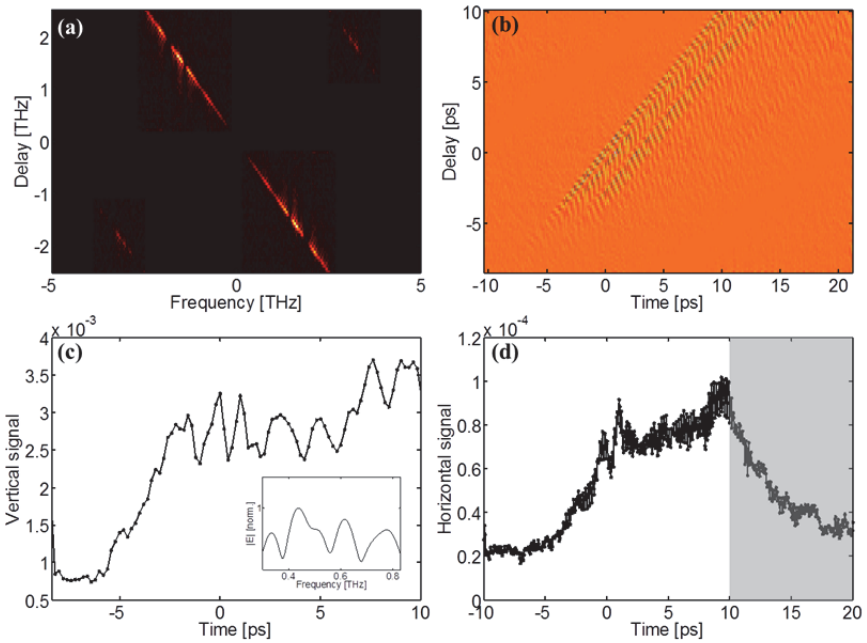

Fig. 6.17: A-Pump/B-probe signal measured for sucrose at 10 K in (a) frequency domain and (b) time domain. In (c) is shown the vertical projection of (b) and (d) is the horizontal projection.

transform of this back to the time-domain is shown in Fig. 6.17 (b). The signal appears as a diagonal element similar to the time domain map of the B pulse. It should be noted that the phase fronts aligned with pulse B is an indication that coherence information is preserved in the nonlinear signal. This will be investigated later in section 6.2.2.1. To investigate the development of this pump-probe signal during the scan, the projections of the absolute value of the signals in the vertical and horizontal direction are calculated, as shown in Fig. 6.17 (c) and Fig. 6.17 (d). The vertical projection is most important, since it precisely tells the response of the pump-probe signal when the pump-probe delay is changed. As expected the signal arises when the delay time approaches 0 ps from negative time values, and does not decay within the recorded delay time, on the contrary the signal seems to increase even further after 7 ps. The oscillating features seen from 3 to 10 ps could originate from mode beating of the absorption features. To determine the frequencies of these beatings, the insert shows the Fourier transform of the vertical projection from -3 to 10 ps. Three main peaks at 0.44, 0.62 and 0.77 THz are seen, and the first peak is broadened.

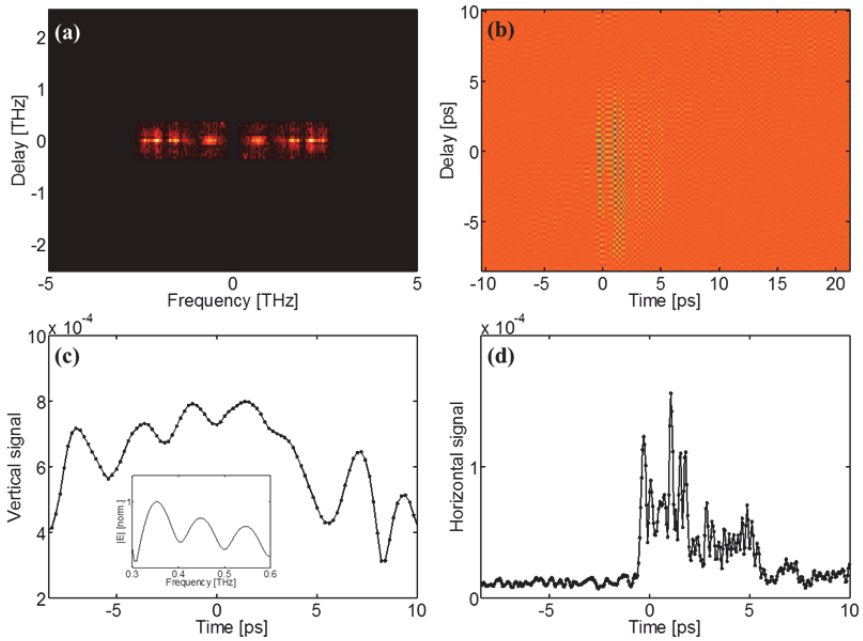

Fig. 6.18 B-Pump/A-probe signal in (a) frequency domain and (b) time domain. In (c) is shown the vertical projection of (b) and (d) is the horizontal projection.

Considering the 1D absorption spectrum in Fig. 6.6, it is likely that these originate from a beating between the 1.4 THz resonance and the high-frequency part of the 1.8 THz resonance, the 2.7 THz phonon and the 3.3 THz phonon, and frequencies within the 1.8 THz peak and the 2.7 THz peak, respectively. The horizontal projection in Fig. 6.17 (d) shows in the same way as the vertical projection that the signal rises towards the real time value of 0 ps, while it increases further afterwards. The decay after 10 ps is due to the end of the delay stage scan and thereby not representative of an actual decay of the signal. In the same way, the real valued inverse Fourier transform of the frequency filtered B-pump/A-probe signal in Fig. 6.18 (a) is shown in Fig. 6.18 (b). As expected it appears as vertical lines, which again is analyzed by the vertical and horizontal projections in Fig. 6.18 (c) and (d). Here, the vertical projection increases slightly up to 2 ps, after which it decays again. The oscillations appear much slower than before, and in the inset it is seen that the dominating beat frequency is at 0.36 THz. This is likely to be beating between the 1.4 and the low-frequency part of the 1.8 THz absorption peak. For this case where the signal decays within the

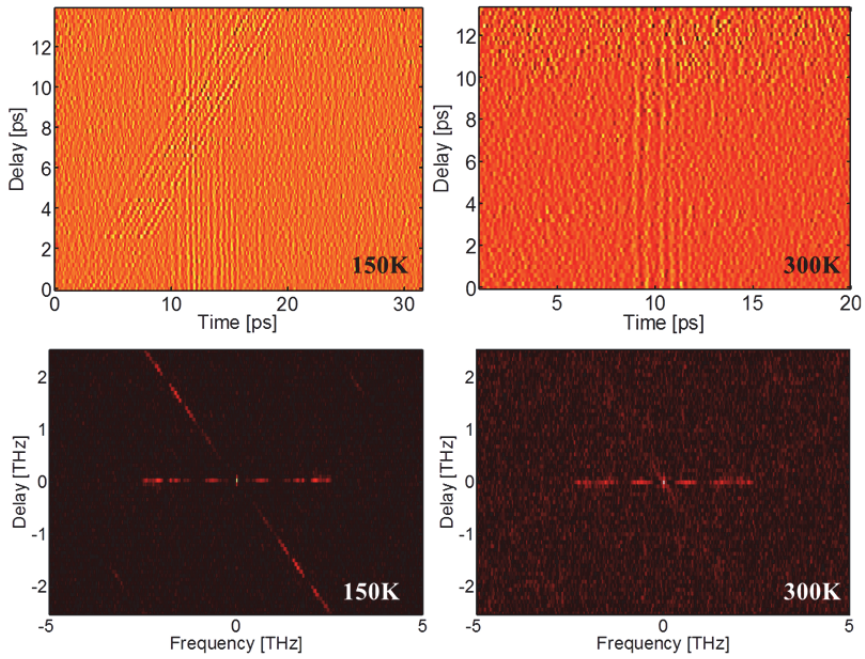

Fig. 6.19: The top row is the non-linear signal measured for sucrose at 150 K and 300 K. The bottom row shows the amplitude maps of the nonlinear signals above.

recorded map, the horizontal projection is representative for real time duration of the signal. From Fig. 6.18 (d) it is seen that the signal for certain delays oscillates for more than 5 ps.

The 2D experiment on sucrose presented above has also been performed at higher temperatures of 150 and 300 K. The results in the form of nonlinear maps are shown in Fig. 6.19, where the top row shows the nonlinear maps in the time domain, while the bottom row are the frequency maps. In both cases, the nonlinear signal in time domain is much harder to identify than for the experiment where the sucrose crystal was cooled to 10 K. The time domain map at 150 K shows weak traces of a vertical signal (B-pump/A-probe) together with a diagonal signal (A-pump/B-probe), which appears similar in strength in contrast to the 10 K map where the A-pump/B-probe was dominating. Considering the Fourier transformed amplitude maps, both types of pump-probe elements appear as the horizontal element and diagonal element at 150 K, while only the horizontal element from the B-pump/A-probe signal appears is present at 300 K. In the following each element in the

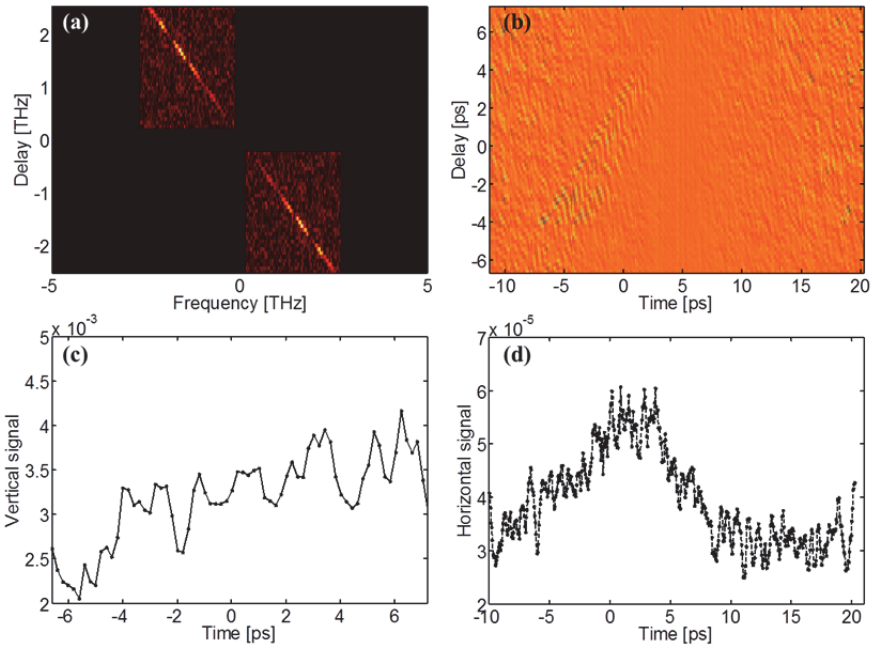

Fig. 6.20: A-Pump/B-probe signal measured for sucrose at 150 K in (a) frequency domain and (b) time domain. In (c) the vertical projection of (b) and (d) the horizontal projection is shown.

frequency domain maps are analyzed in the same way as above for the 10K experiment.

The diagonal element corresponding to the A-pump/B-probe signal measured at 150 K is filtered as shown in Fig. 6.20 (a) and transformed back to the time domain, as shown in (b). The diagonal signal is only weakly present, while most of the map is dominated by noise. The vertical projection of the absolute value of (b) is shown in (c), where a trend similar to what was observed for 10 K is seen, however, the SNR is poor and for this reason it was not possible to resolve any beat frequencies in the same way as for the 10 K data. Considering the absolute value of (b) projected in the horizontal direction shown in (d), the signal increases almost linearly for negative delay times and maximizes around t=0, and remains constant for a few ps after which it decreases again. In contrast to the measurements performed at 10 K, the nonlinear signal decays fully within the delay time recorded in the experiment. Again, it is seen that the SNR is much smaller here than for the equivalent projection calculated in the 10 K experiment.

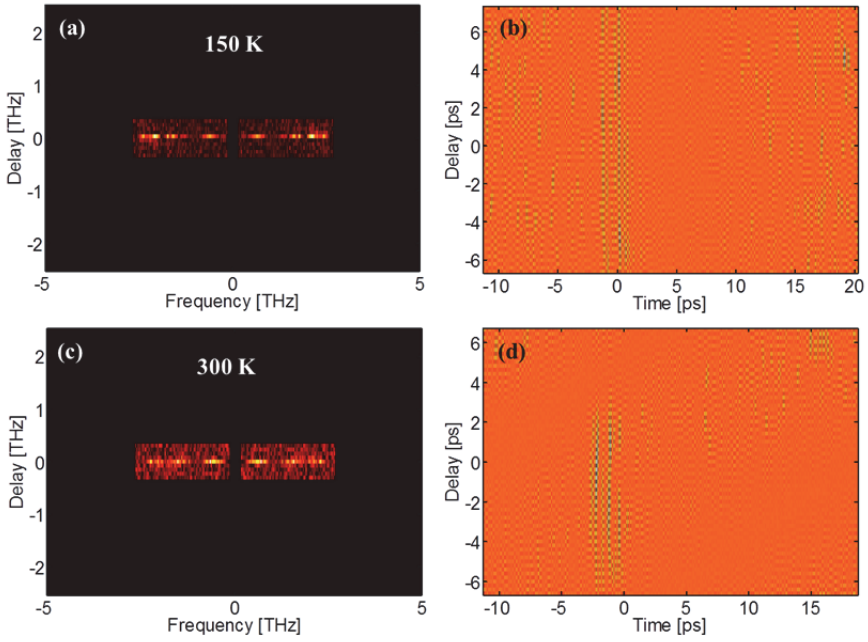

Fig. 6.21: B-Pump/A-probe measured for sucrose at 150 K (a) in frequency domain and (b) time domain. Similarly, at 300 K (c) is the B-Pump/A-probe signal in frequency domain and (d) is in time domain.

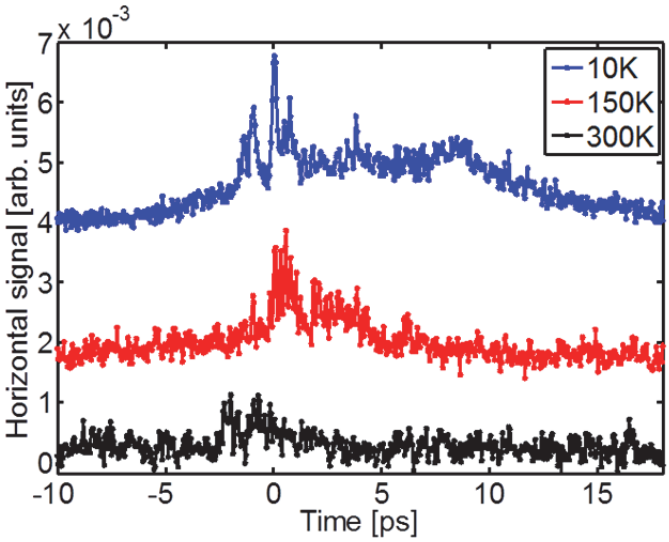

Fig. 6.22: Horizontal projections of the nonlinear signals at 10, 150 and 300 K. All signals are normalized to the integrated signal

For 150 K and 300 K the filtered horizontal elements in the 2D frequency maps are shown in in the left panel of Fig. 6.21. From these representations the signal recorded at 300 K appears even weaker than the signal recorded at 150 K. The right panel shows the corresponding real part of the inverse Fourier transforms. Both time domain maps are highly affected by noise and due to the low SNR the projections are left out for these measurements. However, some oscillation between positive and negative field values along the vertical signal lines is observed for both maps, which is likely to be another indication of mode beating.

For a direct comparison of the nonlinear signal measured at the three temperatures of 10, 150 and 300 K, the horizontal projections of the absolute value of the measured time domain nonlinear signal without any frequency filtering are compared in Fig. 6.22. For clear representation, the projections of the nonlinear signal at 150 and 10 K are offset on the signal axis. From this it is clearly seen that the nonlinear signal is higher when the temperature is low. At the same time it is seen that the decay time of the nonlinear signal i.e. the real time duration of the signals in Fig. 6.22 is increasing when the temperature is decreased; for 300 K the duration is a few ps, for 150 K approximately 5 ps, and for 10 K at least 10 ps since the decay was not measured within the delay time in this experiment.

6.2.2.1. Coherent response

Previous studies where nonlinear signals have been measured with similar collinear 2D schemes have considered semiconductor-based systems [4, 186, 187]. In all of those studies it has been observed that for the pump-probe signals, the phase of the nonlinear signal reproduces the phase of the probe beam (i.e. the phase is independent of the pump-probe delay) since the phase information from pump beam is lost due to incoherent processes such as impact ionization. Only the FWM signal have shown conservation of the pump coherence, which in experiment is observed as lines of constant phase pointing along the downward diagonal in the 2D time-domain map, indicating a phase dependence on both the A and B pulse [186]. In this study concerning molecular vibrations rather than electron dynamics, it has been observed that the phase of the detected nonlinear signal does not necessarily equal that of the probe pulse, but depends on the pump pulse. This was most significant for the A-pump/B-probe element in the experiment where the sample was cooled to 10 K, so for this reason this signal is studied further in the following. The left Panel in Fig. 6.23 shows the real part of this signal for positive pump frequencies. Some broadening of the diagonal elements is observed approximately at 1.7 and 2.1 THz, which is likely to be related to dynamics of near-by phonon resonances. The right panel shows the horizontal projection of the absolute value indicated as black, connected squares. This represents the nonlinear transmission spectrum, and for comparison the absorption spectrum measured with 1D spectroscopy is shown as the red curve.

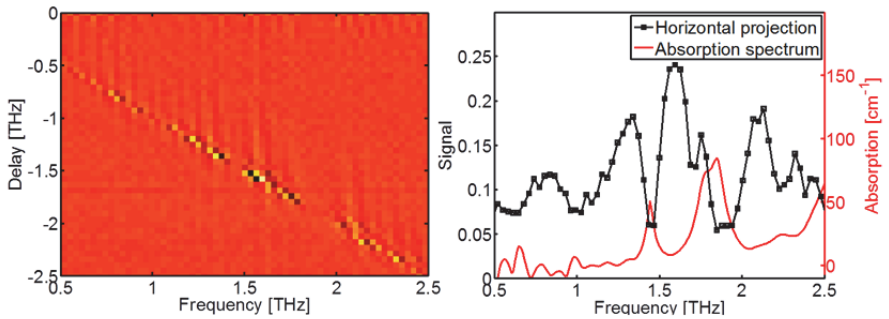

Fig. 6.23: Real part of the A-pump/B-probe signal for positive frequencies (left) and the absolute values horizontal projection (black squares) shown together with the 1D absorption section as the red curve (right).

From the two curves it is seen that there is a good agreement between the absorption features measured in the two experiments. Remarkable is that the absorption peaks at 1.4 THz seems to overlap almost perfectly, while the feature at 1.7 THz is clearly split into two peaks in the horizontal projections. A few other minor absorption features are seen in this frequency range from 0.5 to 2.5 THz. However, the two features around 1.4 and 1.7 THz are dominating.

In the frequency map of the absolute value of the A-pump/B-probe signal, weak bands away from the diagonal line ($\nu_\tau = -\nu_t$) are seen on the redshifted side of the delay axis frequencies close to the two significant phonon resonances discussed above. In Fig. 6.24 the signal has been frequency filtered in two different ways; (a) includes only a narrow band of frequencies around the 1.4 THz resonance (seen as the dark band in the middle of the diagonal element here), and (c) includes the lowest frequencies below 1 THz where no resonance is seen in the elements. Frequency filtering in this manner enables an insight into the temporal dynamics of these specific

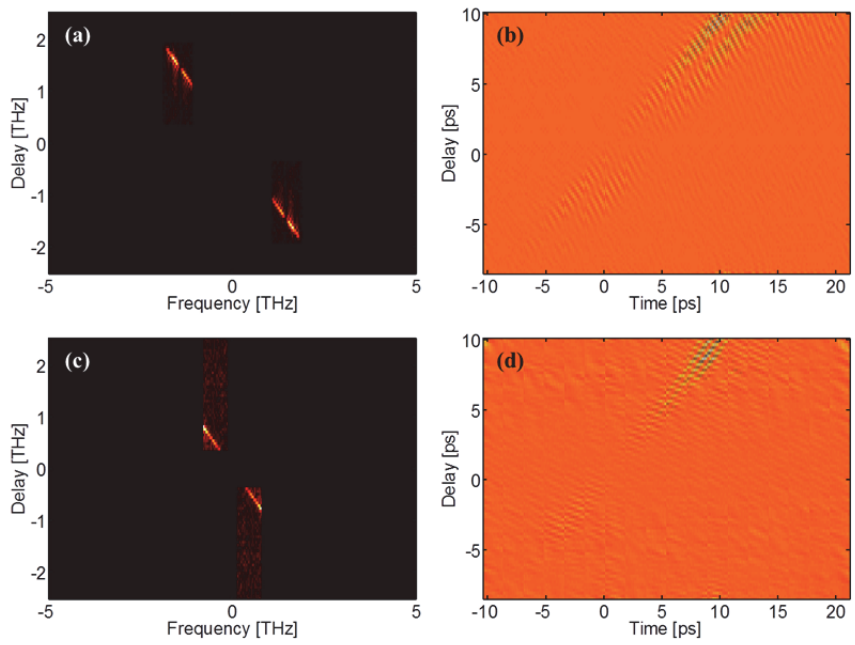

Fig. 6.24: Filtered A-pump/B-probe signals in the frequency spans from (a) 0.8 to 1.8 THz and (c) 0.1 to 0.8 THz. (b) and (d) are the real value of the Fourier transform of (a) and (c), respectively.

frequency regions. Fig. 6.24 (b) and (d) are the corresponding time-domain signals calculated from the inverse Fourier transform of the filtered frequency maps in (a) and (c). From this it is seen that the phase fronts in (d) mostly seems to reproduce the phase of the probe pulse, while (b) has a significantly different phase where the lines are pointing towards the downward diagonal, approximately perpendicular to the propagation direction of the signal. This is interpreted as a superposed phase front of the pump and probe pulse containing coherence information about the molecular vibrations, and the experimental data directly shows that coherence is maintained in the nonlinear signal over several picoseconds, in contrast to previous studies of electronic dynamics. This emphasizes the advantage of instantaneously excited systems such as phonons offering the possibility to maintain the information of coherence on a long time scale, in the case here more than 10 ps, while nonlinear pump-probe signals from carriers immediately lose their phase information.

6.2.3. Measurements without nonlinearities

The 2D experiment described in this section is a method which directly targets nonlinear effects in a sample, which in the previous subsection was a sucrose single crystal. At the same time the method used for detection of the THz pulses is also relying on nonlinearities in an EO crystal, and therefore it is critically necessary to ensure that the measured nonlinearities originate from the sample and not from the detection crystal or other experimental artifacts. For this reason a reference measurement without a sample has been recorded. The typical experimental routine is to insert a silicon wafer in the collimated THz beam path after the sample if the transmission of the sample is high (greater than 70 % of the electric field) in order to attenuate the THz beam to avoid nonlinear detection effects such as over-rotation (explained in Chapter 3) or intrinsic higher-order nonlinearities in the crystals at such high field strengths [209]. Such nonlinearities would lead to the possibility that the nonlinear signal obtained by the AB-A-B subtraction would not necessarily originate from the sample, but from nonlinearities in the detection system. For this reference measurement, no silicon wafer other than the beam splitter combining the two THz beams was implemented, so with the highest possible THz fields incident on the detection crystal, this is representing a “worst-case-scenario” of nonlinear effects originating from the detection crystal (300 μm GaP). The nonlinear signal measured in this scan is shown in Fig. 6.25, where some weak residual traces are seen,

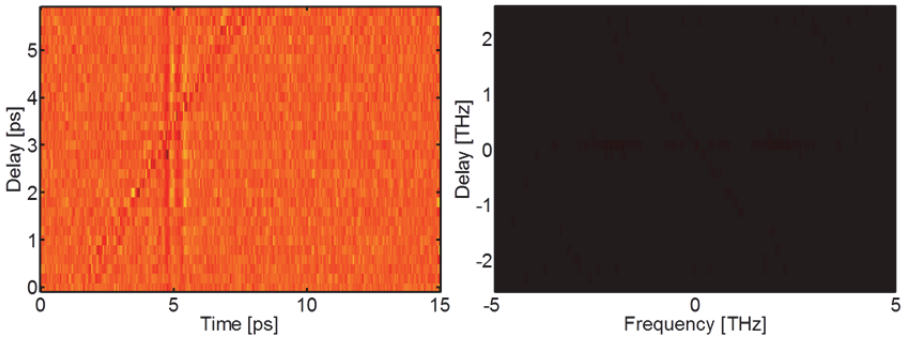

Fig. 6.25: Nonlinear signal measured in air (left) and the corresponding amplitude map of the Fourier transformed nonlinear signal (right). Both maps have the same color range as shown for sucrose measured at 10K.

however, the signal appears almost constant at all times and is located at the same time positions as the AB signal. This signal map represents the accuracy of the detection setup and the subsequent analysis. The residual signal is believed to mainly originate from minor artifacts caused by the uncertainty on the three boxcar windows used in the detection scheme since the tree boxcar windows might not be 100 % identical. The maximum amplitude of the nonlinear signal measured in this scan is approximately six times smaller than what it is for sucrose at 10 K, which is at the same level of the noise floor of the sucrose measurements when the projections are considered. The right panel in Fig. 6.25 shows the amplitude of the Fourier transformed nonlinear signal on the same color scale as used for sucrose at 10 K shown in Fig. 6.16 (a), indicating that the nonlinearities observed in sucrose actually originate from the sample, and not from any systematic errors in the setup. Only very weak features (hardly visible in Fig. 1.25(b)) are seen mostly along the horizontal line for $\tau = 0$. This would be insignificant in the sucrose measurements discussed in the previous section. Again it should be emphasized that this reference measurement represents a worst-case scenario with respect to any detection nonlinearities. The detected signal amplitudes in the sucrose experiment were significantly smaller than in the air reference measurement, and thus any detection nonlinearities should be significantly reduced.

As another reference measurement, a sample where contrary to expectations, no nonlinear signal was observed, is finally presented here. Glutamic acid is an amino acid with two sharp absorption features at 1.2 and 2.0 THz [210, 211], which are within the spectral region covered with the DSTMS and

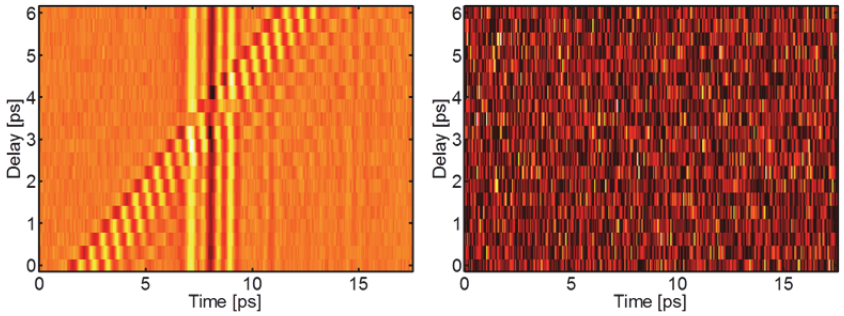

Fig. 6.26: The AB signal measured for Glutamic acid (left) together with the measured nonlinear signal (right).

DAST crystals and thereby an obvious candidate for a 2D study. Here, a pellet of pure L-glutamic acid has been investigated in a 2D experiment, where the resulting AB signal is shown in the left Panel of Fig. 6.26, and the nonlinear signal extracted from this experiment is shown in the right panel. It is seen that even though the transmission through the pellet is high enough to successfully measure the AB trace with a decent SNR, and similar for the A and B traces (not shown here), the nonlinear signal is absent. Despite the author's disappointment at the time when this experiment was performed, the absent nonlinear signal from another crystalline material validates and reinforces the impact of the nonlinear signal measured from the sucrose crystal, both at room temperature and particularly when cooled down to 10 K. This possibly also indicates that nonlinear signals measured from crystalline materials are most ideally measured from single crystals rather than pellets of polycrystalline mixtures.

6.3. Conclusion and outlook

In this chapter results of nonlinear spectroscopy have been presented. The first part concerned 1D spectroscopy where a single beam with intense THz pulses was used to investigate samples. First, lactose was investigated with peak field strengths up to 400 kV/cm achieved with a $LiNbO_3$ setup, where only minor indications of bleaching of the 0.55 THz phonon were seen. Secondly, sucrose was investigated in the DSTMS setup with peak field strengths of several MV/cm, where a stronger indication of phonon bleaching was observed between 1 and 4 THz. Most significant was the bleaching of the 1.4 THz phonon, which is in agreement with what was observed in the field-dependent MD simulations performed with CASTEP.

Additionally to the experiments performed on the organic crystals of lactose and sucrose, field-dependent measurements were also performed on the semiconductors ZnTe and silicon. Here, it was observed that the transmission increased for the highest field strengths due to phonon bleaching in ZnTe and impact ionization in silicon. The 1D measurements in ZnTe indicate that a full 2D investigation of the nonlinear phonon dynamics in this material could be very interesting, as the phonon modes below the fundamental TO phonon are combination bands, and thus represent a different type of vibrational dynamics than sucrose, where all observed vibrational modes are fundamental phonons.

2D spectroscopy has been performed using two THz sources of DAST and DSTMS and an EO sampling detection scheme based on three choppers and three boxcars for simultaneous detection of the A, B and AB signal. Based on this scheme, the first observation of nonlinear vibrational dynamics in the low THz range has been possible. Nonlinear pump-probe signals in sucrose have been measured at temperatures of 10, 150 and 300 K and as expected the nonlinear signal is strongest at low temperature. It was observed that beat frequencies extracted from the pump-probe signal match well with the calculated beat frequencies between the fundamental 1.4, 1.8, 2.7 and 3.3 THz modes, so such beats are expected to be responsible for the measured beating pattern. In contrast to previous 2D studies performed on semiconductors by other groups with low-frequency pulses approaching the THz range where the coherence was not preserved in the pump-probe signal due to incoherent carrier processes, coherent pump-probe signals were detected in frequency ranges containing molecular vibrations. The validity of the nonlinear signal measured from sucrose was verified by a 2D scan without a sample, which only showed an insignificant nonlinear signal. This was further supported by the 2D experiment performed on glutamic acid, which, despite being an obvious candidate with two resonances at 1.2 and 2 THz, did not show any nonlinearities from the measurement.

2D THz spectroscopy results presented here was performed for the first time at DTU in February 2015, so with the short time frame there are obviously a number of developments and improvements to be done in future experiments. In the sucrose measurement no off-diagonal FWM signal has been observed so far. The delay-time resolution limiting the frequency range to 2.5 THz is likely to be a limiting factor for this. Future experiments will be recorded with better delay time resolution and larger real time step size

(100 fs instead of 50 fs) in order to have a frequency range of both axes of approximately 5 THz with a reasonable acquisition time. Additionally, reduction of scattered light giving less noise in the 2D maps and a better understanding of the physical mechanisms behind the causality of the experiment and phonon coherence will be addressed in the future work on this project.

Chapter 7

Conclusion and Outlook

The main goal of this thesis was to investigate nonlinear responses from vibrational modes crystalline materials using 2D THz spectroscopy. Prior to the performance of this experiment, the work has been divided into two overall milestones: a simulation study of nonlinear molecular dynamics in crystalline materials when intense pulses were applied, and an experimental preparation of the most suitable and intense THz source based on a table-top fs laser system.

For the simulations of THz induced nonlinear effects, an add-on module to the existing *ab-initio* DFT code CASTEP has been developed capable of applying a THz field to a molecular structure during an MD simulation. With this, field dependent MD simulations have been performed on ionic bonded CsI and hydrogen bonded sucrose, of which the sucrose crystal as expected exhibited the most interesting nonlinear phenomena for moderate field strengths. For field strengths on the order of MV/cm phonon bleaching and coupling between modes in the THz range was observed.

Beam characterizations of THz beams generated from three different media have been performed: DSTMS, $LiNbO_3$ and 2-color air plasmas. The DFG generated THz beams from the crystals of DSTMS and $LiNbO_3$ were measured to have Gaussian profiles, from which their beam qualities were classified with the M^2-factor. Having simple collinear phase matching conditions the highest beam quality has been measured from DSTMS with an M^2 value of less than 1.5, while the experimentally more complicated tilted-pulse-front technique used to achieve phase matching in $LiNbO_3$ resulted in an M^2 value of around 2. The THz beam emitted from a 2-color air plasma showed a much more complicated conical beam profile, which was focused to a single spot at the sample position using a pair of off-axis

parabolic mirrors. The collapse of the conical donut-shaped beam profile through the focal plane was here reconstructed for the first time in 3D using a commercial THz camera. In addition to the conical emission, a weak forward propagating on-axis THz mode was measured and characterized to have a Gaussian beam profile.

Besides the free-space focusing of intense THz pulses in order to achieve the highest possible field strength at the sample spot, it has been investigated how further enhancement of the THz field inside narrow, rectangular apertures in metallic films (slits) can be achieved. In addition to the field enhancement obtained from a resonant slit itself, it has been shown than an additional field enhancement can be achieved for an array of slits if the lattice resonances match the slit resonance. With this field enhancements higher than 35 have been observed for a micro-slit array resonant at 0.8 THz, which is about 60 % more than what can be achieved in an isolated slit of identical dimensions.

Based on the results of the simulation studies of nonlinear effects in sucrose, it was found that the organic crystals of DAST and DSTMS were most suitable for THz generation in a spectroscopic experiment since they achieved the highest field strengths of almost 5 MV/cm, and were covering the most interesting spectral region from 1 to 5 THz. At the same time the collinear phase matching geometry resulting in a good beam quality was most favorable for the following spectroscopy experiments. Even though several papers have recently demonstrated how high pulse energies efficiently can be generated from such organic crystals [105, 106], this is one of the first demonstrations of high-field 1D spectroscopy performed with DSTMS [212]. With this, phonon bleaching has been observed in sucrose and ZnTe, and THz-field induced impact ionization in the indirect bandgap semiconductor silicon was observed as a significantly decreased transmission at high field strength through a bulk Si wafer.

With both this 1D spectroscopy study and the THz modulated MD simulations performed with CASTEP, it is conclusive that field strengths on the order of several MV/cm are required for nonlinear studies of vibrational modes in hydrogen bonded biomolecules such as sucrose. Such field strengths are significantly higher than what is typically used for investigation of THz-frequency nonlinear effects in semiconductor systems where tens of kV/cm have been demonstrated to be sufficient for observations of nonlinear

carrier dynamics. This is fundamental for the 2D spectroscopy system built for the investigation of nonlinear phonon dynamics in sucrose, where the MV/cm field strengths and simple phase matching geometry were the decisive arguments for choosing the organic crystals as THz sources for the 2D spectroscopy experiment.

With the demonstrated scheme for directly measuring nonlinear contributions from the collinear 2D spectroscopy setup, sucrose was investigated at temperatures down to 10 K. Nonlinear pump-probe signals have been measured, which were most significant at cold temperatures. From this, it was shown that these are likely to originate from nonlinear beating between the low-frequency vibrational modes between and 1 and 4 THz. At the same time it has been shown that the vibrational modes preserve the coherence information in the nonlinear pump-probe signals over periods of several picoseconds. Such long-lived coherence has not been observed in previous reports on studies of semiconductor systems.

With the strict timeline of three years for this PhD project, there are obviously a number of further investigations to be done, and at the same time the results have opened for a number of new interesting studies. For the CASTEP simulation study an obvious continuation is to extend the add-on module to include two THz pulses with a variable delay time in order to replicate and gain further insight into the results of the 2D experiment presented in this thesis. However, with the calculation times experienced for the 1D sucrose simulations, it is expected that such *ab initio* MD simulations will be extremely time consuming, and thus require access to more massive supercomputing architectures than what has been available for this project. A possible approach is also to consider other software packages such as CHARMM with predefined force fields for possible calculations of nonlinear effects, since this approach typically handles MD simulations of complex biomolecules within a much shorter computational time. A direct comparison of simulation results performed with such a software solution with the results presented in Chapter 2 would indicate the potential of using predefined force fields for future nonlinear studies. If the third-order nonlinear THz susceptibility of the molecular crystal can be estimated, for instance based on the linear dispersion of the system, a simpler, phenomenological semi-analytical simulation approach should also be able to offer insight into the general nonlinear behavior, including the coherence properties.

A number of prospective experiments are as well considered for future studies which are listed in the following. Firstly, the main limitation of the acquisition time for the 2D experiments is the low repetition rate used when pumping the DAST and DSTMS. For future experiments it would be highly desired to investigate the thermal properties of these crystals in order to find a way to be able to increase the repetition rate to 1 kHz as possible with laser systems such as the Spitfire Ace, while maintaining pump energies in the mJ range. Possible solutions to investigate could be to use a larger crystal with an expansion of the incident beam, or to use cryogenic cooling of the organic crystals. However, the high cost of these crystals suggests that fundamental background research on the improvement of thermal properties of the crystals would also be very beneficial. Finally, optimized focusing of the THz beam, for instance by prefocusing of the pump beam, has been shown to be a very versatile method for increasing the field strength [106], and this is a natural route to follow in the general optimization of a 2D spectroscopic setup.

For the beam profile characterization of the THz beam generated from 2-color air plasma, the origin of the asymmetric intensity distribution of the conical beam profile is at this moment unknown. However, it is suggested to investigate if it is related to the shape of the optical beams generating the air plasma. Initial tests have indicated that the distribution of THz energy in the conical emission pattern can be modified by physically blocking parts of the pump beam. For a more careful study of this effect, commercial beam shaper can be implemented in the beam path. However, this may require additional dispersion compensation for the optical elements in the beam shaper. At the same time an alternative technique for obtaining frequency resolved beam profiles rather than using bandpass filters, could be to guide the THz beam through an interferometric setup, and from this obtain field autocorrelations from which the frequency resolved beam profiles can be measured. This would also provide additional knowledge about the frequency response of the THz camera.

Future experiments will concern spectroscopic investigations of absorption features in crystalline materials at high fields using slit-arrays where the slit widths have been reduced to 200 nm in order to increase the absorption cross-section. These arrays have the possibility to be fabricated with even narrower slits widths below 100 nm, which have shown to result in field enhancements of more than 1000 [156], and for such high field

enhancements, the THz field has even caused damage to the metamaterial structure [127]. Despite the high potential of these field enhancing structures, it has still not been utilized for investigations of high-field THz pulse induced nonlinear responses of vibrational modes. For this, the field enhancing structures need to be carefully characterized and designed in order to match the vibrational modes of interest. In order to experimentally characterize the field distribution of the lattice modes simulated for the slit array presented in Chapter 5, a near-field imaging technique similar to what is presented in [213] can be implemented, where the slit array possibly can be fabricated on a $LiNbO_3$ substrate in order to utilize the EO properties of this for local THz field detection in the near-field zone of the slits.

The 2D spectroscopy experiments performed on cryogenically cooled sucrose showed much higher nonlinearities than at room temperature. The 1D spectroscopy results are therefore likely to exhibit higher nonlinearities if the sucrose crystal also is cooled to 10 K for this experiment. The most important immediate-future experiment for the spectroscopic investigation of sucrose will be to sample with better time delay resolution allowing for a Nyquist frequency higher than 2.5 THz. This, possibly together with even higher field strengths, is proposed for a way to detect THz induced FWM signals in sucrose, in addition to the nonlinear pump-probe signals observed here. Higher field strengths can first of all be achieved by combining the two THz pulses without the usage of the silicon beam splitter, however, the spatial alignment of two non-collinear beams incident on an off-axis parabolic mirror is in practice rather complicated. In the 2D experiments presented here where the field strength of each THz beam is expected to be on the order of 1 MV/cm, was however, capable of providing coherent nonlinear pump-probe signals containing information about vibrational couplings in sucrose, which are still subject for studies revealing the details about their physical mechanisms.

Chapter 8

References

8.1. Bibliography

[1] P. Hamm, and M. Zanni, *Concepts and Methods of 2D Infrared Spectroscopy* (Cambridge University Press, 2011).
[2] P. U. Jepsen, and S. J. Clark, "Precise ab-initio prediction of terahertz vibrational modes in crystalline systems," Chem. Phys. Lett. **442**, 275-280 (2007).
[3] M. Grishin, and A. Michailovas, "Dynamics of Continuously Pumped Solid-State Regenerative Amplifiers," InTech (2010).
[4] W. Kuehn, K. Reimann, M. Woerner, and T. Elsaesser, "Phase-resolved two-dimensional spectroscopy based on collinear n-wave mixing in the ultrafast time domain," J. Chem. Phys. **130**, 164503 (2009).
[5] J.-S. Rieh, S. Jeon, and M. Kim, "An overview of integrated THz electronics for communication applications," Conference: Circuits and Systems (MWSCAS), 2011 IEEE 54th International Midwest Symposium on, 1-4 (2011).
[6] J. D. Buron, D. H. Petersen, P. Boggild, D. G. Cooke, M. Hilke, J. Sun, E. Whiteway, P. F. Nielsen, O. Hansen, A. Yurgens, and P. U. Jepsen, "Graphene conductance uniformity mapping," Nano Lett. **12**, 5074-5081 (2012).
[7] Q. Zhang, E. H. Haroz, Z. Jin, L. Ren, X. Wang, R. S. Arvidson, A. Luttge, and J. Kono, "Plasmonic nature of the terahertz conductivity peak in single-wall carbon nanotubes," Nano Lett. **13**, 5991-5996 (2013).
[8] Y. Sano, I. Kawayama, M. Tabata, K. A. Salek, H. Murakami, M. Wang, R. Vajtai, P. M. Ajayan, J. Kono, and M. Tonouchi, "Imaging molecular adsorption and desorption dynamics on graphene using terahertz emission spectroscopy," Sci. Rep. **4**, 6046 (2014).
[9] T. L. Cocker, V. Jelic, M. Gupta, S. J. Molesky, J. A. J. Burgess, G. D. L. Reyes, L. V. Titova, Y. Y. Tsui, M. R. Freeman, and F. A. Hegmann, "An ultrafast terahertz scanning tunnelling microscope," Nature Photon. **7**, 620-625 (2013).
[10] M. Eisele, T. L. Cocker, M. A. Huber, M. Plankl, L. Viti, D. Ercolani, L. Sorba, M. S. Vitiello, and R. Hober, "Ultrafast multi-terahertz nano-

spectroscopy with sub-cycle temporal resolution," Nature Photon. **8**, 841-845 (2014).
[11] R. H. Clothier, and N. Bourne, "Effects of THz Exposure on Human Primary Keratinocyte Differentiation and Viability," J. Biol. Phys. **29**, 179-185 (2003).
[12] L. V. Titova, A. K. Ayesheshim, A. Golubov, D. Fogen, R. Rodriguez-Juarez, F. A. Hegmann, and O. Kovalchuk, "Intense THz pulses cause H2AX phosphorylation and activate DNA damage response in human skin tissue," Biomed. Opt. Express **4**, 559-568 (2013).
[13] G. Herink, L. Wimmer, and C. Ropers, "Field emission at terahertz frequencies: AC-tunneling and ultrafast carrier dynamics," New J. Phys. **16**, 123005 (2014).
[14] A. Strikwerda, M. Zalkovskij, K. Iwaszczuk, and P. U. Jepsen, "Terahertz field induced electromigration," 39th International Conference on Infrared, Millimeter, and Terahertz Waves (2014).
[15] K. Iwaszczuk, M. Zalkovskij, A. C. Strikwerda, and P. U. Jepsen, "Nitrogen plasma formation through terahertz-induced ultrafast electron field emission," Optica **2**, 116 (2015).
[16] M. Jewariya, M. Nagai, and K. Tanaka, "Ladder Climbing on the Anharmonic Intermolecular Potential in an Amino Acid Microcrystal via an Intense Monocycle Terahertz Pulse," Phys. Rev. Lett. **105** (2010).
[17] F. Fassioli, R. Dinshaw, P. C. Arpin, and G. D. Scholes, "Photosynthetic light harvesting: excitons and coherence," J. R. Soc. Interface **11**, 20130901 (2014).
[18] T. Elsaesser, K. Reimann, and M. Woerner, "Focus: Phase-resolved nonlinear terahertz spectroscopy—From charge dynamics in solids to molecular excitations in liquids," J. Chem. Phys. **142**, 212301 (2015).
[19] H. R. Park, K. J. Ahn, S. Han, Y. M. Bahk, N. Park, and D. S. Kim, "Colossal absorption of molecules inside single terahertz nanoantennas," Nano Lett. **13**, 1782-1786 (2013).
[20] B. R. Brooks, R. E. Bruccoleri, B. D. Olafson, D. J. States, S. Swaminathan, and M. Karplus, "CHARMM: A program for macromolecular energy, minimization, and dynamics calculations," J. Comput. Chem. **4**, 187-217 (1983).
[21] T. M. Korter, R. Balu, M. B. Campbell, M. C. Beard, S. K. Gregurick, and E. J. Heilweil, "Terahertz spectroscopy of solid serine and cysteine," Chem. Phys. Lett. **418**, 65-70 (2006).
[22] G. Acbas, K. A. Niessen, E. H. Snell, and A. G. Markelz, "Optical measurements of long-range protein vibrations," Nat. Commun. **5**, 3076 (2014).
[23] B. Delley, "An all-electron numerical method for solving the local density functional for polyatomic molecules," J. Chem. Phys. **92**, 508 (1990).

[24] B. Delley, "From molecules to solids with the DMol^3 approach," J. Chem. Phys. **113**, 7756 (2000).
[25] S. Plimpton, "Fast Parallel Algorithms for Short-Range Molecular Dynamics," J. Comput. Phys. **117**, 1-19 (1995).
[26] A. Pereverzev, and T. D. Sewell, "Terahertz normal mode relaxation in pentaerythritol tetranitrate," J. Chem. Phys. **134**, 014513 (2011).
[27] A. Pereverzev, T. D. Sewell, and D. L. Thompson, "Calculation of anharmonic couplings and THz linewidths in crystalline PETN," J. Chem. Phys. **140**, 104508 (2014).
[28] D. G. Allis, and T. M. Korter, "Theoretical analysis of the terahertz spectrum of the high explosive PETN," ChemPhysChem **7**, 2398-2408 (2006).
[29] D. G. Allis, D. A. Prokhorova, and T. M. Korter, "Solid-state modeling of the terahertz spectrum of the high explosive HMX," J. Phys. Chem. A **110**, 1951-1959 (2006).
[30] D. Marx, and J. Hutter, "Ab initio molecular dynamics: Theory and Implementation," (2000), http://www.theochem.ruhr-uni-bochum.de/research/marx/marx.pdf.
[31] S. Patel, A. D. Mackerell, Jr., and C. L. Brooks, 3rd, "CHARMM fluctuating charge force field for proteins: II protein/solvent properties from molecular dynamics simulations using a nonadditive electrostatic model," J. Comput. Chem. **25**, 1504-1514 (2004).
[32] D. K. Remler, and P. A. Madden, "Molecular dynamics without effective potentials via the Car-Parrinello approach," Mol. Phys. **70**, 921-966 (1990).
[33] M. D. Segall, P. J. D. Lindan, M. J. Probert, C. J. Pickard, P. J. Hasnip, S. J. Clark, and M. C. Payne, "First-principles simulation: ideas, illustrations and the CASTEP code," J. Phys. Condens. Matter **14**, 2717-2744 (2002).
[34] M. C. Payne, T. A. Arias, and J. D. Joannopoulos, "Iterative minimization techniques for ab initio total-energy calculations: molecular dynamics and conjugate gradients," Rev. Mod. Phys. **64**, 1045-1097 (1992).
[35] V. Milman, K. Refson, S. J. Clark, C. J. Pickard, J. R. Yates, S. P. Gao, P. J. Hasnip, M. I. J. Probert, A. Perlov, and M. D. Segall, "Electron and vibrational spectroscopies using DFT, plane waves and pseudopotentials: CASTEP implementation," J. Mol. Struct. (Theochem.) **954**, 22-35 (2010).
[36] M. Walther, B. M. Fischer, and P. Uhd Jepsen, "Noncovalent intermolecular forces in polycrystalline and amorphous saccharides in the far infrared," Chem. Phys. **288**, 261-268 (2003).
[37] R. S. Mulliken, "Electronic Population Analysis on LCAO[Single Bond]MO Molecular Wave Functions. I," J. Chem. Phys. **23**, 1833 (1955).
[38] G. J. Martyna, M. L. Klein, and M. Tuckerman, "Nosé–Hoover chains: The canonical ensemble via continuous dynamics," J. Chem. Phys. **97**, 2635 (1992).

[39] B. Santra, "Density-Functional Theory Exchange-Correlation Functionals for Hydrogen Bonds in Water," in *Fakultät II Mathematik und Naturwissenschaften*(Technischen Universität Berlin, 2010).
[40] J. P. Perdew, K. Burke, and M. Ernzerhof, "Generalized Gradient Approximation Made Simple," Phys. Rev. Lett. **77**, 3865-3868 (1996).
[41] J. P. Perdew, K. Burke, and M. Ernzerhof, "Generalized Gradient Approximation Made Simple [Phys. Rev. Lett. 77, 3865 (1996)]," Phys. Rev. Lett. **78**, 1396-1396 (1997).
[42] C. Liu, N. Kioussis, S. Demos, and H. Radousky, "Electron- or Hole-Assisted Reactions of H Defects in Hydrogen-Bonded KDP," Phys. Rev. Lett. **91** (2003).
[43] P. U. Jepsen, B. Fischer, and M, "Dynamic range in terahertz time-domain transmission and reflection spectroscopy," Opt. Lett. **30**, 29-31 (2005).
[44] T. Okada, M. Nagai, and K. Tanaka, "Resonant phase jump with enhanced electric field caused by surface phonon polariton in terahertz region," Opt. Express **16**, 5633 (2008).
[45] F. D. Brunner, A. Schneider, and P. Gunter, "A terahertz time-domain spectrometer for simultaneous transmission and reflection measurements at normal incidence," Opt. Express **17**, 20684-20693 (2009).
[46] R. P. Lowndes, and D. H. Martin, *Dielectric Dispersion and the Structures of Ionic Lattices* (1969).
[47] A. B. Brizuela, L. C. Bichara, E. Romano, A. Yurquina, S. Locatelli, and S. A. Brandan, "A complete characterization of the vibrational spectra of sucrose," Carbohydr. Res. **361**, 212-218 (2012).
[48] E. V. Loewenstein, "The history and current status of fourier transform spectroscopy," Appl. Opt. **5**, 845-854 (1966).
[49] P. F. Moulton, "Spectroscopic and laser characteristics of Ti:Al_2O_3," J. Opt. Soc. Am. B **3**, 125 (1986).
[50] D. H. Auston, "Picosecond optoelectronic switching and gating in silicon," Appl. Phys. Lett. **26**, 101 (1975).
[51] P. H. Siegel, "Terahertz Pioneer: David H. Auston," IEEE Trans. Terahertz Sci. Technol. **1**, 6-8 (2011).
[52] M. v. Exter, C. Fattinger, and D. Grischkowsky, "Terahertz time-domain spectroscopy of water vapor," Opt. Lett. **14**, 1128 (1989).
[53] C. Fattinger, and D. Grischkowsky, "Terahertz beams," Appl. Phys. Lett. **54**, 490 (1989).
[54] M. Bass, P. Franken, J. Ward, and G. Weinreich, "Optical Rectification," Phys. Rev. Lett. **9**, 446-448 (1962).
[55] L. Xu, X. C. Zhang, and D. H. Auston, "Terahertz beam generation by femtosecond optical pulses in electro-optic materials," Appl. Phys. Lett. **61**, 1784 (1992).

[56] A. Rice, Y. Jin, X. F. Ma, X. C. Zhang, D. Bliss, J. Larkin, and M. Alexander, "Terahertz optical rectification from <110> zinc-blende crystals," Appl. Phys. Lett. **64**, 1324 (1994).
[57] P. U. Jepsen, D. G. Cooke, and M. Koch, "Terahertz spectroscopy and imaging - Modern techniques and applications," Laser Photon. Rev. **5**, 124-166 (2011).
[58] K. H. Yang, "Generation of Far-Infrared Radiation by Picosecond Light Pulses in $LiNbO_3$," Appl. Phys. Lett. **19**, 320 (1971).
[59] Q. Wu, and X. C. Zhang, "Free-space electro-optic sampling of terahertz beams," Appl. Phys. Lett. **67**, 3523 (1995).
[60] P. Jepsen, C. Winnewisser, M. Schall, V. Schyja, S. Keiding, and H. Helm, "Detection of THz pulses by phase retardation in lithium tantalate," Phys.Rev. E **53**, R3052-R3054 (1996).
[61] A. Nahata, D. H. Auston, T. F. Heinz, and C. Wu, "Coherent detection of freely propagating terahertz radiation by electro-optic sampling," Appl. Phys. Lett. **68**, 150 (1996).
[62] D. You, R. R. Jones, P. H. Bucksbaum, and D. R. Dykaar, "Generation of high-power sub-single-cycle 500-fs electromagnetic pulses," Opt. Lett. **18**, 290 (1993).
[63] E. Budiarto, J. Margolies, S. Jeong, J. Son, and J. Bokor, "High-intensity terahertz pulses at 1-kHz repetition rate," IEEE J. Quantum Electron. **32**, 1839-1846 (1996).
[64] P. U. Jepsen, R. H. Jacobsen, and S. R. Keiding, "Generation and detection of terahertz pulses from biased semiconductor antennas," J. Opt. Soc. Am. B **13**, 2424 (1996).
[65] F. Blanchard, L. Razzari, H. C. Bandulet, G. Sharma, R. Morandotti, J. C. Kieffer, T. Ozaki, M. Reid, H. F. Tiedje, H. K. Haugen, and F. A. Hegmann, "Generation of 1.5 μJ single-cycle terahertz pulses by optical rectification from a large aperture ZnTe crystal," Opt. Express **15**, 13212 (2007).
[66] K. L. Yeh, M. C. Hoffmann, J. Hebling, and K. A. Nelson, "Generation of 10 μJ ultrashort terahertz pulses by optical rectification," Appl. Phys. Lett. **90**, 171121 (2007).
[67] J. A. Fulop, Z. Ollmann, C. Lombosi, C. Skrobol, S. Klingebiel, L. Palfalvi, F. Krausz, S. Karsch, and J. Hebling, "Efficient generation of THz pulses with 0.4 mJ energy," Opt. Express **22**, 20155-20163 (2014).
[68] D. J. Cook, and R. M. Hochstrasser, "Intense terahertz pulses by four-wave rectification in air," Opt. Lett. **25**, 1210-1212 (2000).
[69] N. Karpowicz, J. Dai, X. Lu, Y. Chen, M. Yamaguchi, H. Zhao, X. C. Zhang, L. Zhang, C. Zhang, M. Price-Gallagher, C. Fletcher, O. Mamer, A. Lesimple, and K. Johnson, "Coherent heterodyne time-domain spectrometry covering the entire “terahertz gap”," Appl. Phys. Lett. **92**, 011131 (2008).

[70] M. D. Thomson, V. Blank, and H. G. Roskos, "Terahertz white-light pulses from an air plasma photo-induced by incommensurate two-color optical fields," Opt. Express **18**, 23173-23182 (2010).
[71] D. Grischkowsky, S. Keiding, M. v. Exter, and C. Fattinger, "Far-infrared time-domain spectroscopy with terahertz beams of dielectrics and semiconductors," J. Opt. Soc. Am. B **7**, 2006 (1990).
[72] Y.-S. Lee, *Principles of Terahertz Science and Technology* (Springer Science+Business Media, 2009).
[73] S. Gupta, M. Y. Frankel, J. A. Valdmanis, J. F. Whitaker, G. A. Mourou, F. W. Smith, and A. R. Calawa, "Subpicosecond carrier lifetime in GaAs grown by molecular beam epitaxy at low temperatures," Appl. Phys. Lett. **59**, 3276 (1991).
[74] A. Dreyhaupt, S. Winnerl, T. Dekorsy, and M. Helm, "High-intensity terahertz radiation from a microstructured large-area photoconductor," Appl. Phys. Lett. **86**, 121114 (2005).
[75] B. Sartorius, H. Roehle, H. Künzel, J. Böttcher, M. Schlak, D. Stanze, H. Venghaus, and M. Schell, "All-fiber terahertz time-domain spectrometer operating at 1.5 μm telecom wavelengths," Opt. Express **16**, 9565 (2008).
[76] C. L. K. Dandolo, and P. U. Jepsen, "THz reflectometric imaging of medieval wall paintings," Infrared, Millimeter, and Terahertz Waves (IRMMW-THz), 2013 38th International Conference on, 13915984 (2013).
[77] C. L. K. Dandolo, and P. U. Jepsen, "THz reflectometric imaging of contemporary panel artwork," Infrared, Millimeter, and Terahertz Waves (IRMMW-THz), 2013 38th International Conference on, 13916040 (2013).
[78] D. Strickland, and G. Mourou, "Compression of amplified chirped optical pulses," Opt. Commun. **55**, 447-449 (1985).
[79] A. Tomasino, A. Parisi, S. Stivala, P. Livreri, A. C. Cino, A. C. Busacca, M. Peccianti, and R. Morandotti, "Wideband THz time domain spectroscopy based on optical rectification and electro-optic sampling," Sci. Rep. **3**, 3116 (2013).
[80] G. P. Agrawal, *Nonlinear Fiber Optics (Fourth Edition)*, (Academic Press, San Diego, 2006).
[81] A. Nahata, A. S. Weling, and T. F. Heinz, "A wideband coherent terahertz spectroscopy system using optical rectification and electro-optic sampling," Appl. Phys. Lett. **69**, 2321 (1996).
[82] X.-C. Zhang, and J. Xu, *Introduction to THz Wave Photonics* (Springer US, 2010).
[83] R. A. Kaindl, F. Eickemeyer, M. Woerner, and T. Elsaesser, "Broadband phase-matched difference frequency mixing of femtosecond pulses in GaSe: Experiment and theory," Appl. Phys. Lett. **75**, 1060 (1999).
[84] D. N. Erschens, D. Turchinovich, and P. U. Jepsen, "Optimized Optical Rectification and Electro-optic Sampling in ZnTe Crystals with Chirped Femtosecond Laser Pulses," J. Infrared Millim. Terahertz Waves **32**, 1371-1381 (2011).

[85] G. Gallot, J. Zhang, R. W. McGowan, T.-I. Jeon, and D. Grischkowsky, "Measurements of the THz absorption and dispersion of ZnTe and their relevance to the electro-optic detection of THz radiation," Appl. Phys. Lett. **74**, 3450 (1999).
[86] Q. Wu, and X. C. Zhang, "Ultrafast electro-optic field sensors," Appl. Phys. Lett. **68**, 1604 (1996).
[87] J. Hebling, K.-L. Yeh, M. C. Hoffmann, B. Bartal, and K. A. Nelson, "Generation of high-power terahertz pulses by tilted-pulse-front excitation and their application possibilities," J. Opt. Soc. Am. B **25**, B6 (2008).
[88] D. A. Bryan, R. Gerson, and H. E. Tomaschke, "Increased optical damage resistance in lithium niobate," Appl. Phys. Lett. **44**, 847 (1984).
[89] J. Hebling, G. Almasi, I. Kozma, and J. Kuhl, "Velocity matching by pulse front tilting for large area THz-pulse generation," Opt. Express **10**, 1161 (2002).
[90] J. Hebling, A. G. Stepanov, G. Almási, B. Bartal, and J. Kuhl, "Tunable THz pulse generation by optical rectification of ultrashort laser pulses with tilted pulse fronts," Appl. Phys. B **78**, 593-599 (2004).
[91] Z. Wang, A. Ayesheshim, F. Su, and F. Hegmann, "Ultrafast imaging of terahertz pulse generation by tilted optical pulse front in $LiNbO_3$," in Conference on Lasers and Electro-Optics 2012, OSA Technical Digest (online) (Optical Society of America, 2012), CTu3B.5 (2012).
[92] Z. Wang, F. Su, and F. A. Hegmann, "Ultrafast imaging of terahertz Cherenkov waves and transition-like radiation in $LiNbO_3$," Opt. Express **23**, 8073 (2015).
[93] H. Hirori, A. Doi, F. Blanchard, and K. Tanaka, "Single-cycle terahertz pulses with amplitudes exceeding 1 MV/cm generated by optical rectification in $LiNbO_3$," Appl. Phys. Lett. **98**, 091106 (2011).
[94] J. A. Fulop, L. Palfalvi, S. Klingebiel, G. Almasi, F. Krausz, S. Karsch, and J. Hebling, "Generation of sub-mJ terahertz pulses by optical rectification," Opt. Lett. **37**, 557-559 (2012).
[95] S. W. Huang, E. Granados, W. R. Huang, K. H. Hong, L. E. Zapata, and F. X. Kartner, "High conversion efficiency, high energy terahertz pulses by optical rectification in cryogenically cooled lithium niobate," Opt. Lett. **38**, 796-798 (2013).
[96] J. A. Fulop, L. Palfalvi, G. Almasi, and J. Hebling, "Design of high-energy terahertz sources based on optical rectification," Opt. Express **18**, 12311-12327 (2010).
[97] F. Blanchard, X. Ropagnol, H. Hafez, H. Razavipour, M. Bolduc, R. Morandotti, T. Ozaki, and D. G. Cooke, "Effect of extreme pump pulse reshaping on intense terahertz emission in lithium niobate at multimilliJoule pump energies," Opt. Lett. **39**, 4333-4336 (2014).
[98] A. Schneider, M. Neis, M. Stillhart, B. Ruiz, R. U. A. Khan, and P. Günter, "Generation of terahertz pulses through optical rectification in

organic DAST crystals: theory and experiment," J. Opt. Soc. Am. B **23**, 1822 (2006).
[99] X. C. Zhang, X. F. Ma, Y. Jin, T. M. Lu, E. P. Boden, P. D. Phelps, K. R. Stewart, and C. P. Yakymyshyn, "Terahertz optical rectification from a nonlinear organic crystal," Appl. Phys. Lett. **61**, 3080 (1992).
[100] M. Walther, K. Jensby, S. R. Keiding, H. Takahashi, and H. Ito, "Far-infrared properties of DAST," Opt. Lett. **25**, 911 (2000).
[101] A. Schneider, and P. Günter, "Spectrum of Terahertz Pulses from Organic DAST Crystals," Ferroelectrics **318**, 83-88 (2005).
[102] L. Mutter, F. D. Brunner, Z. Yang, M. Jazbinšek, and P. Günter, "Linear and nonlinear optical properties of the organic crystal DSTMS," J. Opt. Soc. Am. B **24**, 2556 (2007).
[103] Z. Yang, L. Mutter, M. Stillhart, B. Ruiz, S. Aravazhi, M. Jazbinsek, A. Schneider, V. Gramlich, and P. Günter, "Large-Size Bulk and Thin-Film Stilbazolium-Salt Single Crystals for Nonlinear Optics and THz Generation," Adv. Funct. Mater. **17**, 2018-2023 (2007).
[104] M. Stillhart, A. Schneider, and P. Günter, "Optical properties of 4-N,N-dimethylamino-4′-N′-methyl-stilbazolium 2,4,6-trimethylbenzenesulfonate crystals at terahertz frequencies," J. Opt. Soc. Am. B **25**, 1914 (2008).
[105] C. P. Hauri, C. Ruchert, C. Vicario, and F. Ardana, "Strong-field single-cycle THz pulses generated in an organic crystal," Appl. Phys. Lett. **99**, 161116 (2011).
[106] M. Shalaby, and C. P. Hauri, "Demonstration of a low-frequency three-dimensional terahertz bullet with extreme brightness," Nat. Commun. **6**, 5976 (2015).
[107] F. Buccheri, and X. C. Zhang, "Terahertz wave emission from laser-induced micro-plasma," Infrared, Millimeter, and Terahertz waves (IRMMW-THz), 2014 39th International Conference on, 14771036 (2014).
[108] F. Buccheri, and X.-C. Zhang, "Terahertz emission from laser-induced microplasma in ambient air," Optica **2**, 366 (2015).
[109] H. Zhong, N. Karpowicz, and X. C. Zhang, "Terahertz emission profile from laser-induced air plasma," Appl. Phys. Lett. **88**, 261103 (2006).
[110] Y. S. You, T. I. Oh, and K. Y. Kim, "Off-Axis Phase-Matched Terahertz Emission from Two-Color Laser-Induced Plasma Filaments," Phys. Rev. Lett. **109** (2012).
[111] P. Klarskov, A. C. Strikwerda, K. Iwaszczuk, and P. U. Jepsen, "Experimental three-dimensional beam profiling and modeling of a terahertz beam generated from a two-color air plasma," New J. Phys. **15**, 075012 (2013).
[112] V. Blank, M. D. Thomson, and H. G. Roskos, "Spatio-spectral characteristics of ultra-broadband THz emission from two-colour photoexcited gas plasmas and their impact for nonlinear spectroscopy," New J. Phys. **15**, 075023 (2013).

[113] K. Y. Kim, A. J. Taylor, J. H. Glownia, and G. Rodriguez, "Coherent control of terahertz supercontinuum generation in ultrafast laser–gas interactions," Nature Photon. **2**, 605-609 (2008).
[114] T. I. Oh, Y. J. Yoo, Y. S. You, and K. Y. Kim, "Generation of strong terahertz fields exceeding 8 MV/cm at 1 kHz and real-time beam profiling," Appl. Phys. Lett. **105**, 041103 (2014).
[115] X. Sun, and X. C. Zhang, "Terahertz radiation in alkali vapor plasmas," Appl. Phys. Lett. **104**, 191106 (2014).
[116] T. Popmintchev, M. C. Chen, D. Popmintchev, P. Arpin, S. Brown, S. Alisauskas, G. Andriukaitis, T. Balciunas, O. D. Mucke, A. Pugzlys, A. Baltuska, B. Shim, S. E. Schrauth, A. Gaeta, C. Hernandez-Garcia, L. Plaja, A. Becker, A. Jaron-Becker, M. M. Murnane, and H. C. Kapteyn, "Bright coherent ultrahigh harmonics in the keV x-ray regime from mid-infrared femtosecond lasers," Science **336**, 1287-1291 (2012).
[117] F. Krausz, "Attosecond physics," Rev. Mod. Phys. **81**, 163-234 (2009).
[118] M. Clerici, M. Peccianti, B. E. Schmidt, L. Caspani, M. Shalaby, M. Giguere, A. Lotti, A. Couairon, F. Legare, T. Ozaki, D. Faccio, and R. Morandotti, "Wavelength scaling of terahertz generation by gas ionization," Phys. Rev. Lett. **110**, 253901 (2013).
[119] K. Iwaszczuk, "Terahertz Technology for Defense and Security-Related Applications," (Technical University of Denmark, 2012).
[120] Q. Wu, and X. C. Zhang, "7 terahertz broadband GaP electro-optic sensor," Appl. Phys. Lett. **70**, 1784 (1997).
[121] F. D'Angelo, Z. Mics, M. Bonn, and D. Turchinovich, "Ultra-broadband THz time-domain spectroscopy of common polymers using THz air photonics," Opt. Express **22**, 12475-12485 (2014).
[122] M. Zalkovskij, C. Zoffmann Bisgaard, A. Novitsky, R. Malureanu, D. Savastru, A. Popescu, P. Uhd Jepsen, and A. V. Lavrinenko, "Ultrabroadband terahertz spectroscopy of chalcogenide glasses," Appl. Phys. Lett. **100**, 031901 (2012).
[123] J. D. Buron, F. Pizzocchero, B. S. Jessen, T. J. Booth, P. F. Nielsen, O. Hansen, M. Hilke, E. Whiteway, P. U. Jepsen, P. Boggild, and D. H. Petersen, "Electrically continuous graphene from single crystal copper verified by terahertz conductance spectroscopy and micro four-point probe," Nano Lett. **14**, 6348-6355 (2014).
[124] D. G. Cooke, A. Meldrum, and P. Uhd Jepsen, "Ultrabroadband terahertz conductivity of Si nanocrystal films," Appl. Phys. Lett. **101**, 211107 (2012).
[125] D. G. Cooke, F. C. Krebs, and P. U. Jepsen, "Direct Observation of Sub-100 fs Mobile Charge Generation in a Polymer-Fullerene Film," Phys. Rev. Lett. **108** (2012).
[126] T. Wang, P. Klarskov, and P. U. Jepsen, "Ultrabroadband THz Time-Domain Spectroscopy of a Free-Flowing Water Film," IEEE Trans. Terahertz Sci. Technol. **4**, 425-431 (2014).

[127] M. Liu, H. Y. Hwang, H. Tao, A. C. Strikwerda, K. Fan, G. R. Keiser, A. J. Sternbach, K. G. West, S. Kittiwatanakul, J. Lu, S. A. Wolf, F. G. Omenetto, X. Zhang, K. A. Nelson, and R. D. Averitt, "Terahertz-field-induced insulator-to-metal transition in vanadium dioxide metamaterial," Nature **487**, 345-348 (2012).
[128] J. Van Rudd, J. L. Johnson, and D. M. Mittleman, "Cross-polarized angular emission patterns from lens-coupled terahertz antennas," J. Opt. Soc. Am. B **18**, 1524 (2001).
[129] A. Gorodetsky, A. D. Koulouklidis, M. Massaouti, and S. Tzortzakis, "Physics of the conical broadband terahertz emission from two-color laser-induced plasma filaments," Phys. Rev. A **89**, 033838 (2014).
[130] A. V. Borodin, M. N. Esaulkov, I. I. Kuritsyn, I. A. Kotelnikov, and A. P. Shkurinov, "On the role of photoionization in generation of terahertz radiation in the plasma of optical breakdown," J. Opt. Soc. Am. B **29**, 1911 (2012).
[131] M. T. Reiten, and R. A. Cheville, "Effect of spherical aberration and surface waves on propagation of lens-coupled terahertz pulses," Opt. Lett. **30**, 673 (2005).
[132] M. T. Reiten, S. A. Harmon, and R. A. Cheville, "Terahertz beam propagation measured through three-dimensional amplitude profile determination," J. Opt. Soc. Am. B **20**, 2215 (2003).
[133] A. Podzorov, A. Wojdyla, and G. Gallot, "Beam waist measurement for terahertz time-domain spectroscopy experiments," Opt. Lett. **35**, 901-903 (2010).
[134] H. Richter, A. D. Semenov, S. G. Pavlov, L. Mahler, A. Tredicucci, H. E. Beere, D. A. Ritchie, K. S. Il'in, M. Siegel, and H. W. Hübers, "Terahertz heterodyne receiver with quantum cascade laser and hot electron bolometer mixer in a pulse tube cooler," Appl. Phys. Lett. **93**, 141108 (2008).
[135] N. Oda, "Uncooled bolometer-type Terahertz focal plane array and camera for real-time imaging," C. R. Phys. **11**, 496-509 (2010).
[136] C. R. Petersen, U. Møller, I. Kubat, B. Zhou, S. Dupont, J. Ramsay, T. Benson, S. Sujecki, N. Abdel-Moneim, Z. Tang, D. Furniss, A. Seddon, and O. Bang, "Mid-infrared supercontinuum covering the 1.4–13.3 μm molecular fingerprint region using ultra-high NA chalcogenide step-index fibre," Nature Photon. **8**, 830-834 (2014).
[137] Personal communication with S. Tzortzakis.
[138] C. J. R. Sheppard, and T. Wilson, "Gaussian-beam theory of lenses with annular aperture," in *IEE Proc. H*(1978), pp. 105-112.
[139] F. Gori, G. Guattari, and C. Padovani, "Bessel-Gauss beams," Opt. Commun. **64**, 491-495 (1987).
[140] D. N. Schimpf, J. Schulte, W. P. Putnam, and F. X. Kärtner, "Generalizing higher-order Bessel-Gauss beams: analytical description and demonstration," Opt. Express **20**, 26852-26867 (2012).

[141] W. P. Putnam, D. N. Schimpf, G. Abram, and F. X. Kärtner, "Bessel-Gauss beam enhancement cavities for high-intensity applications," Opt. Express **20**, 24429-24443 (2012).
[142] K.-Y. Kim, "Generation of coherent terahertz radiation in ultrafast laser-gas interactionsa)," Phys. Plasmas **16**, 056706 (2009).
[143] K.-Y. Kim, J. H. Glownia, A. J. Taylor, and G. Rodriguez, "Terahertz emission from ultrafast ionizing air in symmetry-broken laser fields," Opt. Express **15**, 4577-4584 (2007).
[144] V. S. Popov, "Tunnel and multiphoton ionization of atoms and ions in a strong laser field (Keldysh theory)," Phys. Usp. **47**, 855 (2004).
[145] B. Thidé, "Electromagnetic Field Theory, 2nd Ed.," (2011).
[146] J. S. A. Collins, "Lens-System Diffraction Integral Written in Terms of Matrix Optics," J. Opt. Soc. Am. **60**, 1168-1177 (1970).
[147] S. Hunsche, S. Feng, H. G. Winful, A. Leitenstorfer, M. C. Nuss, and E. P. Ippen, "Spatiotemporal focusing of single-cycle light pulses," J. Opt. Soc. Am. A **16**, 2025-2028 (1999).
[148] R. W. McGowan, R. A. Cheville, and D. Grischkowsky, "Direct observation of the Gouy phase shift in THz impulse ranging," Appl. Phys. Lett. **76**, 670-672 (2000).
[149] A. B. Ruffin, J. V. Rudd, J. F. Whitaker, S. Feng, and H. G. Winful, "Direct Observation of the Gouy Phase Shift with Single-Cycle Terahertz Pulses," Phys. Rev. Lett. **83**, 3410-3413 (1999).
[150] P. Kuzel, H. Nemec, F. Kadlec, and C. Kadlec, "Gouy shift correction for highly accurate refractive index retrieval in time-domain terahertz spectroscopy," Opt. Express **18**, 15338-15348 (2010).
[151] A. C. Strikwerda, M. Zalkovskij, D. Lund Lorenzen, A. Krabbe, A. V. Lavrinenko, and P. Uhd Jepsen, "Metamaterial composite bandpass filter with an ultra-broadband rejection bandwidth of up to 240 terahertz," Appl. Phys. Lett. **104**, 191103 (2014).
[152] O. Paul, R. Beigang, and M. Rahm, "Highly selective terahertz bandpass filters based on trapped mode excitation," Opt. Express **17**, 18590-18595 (2009).
[153] A. Toma, S. Tuccio, M. Prato, F. De Donato, A. Perucchi, P. Di Pietro, S. Marras, C. Liberale, R. Proietti Zaccaria, F. De Angelis, L. Manna, S. Lupi, E. Di Fabrizio, and L. Razzari, "Squeezing Terahertz Light into Nanovolumes: Nanoantenna Enhanced Terahertz Spectroscopy (NETS) of Semiconductor Quantum Dots," Nano Lett. (2014).
[154] R. Adato, A. A. Yanik, J. J. Amsden, D. L. Kaplan, F. G. Omenetto, M. K. Hong, S. Erramilli, and H. Altug, "Ultra-sensitive vibrational spectroscopy of protein monolayers with plasmonic nanoantenna arrays," Proc. Natl. Acad. Sci. U.S.A. **106**, 19227-19232 (2009).
[155] T. W. Ebbesen, H. J. Lezec, H. F. Ghaemi, T. Thio, and P. A. Wolff, "Extraordinary optical transmission through sub-wavelength hole arrays," Nature **391**, 667-669 (1998).

[156] M. A. Seo, H. R. Park, S. M. Koo, D. J. Park, J. H. Kang, O. K. Suwal, S. S. Choi, P. C. M. Planken, G. S. Park, N. K. Park, Q. H. Park, and D. S. Kim, "Terahertz field enhancement by a metallic nano slit operating beyond the skin-depth limit," Nature Photon. **3**, 152-156 (2009).
[157] W. Barnes, W. Murray, J. Dintinger, E. Devaux, and T. Ebbesen, "Surface Plasmon Polaritons and Their Role in the Enhanced Transmission of Light through Periodic Arrays of Subwavelength Holes in a Metal Film," Phys. Rev. Lett. **92** (2004).
[158] A. Bitzer, J. Wallauer, H. Helm, H. Merbold, T. Feurer, and M. Walther, "Lattice modes mediate radiative coupling in metamaterial arrays," Opt. Express **17**, 22108-22113 (2009).
[159] A. Mary, S. Rodrigo, L. Martín-Moreno, and F. García-Vidal, "Theory of light transmission through an array of rectangular holes," Phys. Rev. B **76** (2007).
[160] D. M. Mittleman, "Frontiers in terahertz sources and plasmonics," Nature Photon. **7**, 666-669 (2013).
[161] J. Liu, R. Mendis, and D. M. Mittleman, "The transition from a TEM-like mode to a plasmonic mode in parallel-plate waveguides," Appl. Phys. Lett. **98**, 231113 (2011).
[162] K. Iwaszczuk, A. Andryieuski, A. Lavrinenko, X. C. Zhang, and P. U. Jepsen, "Terahertz field enhancement to the MV/cm regime in a tapered parallel plate waveguide," Opt. Express **20**, 8344-8355 (2012).
[163] V. Astley, R. Mendis, and D. M. Mittleman, "Characterization of terahertz field confinement at the end of a tapered metal wire waveguide," Appl. Phys. Lett. **95**, 031104 (2009).
[164] V. Astley, J. Scheiman, R. Mendis, and D. M. Mittleman, "Bending and coupling losses in terahertz wire waveguides," Opt. Lett. **35**, 553-555 (2010).
[165] C. A. Balanis, *Antenna theory: analysis and design* (John Wiley & Sons, 2012).
[166] F. García-Vidal, E. Moreno, J. Porto, and L. Martín-Moreno, "Transmission of Light through a Single Rectangular Hole," Phys. Rev. Lett. **95** (2005).
[167] A. Degiron, and T. W. Ebbesen, "The role of localized surface plasmon modes in the enhanced transmission of periodic subwavelength apertures," J.Opt. A: Pure Appl.Op. **7**, S90-S96 (2005).
[168] F. J. García-Vidal, L. Martín-Moreno, E. Moreno, L. K. S. Kumar, and R. Gordon, "Transmission of light through a single rectangular hole in a real metal," Phys. Rev. B **74** (2006).
[169] M. Kominami, D. Pozar, and D. Schaubert, "Dipole and slot elements and arrays on semi-infinite substrates," IEEE Trans. Antennas Propag. **33**, 600-607 (1985).
[170] H. R. Park, S. M. Koo, O. K. Suwal, Y. M. Park, J. S. Kyoung, M. A. Seo, S. S. Choi, N. K. Park, D. S. Kim, and K. J. Ahn, "Resonance behavior

of single ultrathin slot antennas on finite dielectric substrates in terahertz regime," Appl. Phys. Lett. **96**, 211109 (2010).
[171] B. Luk'yanchuk, N. I. Zheludev, S. A. Maier, N. J. Halas, P. Nordlander, H. Giessen, and C. T. Chong, "The Fano resonance in plasmonic nanostructures and metamaterials," Nat. Mater. **9**, 707-715 (2010).
[172] P. Gaal, W. Kuehn, K. Reimann, M. Woerner, T. Elsaesser, and R. Hey, "Internal motions of a quasiparticle governing its ultrafast nonlinear response," Nature **450**, 1210-1213 (2007).
[173] M. Hoffmann, J. Hebling, H. Hwang, K.-L. Yeh, and K. Nelson, "Impact ionization in InSb probed by terahertz pump—terahertz probe spectroscopy," Phys. Rev. B **79** (2009).
[174] F. Blanchard, D. Golde, F. H. Su, L. Razzari, G. Sharma, R. Morandotti, T. Ozaki, M. Reid, M. Kira, S. W. Koch, and F. A. Hegmann, "Effective Mass Anisotropy of Hot Electrons in Nonparabolic Conduction Bands of n-Doped InGaAs Films Using Ultrafast Terahertz Pump-Probe Techniques," Phys. Rev. Lett. **107** (2011).
[175] K. P. H. Lui, and F. A. Hegmann, "Ultrafast carrier relaxation in radiation-damaged silicon on sapphire studied by optical-pump–terahertz-probe experiments," Appl. Phys. Lett. **78**, 3478 (2001).
[176] J. Zielbauer, and M. Wegener, "Ultrafast optical pump THz-probe spectroscopy on silicon," Appl. Phys. Lett. **68**, 1223 (1996).
[177] P. Uhd Jepsen, W. Schairer, I. H. Libon, U. Lemmer, N. E. Hecker, M. Birkholz, K. Lips, and M. Schall, "Ultrafast carrier trapping in microcrystalline silicon observed in optical pump–terahertz probe measurements," Appl. Phys. Lett. **79**, 1291 (2001).
[178] R. D. Averitt, G. Rodriguez, J. L. W. Siders, S. A. Trugman, and A. J. Taylor, "Conductivity artifacts in optical-pump THz-probe measurements of $YBa_2Cu_3O_7$," J. Opt. Soc. Am. B **17**, 327-331 (2000).
[179] M. C. Hoffmann, N. C. Brandt, H. Y. Hwang, K.-L. Yeh, and K. A. Nelson, "Terahertz Kerr effect," Appl. Phys. Lett. **95**, 231105 (2009).
[180] M. Zalkovskij, A. C. Strikwerda, K. Iwaszczuk, A. Popescu, D. Savastru, R. Malureanu, A. V. Lavrinenko, and P. U. Jepsen, "Terahertz-induced Kerr effect in amorphous chalcogenide glasses," Appl. Phys. Lett. **103**, 221102 (2013).
[181] M. Cornet, J. Degert, E. Abraham, and E. Freysz, "Terahertz Kerr effect in gallium phosphide crystal," J. Opt. Soc. Am. B **31**, 1648 (2014).
[182] M. C. Hoffmann, J. Hebling, H. Y. Hwang, K.-L. Yeh, and K. A. Nelson, "THz-pump/THz-probe spectroscopy of semiconductors at high field strengths [Invited]," J. Opt. Soc. Am. B **26**, A29 (2009).
[183] D. Turchinovich, J. M. Hvam, and M. C. Hoffmann, "Self-phase modulation of a single-cycle terahertz pulse by nonlinear free-carrier response in a semiconductor," Phys. Rev. B **85,** 201304 (2012).

[184] M. T. Zanni, and R. M. Hochstrasser, "Two-dimensional infrared spectroscopy: a promising new method for the time resolution of structures," Curr. Opin. Struct. Biol. **11**, 516-522 (2001).
[185] W. Kühn, "Nonlinear Terahertz Spectroscopy in One and Two Dimensions," (Humboldt-Universität zu Berlin, 2011).
[186] F. Junginger, B. Mayer, C. Schmidt, O. Schubert, S. Mährlein, A. Leitenstorfer, R. Huber, and A. Pashkin, "Nonperturbative Interband Response of a Bulk InSb Semiconductor Driven Off Resonantly by Terahertz Electromagnetic Few-Cycle Pulses," Phys. Rev. Lett. **109**, 147403 (2012).
[187] M. Woerner, W. Kuehn, P. Bowlan, K. Reimann, and T. Elsaesser, "Ultrafast two-dimensional terahertz spectroscopy of elementary excitations in solids," New J. Phys. **15**, 025039 (2013).
[188] C. Somma, K. Reimann, C. Flytzanis, T. Elsaesser, and M. Woerner, "High-Field Terahertz Bulk Photovoltaic Effect in Lithium Niobate," Phys. Rev. Lett. **112** (2014).
[189] P. Bowlan, E. Martinez-Moreno, K. Reimann, T. Elsaesser, and M. Woerner, "Ultrafast terahertz response of multilayer graphene in the nonperturbative regime," Phys. Rev. B **89** (2014).
[190] H. Hirori, K. Yamashita, M. Nagai, and K. Tanaka, "Attenuated Total Reflection Spectroscopy in Time Domain Using Terahertz Coherent Pulses," Jpn. J. Appl. Phys. **43**, L1287-L1289 (2004).
[191] M. Nagai, H. Yada, T. Arikawa, and K. Tanaka, "Terahertz time-domain attenuated total reflection spectroscopy in water and biological solution," International Journal of Infrared and Millimeter Waves **27**, 505-515 (2007).
[192] D. M. Mittleman, M. C. Nuss, and V. L. Colvin, "Terahertz spectroscopy of water in inverse micelles," Chem. Phys. Lett. **275**, 332-338 (1997).
[193] L. Thrane, R. H. Jacobsen, P. Uhd Jepsen, and S. R. Keiding, "THz reflection spectroscopy of liquid water," Chem. Phys. Lett. **240**, 330-333 (1995).
[194] T.-I. Jeon, and D. Grischkowsky, "Characterization of optically dense, doped semiconductors by reflection THz time domain spectroscopy," Appl. Phys. Lett. **72**, 3032 (1998).
[195] L. Razzari, F. Su, G. Sharma, F. Blanchard, A. Ayesheshim, H. C. Bandulet, R. Morandotti, J. C. Kieffer, T. Ozaki, M. Reid, and F. Hegmann, "Nonlinear ultrafast modulation of the optical absorption of intense few-cycle terahertz pulses in n-doped semiconductors," Phys. Rev. B **79** (2009).
[196] M. Dressel, and G. Grüner, *Electrodynamics of Solids: Optical Properties of Electrons in Matter* (Cambridge University Press, 2002).
[197] E. Hecht, *Optics* (Addison-Wesley, 2002).

[198] E. R. Brown, J. E. Bjarnason, A. M. Fedor, and T. M. Korter, "On the strong and narrow absorption signature in lactose at 0.53 THz," Appl. Phys. Lett. **90**, 061908 (2007).
[199] K.-E. Peiponen, A. Zeitler, and M. Kuwata-Gonokami, *Terahertz Spectroscopy and Imaging* (Springer, 2012).
[200] W. H. Press, S. A. Teukolsky, W. T. Vetterling, and B. P. Flannery, *Numerical Recipes 3rd Edition: The Art of Scientific Computing* (Cambridge University Press, 2007).
[201] B. Fischer, "Broadband THz Time-Domain Spectroscopy of Biomolecules," (Albert-Ludwigs University, Freiburg, Germany, 2005).
[202] J. Kroll, J. Darmo, and K. Unterrainer, "Terahertz spectroscopy of vibrational modes of molecular crystal of sucrose," Infrared and Millimeter Waves, 2004 and 12th International Conference on Terahertz Electronics, 2004. Conference Digest of the 2004 Joint 29th International Conference on, 89-90 (2004).
[203] J. Kröll, J. Darmo, and K. Unterrainer, "Terahertz optical activity of sucrose single-crystals," Vib. Spectrosc. **43**, 324-329 (2007).
[204] M. Schall, M. Walther, and P. Uhd Jepsen, "Fundamental and second-order phonon processes in CdTe and ZnTe," Phys. Rev. B **64** (2001).
[205] H. Hirori, K. Shinokita, M. Shirai, S. Tani, Y. Kadoya, and K. Tanaka, "Extraordinary carrier multiplication gated by a picosecond electric field pulse," Nat. Commun. **2**, 594 (2011).
[206] A. T. Tarekegne, K. Iwaszczuk, M. Zalkovskij, A. C. Strikwerda, and P. U. Jepsen, "Impact ionization in high resistivity silicon induced by an intense terahertz field enhanced by an antenna array," New J. Phys. **17**, 043002 (2015).
[207] E. Cartier, M. V. Fischetti, E. A. Eklund, and F. R. McFeely, "Impact ionization in silicon," Appl. Phys. Lett. **62**, 3339-3341 (1993).
[208] E. O. Kane, "Band Structure of Silicon from an Adjusted Heine-Abarenkov Calculation," Phys. Rev. **146**, 558-567 (1966).
[209] A. Sell, A. Leitenstorfer, and R. Huber, "Phase-locked generation and field-resolved detection of widely tunable terahertz pulses with amplitudes exceeding 100 MV/cm," Opt. Lett. **33**, 2767 (2008).
[210] Z. Yan, D. Hou, P. Huang, B. Cao, G. Zhang, and Z. Zhou, "Terahertz spectroscopic investigation of L-glutamic acid and L-tyrosine," Meas. Sci. Technol. **19**, 015602 (2008).
[211] Y. Ueno, R. Rungsawang, I. Tomita, and K. Ajito, "Quantitative measurements of amino acids by terahertz time-domain transmission spectroscopy," Anal. Chem. **78**, 5424-5428 (2006).
[212] K. L. Vodopyanov, and M. C. Hoffmann, "Intense THz pulses for condensed matter physics," Proc. SPIE 9347, Nonlinear Frequency Generation and Conversion: Materials, Devices, and Applications XIV **9347**, 93470G (2015).

[213] F. Blanchard, A. Doi, T. Tanaka, H. Hirori, H. Tanaka, Y. Kadoya, and K. Tanaka, "Real-time terahertz near-field microscope," Opt. Express **19**, 8277-8284 (2011).

8.2. Journal publications

- P. Klarskov, A. Tarekegne, K. Iwaszczuk, X.-C. Zhang, and P. U. Jepsen, “Resonant field enhancement by lattice mode coupling in metallic micro-slit arrays”, submitted to Optics Express, April 2015.
- T. Wang, P. Klarskov, P.U. Jepsen, "Ultrabroadband THz Time-Domain Spectroscopy of a Free-Flowing Water Film," IEEE Transactions on Terahertz Science and Technology 425-7 (2014).
- P. Klarskov and P. U. Jepsen, “Observation of forward propagating THz mode emitted from a two-color laser-induced air plasma,” J. Infrared, Millimeter, Terahertz Waves, pp. 5–7, Oct. 2013.
- P. Klarskov, A. C. Strikwerda, K. Iwaszczuk and P. U. Jepsen, ”Experimental 3D beam profiling and modeling of a terahertz beam generated from a two-color air plasma”, New J. Phys. 15, 075012 (2013).

8.3. Conference proceedings

- P. Klarskov, K. Iwaszczuk, M. Zalkovskij, R. Malureanu, J. Dai, X. Zhang, and P. U. Jepsen, "Resonant field enhancement in periodically arranged microslits for non-linear terahertz spectroscopy," in 2014 39th International Conference on Infrared, Millimeter, and Terahertz waves (IRMMW-THz), IEEE (2014).
- P. Klarskov, S. Clark, and P. Jepsen, "Numerical Investigation of Ultrafast interaction between THz Fields and Crystalline Materials," in CLEO: 2014, OSA Technical Digest (online) (Optical Society of America, 2014), paper SW3F.2.

- P. Klarskov, M. Zalkovskij, A. Strikwerda, and P. Jepsen, "Spectrally resolved measurements of the terahertz beam profile generated from a two-color air plasma," in CLEO: 2014, OSA Technical Digest (online) (Optical Society of America, 2014), paper STu1F.6.
- P. Klarskov, S. J. Clark, and P. U. Jepsen, ”Modeling of ultrafast THz interactions in molecular crystals”, Proceedings of SPIE, the International Society for Optical Engineering, 8984-12 (2014).
- P. Klarskov, T. Wang, J. D. Buron, A. C. Strikwerda and P. U. Jepsen, ” Spatial properties of a terahertz beam generated from a two-color air plasma”, Proceedings of SPIE, OP13O SPIE Optical Engineering + Applications, paper 8846-28 (2013).
- C. Strikwerda, P. Klarskov, and P. U. Jepsen. “Evolution of the THz Beam Profile From a Two-Color Air Plasma Through a Beam Waist”. CLEO Technical Digest (2013):
- P. Klarskov, A. C. Strikwerda, T. Wang, M. Zalkovskij and P. U. Jepsen, ”3D terahertz beam profiling”, Proceedings of SPIE, the International Society for Optical Engineering, 8624 (2013).

8.4. Conference presentations

- P. Klarskov, A. Tarekegne, K. Iwaszczuk, and P. U. Jepsen, “Field enhancing coupling between microslits and lattice modes resonant at terahertz frequencies” talk at International Workshop on Terahertz Science and Technology 2015 (OTST2015), San Diego, USA.
- P. Klarskov, P. U. Jepsen “Field enhancing coupling between lattice modes and microslits resonantat THz frequencies”, talk at TeraNano V, Martinique 2014.

- P. Klarskov, S. J. Clark, X.-C. Zhang, P. Uhd Jepsen, “Nonlinear spectroscopy with intense table-top terahertz sources”, invited talk at LAPHYS’14, Sofia, Bulgaria.
- P. Klarskov, “Towards Nonlinear Terahertz Spectroscopy”, physics seminar given at University of Buffalo (SUNY), June 2014.
- P. Klarskov, S. J. Clark, P. U. Jepsen, ” Numerical Investigation of Ultrafast interaction between THz Fields and Crystalline Materials”, talk at CLEO 2014, San José, USA.
- P.Klarskov, M. Zalkovskij, A. C. Strikwerda, and P. U. Jepsen, “Spectrally resolved measurements of the terahertz beam profile generated from a two-color air plasma” talk at CLEO 2014, San José, USA.
- P. Klarskov, S. J. Clark, P. U. Jepsen, ”Modeling of ultrafast THz interactions in molecular crystals”, talk at Photonics West 2014, San Francisco, USA.
- P. U. Jepsen, D. G. Cooke, K. Iwaszczuk, A. Strikwerda, P. Klarskov and M. Zalkovskij, “Ultrafast terahertz dynamics in bulk and nanostructured materials”, invited talk at Photonics West 2014, San Francisco, USA.
- P. Klarskov, T. Wang, J. D. Buron, A. C. Strikwerda and P. U. Jepsen , ”Experimental beam profiling and modeling of a terahertz beam generated from a 2-color air plasma”, SPIE Optics + Photonics i august 2013, San Diego, USA.
- A. C. Strikwerda, P. Klarskov and P.U. Jepsen, ”Evolution of the THz Beam Profile from a Two-Color Air Plasma Through a Beam Waist”, Special Symposium: Nonlinear Terahertz Science and Technology, CLEO:2013, San José, USA.

- P. Klarskov, A. C. Strikwerda and P.U. Jepsen, ”3D Terahertz Beam Profiling”, poster presentation at International Workshop on Terahertz Science and Technology 2013 (OTST2013), Kyoto, Japan.
- P. Klarskov, A. C. Strikwerda, T. Wang, M. Zalkovskij and Peter U. Jepsen, ”3D Terahertz Beam Profiling”, talk at SPIE Photonics West 2013, San Francisco, USA.
- P. Klarskov and Peter Uhd Jepsen, “3D Terahertz Beam Profiling”, talk at 4th Workshop on THz Science & Technology 2012, Elba, Italy.

8.5. Funding and awards

- Student Speaker Winner, TeraNano V, Martinique 2014.
- Eliteforsk travel grant 2014, 300.000 dkr.
- Toubro Fonden, 100.000 dkr for laboratory equipment (December 2013).
- Brdn. Hartmanns Fond, 101.724 dkr for laboratory equipment (December 2013).
- Poster prize for ”most impressive presentation” at the International Workshop on Terahertz Science and Technology 2013 (OTST2013), Kyoto, Japan.
- Reinholdt W. Jorck og Hustrus Fond travel scholarship, 200.000 dkr for postdoc stay at Brown University.
- FTP Postdoc scholarship for the project “HI-TEM: High-resolution Terahertz Emission Microscopy for Conductivity Sensing on Nanoscale”, covering 2 years at Brown University starting in 2015.

Appendix A. CASTEP files

.cell file for CsI 2x2x2 supercell

```
%block lattice_abc
9.1334 9.1334 9.1334
90.00000 90.0000 90.0000
%endblock lattice_abc

%block positions_frac
I  0.250000 0.250000 0.250000
I  0.750000 0.250000 0.250000
I  0.250000 0.750000 0.250000
I  0.750000 0.750000 0.250000
I  0.250000 0.250000 0.750000
I  0.750000 0.250000 0.750000
I  0.250000 0.750000 0.750000
I  0.750000 0.750000 0.750000
Cs 0.000000 0.000000 0.000000
Cs 0.500000 0.000000 0.000000
Cs 0.000000 0.500000 0.000000
Cs 0.500000 0.500000 0.000000
Cs 0.000000 0.000000 0.500000
Cs 0.500000 0.000000 0.500000
Cs 0.000000 0.500000 0.500000
Cs 0.500000 0.500000 0.500000
%endblock positions_frac

kpoints_mp_grid 2 2 2

%block species_pot
Cs Cs_00PBE.usp
I   I_00PBE.usp
%endblock species_pot
```

.param file with a THz field with 1 MV/cm field strength applied

```
task : MolecularDynamics
THz_Emax : 0.002 Hartree/Bohr/e
THz_width : 0.2 ps
THz_delay_time : 1.0 ps
THz_direction : z
THz_polarisability : 72.0 Ang**3
```

md_temperature : 10 K
md_num_iter : 20000
md_delta_t : 1.0 fs
md_sample_iter : 1
md_ensemble : nvt
md_thermostat = nose-hoover
md_nhc_length : 5
md_ion_t = 10 ps

Script for submitting a job on the FOTONANO cluster

```
#!/bin/sh
#PBS -m ae
#PBS -N castep
#PBS -q fotonano
#PBS -l nodes=2:ppn=16,feature=XeonE5-2665
#PBS -l walltime=24:00:00

module purge
module add gcc mpi/gcc-4.7.2-openmpi-1.6.3
export castep=$HOME/CASTEP-THZ/CASTEP-7.0/obj/linux_x86_64_gfortran4.6/castep.mpi

cd $PBS_O_WORKDIR
mpirun -np $PBS_NP $castep CsI_2x2x2supercell
```

Appendix B. Misaligned THz beam profiles

Below is shown four beam profiles recorded during a scan through the focal plane of a $LiNbO_3$ setup. For this setup the focusing procedure where three off-axis parabolic mirrors is used as introduced in [93]. Here, the beam path has been aligned with a HeNe laser, but no further alignment of the THz beam with the NEC camera has been done. Even though the focus (Stage position 45) looks acceptable, the unfocused beam profiles are rather distorted. It is expected that alignment of the unfocused beam would lead to a better focus and thereby a larger field strength.

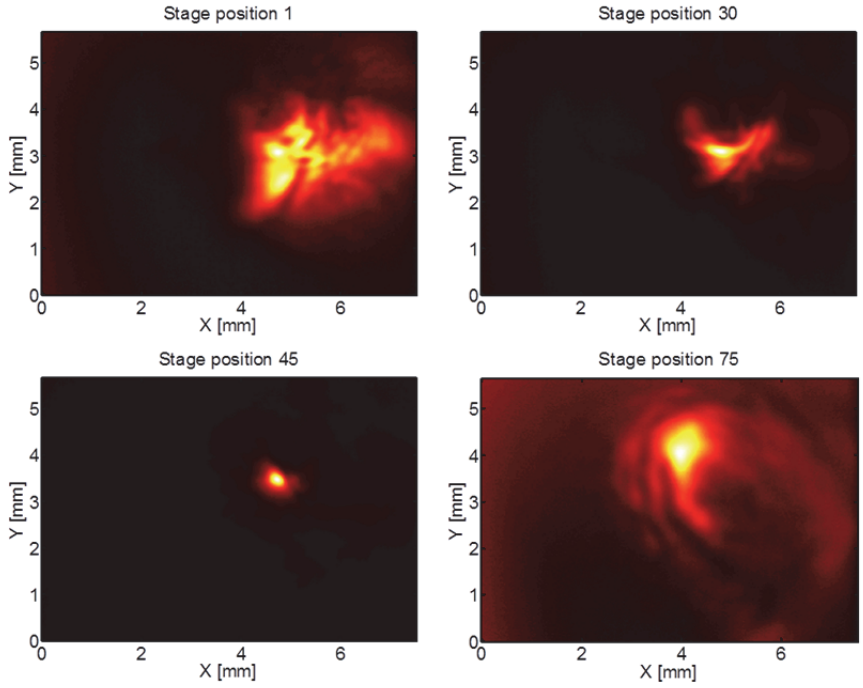

Fig. B.1: Beam profiles recorded at four different stage positions of a THz beam where only alignment with a HeNe laser has been done. Stage position 45 is the focus.

Appendix C. Mathematical window functions

During the thesis a few mathematical window functions have been used namely the Hanning window, the Tukey window and the boxcar window, which are shown in the figure below. The Hanning window has the shape of

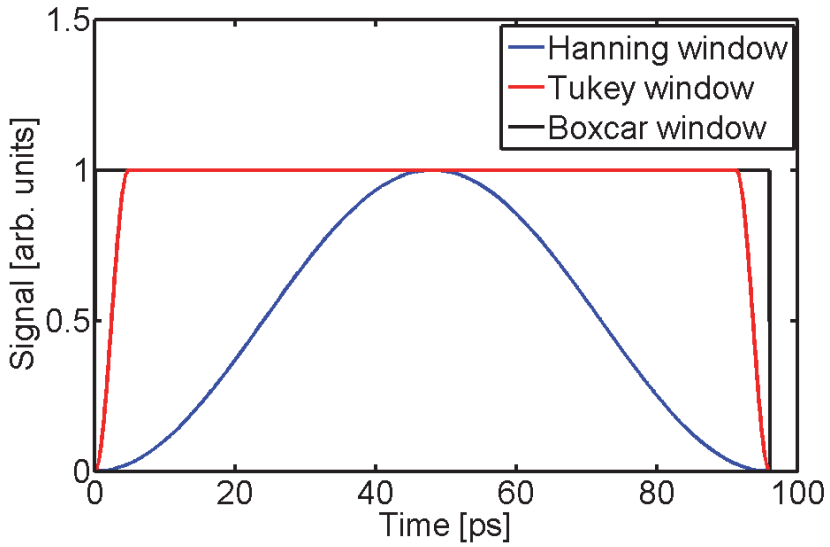

C.1: Hanning window, Tukey window and boxcar window.

a cosine while the boxcar window is a square. The Tukey window is something in between i.e.

$$W = \begin{cases} \frac{1}{2}\left(1+\cos\left(\frac{2\pi}{r}(t-r/2)\right)\right), & 0 \le t < \frac{r}{2} \\ 1, & \frac{r}{2} \le t < 1-\frac{r}{2} \\ \frac{1}{2}\left(1+\cos\left(\frac{2\pi}{r}(t-1+r/2)\right)\right), & 1-\frac{r}{2} \le t < 1 \end{cases}$$

r determines how close to a Hanning window the Tukey window is. For r=1 the Tukey window equals the Hanning window, and for r=0 the Tukey

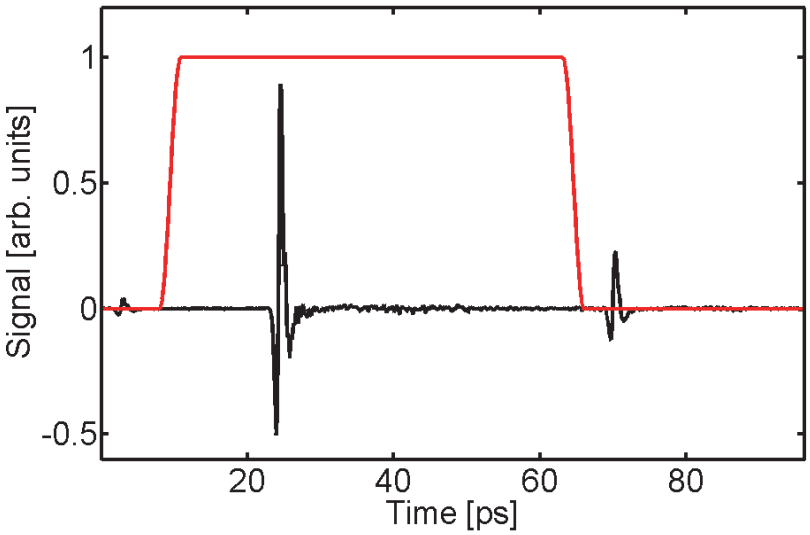

C.2: Example of a waveform with a reflection from a thick silicon wafer (back curve). The red curve is the applied Tukey window.

window equals a boxcar window. In this work *r* is always set to 0.1, which gives the shape of the Tukey window shown above. An example of a time trace is shown in the figure below (black curve), where the Tukey window is set so that it will eliminate the first reflection. With the r-value of 0.1 the peak signal is maintained together with most of the trace until the decays giving a smooth suppression of the oscillations in the time trace. A boxcar window decays too abruptly and often leads to artifacts in the spectrum after Fourier transforming the time trace.

Appendix D. Photos

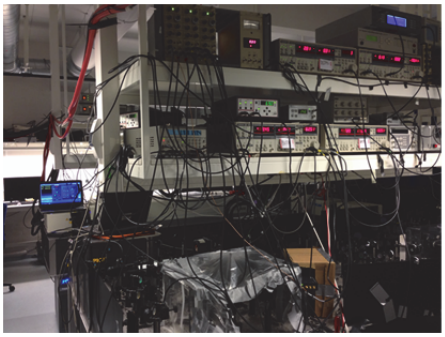
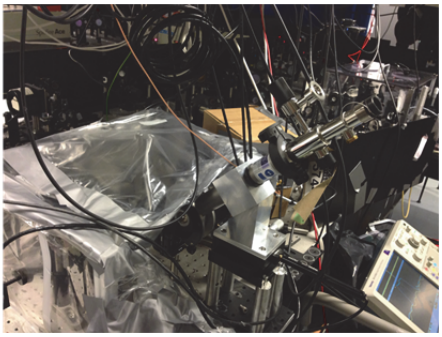

D.1: Left: setup together with boxcars, lockins, choppers, delay generator etc. Right: cryostat in purge tent.

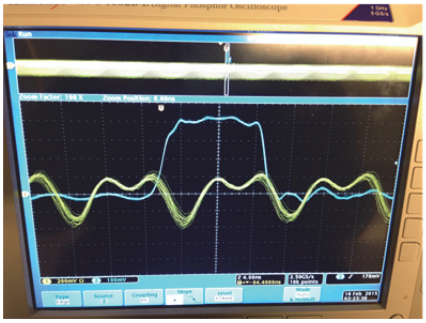
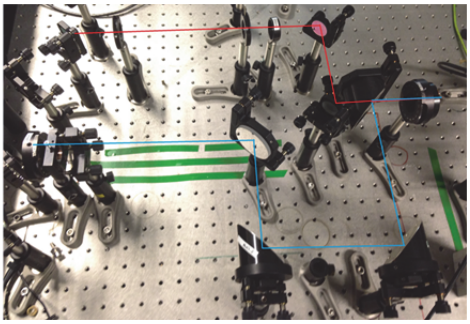

D.2: Left: Oscilloscope showing a 9 ns wide boxcar window (blue) and the photodiode signal (yellow). Right: 1D DSTMS setup.


D.3: Left: preparation of sucrose samples. Right: sucrose sample in cryostat